



TECHNISCHE
UNIVERSITÄT
WIEN
Vienna | Austria

Diplomarbeit

Iron-based Metal-Organic Frameworks for Photocatalytic Nitrogen Reduction to Ammonia

Zur Erlangung des akademischen Grades einer

Diplom-Ingenieurin

an der Technischen Universität Wien, Fakultät für Technische Chemie

Eingereicht von

Jana Bischoff, BSc

Unter der Leitung von

Projektass.in (FWF) Dr.in rer.nat. **Shaghayegh Naghdi, MSc**

Univ.Prof. Mag.rer.nat. Dr.rer.nat. **Dominik Eder**

Institut für Materialchemie

Forschungsbereich Molekulare Materialchemie

Getreidemarkt 9/165

1060 Wien

Austria

Contents

Abstract	i
Zusammenfassung.....	iii
List of Abbreviations.....	v
List of Figures.....	vi
List of Tables.....	x
1 Introduction.....	1
1.1 Environmental Sustainability Issues.....	1
1.2 Motivation and Aims.....	3
2 Theoretical Background.....	5
2.1 Photocatalysis.....	5
2.2 Electronic Properties of Semiconductor Photocatalyst.....	6
2.3 Perspective of Nitrogen Reduction to Ammonia	8
2.3.1 Properties of N ₂ Molecule.....	8
2.4 Industrial Ammonia Synthesis.....	9
2.4.1 Thermodynamic Aspects of Nitrogen Conversion to Ammonia.....	9
2.4.2 Conventional Heterogenous Catalyst for Industrial Ammonia Synthesis.....	10
2.5 Basic Principle of Photocatalytic Nitrogen Reduction	11
2.5.1 Thermodynamics of Nitrogen Reduction over Semiconductor Photocatalyst	11
2.6 Possible Pathways of Nitrogen Reduction in Heterogenous Catalysis	14
3 Metal-Organic Frameworks	15
3.1 Introduction to Metal-Organic Frameworks	15
3.2 Structural Features of MOFs Photocatalyst	18
3.3 Prospective of MOFs for Photocatalytic Nitrogen Reduction to Ammonia.....	19
3.4 Fe-based MOFs	20
3.4.1 MIL-101(Fe)	20
4 Methods.....	23
4.1 Powder X-ray Diffraction (PXRD).....	23
4.2 Thermogravimetric Analysis (TGA).....	25
4.3 Physisorption	25
4.3.1 Classification of Physisorption Isotherms	27
4.3.2 The Origin of Hysteresis	29

4.3.3	Principles of the Brunauer-Emmet-Teller (BET) Method	30
4.4	Spectroscopy Techniques	31
4.4.1	Diffuse Reflectance Spectroscopy (DRS)	31
4.4.2	Attenuated Total Reflectance Fourier Transform Infrared Spectroscopy (ATR-FTIR)	31
4.4.3	Ultraviolet Visible Spectroscopy (UV-Vis).....	32
4.5	Microscopy Techniques	33
4.5.1	Scanning Electron Microscopy (SEM).....	33
4.6	Electrochemical measurements.....	35
4.6.1	Linear Sweep Voltammetry (LSV).....	35
4.7	In-situ Techniques.....	36
4.7.1	In-situ X-ray Diffraction (In-situ XRD)	36
4.7.2	In-situ Diffuse Reflectance Fourier Transform Infrared Spectroscopy (DRIFTS).....	36
5	Experimental Part	37
5.1	Material Synthesis.....	37
5.1.1	Synthesis of Mixed-ligand MOFs xNH ₂ -MIL-101-Fe	37
5.1.2	Synthesis of Single-ligand MOFs with Different Functional Groups.....	37
5.1.3	Synthesis of Reference Single-ligand MOFs	38
5.2	Heat-treatment of Mixed-ligand Fe-MOFs.....	38
5.3	Photocatalytic Experiments	39
5.3.1	Photocatalytic Nitrogen Reduction Reaction (NRR)	39
5.3.2	Spectrophotometric Ammonium Detection	39
5.4	Electrochemical Experiments.....	40
6	Results and Discussion	41
6.1	Influence of Ligand Tuning on Properties of Fe-based MOFs	41
6.1.1	Single-ligand and Mixed-ligand Fe-MOFs with Different NH ₂ -BDC Content.....	41
6.1.2	Single-ligand MOFs with Opposite Electronic Tuning Effect	62
6.2	Effect of Ligand Tuning on Photocatalytic Nitrogen Reduction Reaction	65
6.2.1	Nessler's Reagent Ammonia Detection Method.....	66
6.2.2	Investigation of Photocatalytic Behavior of Single- and Mixed-ligand Fe-MOFs.....	67
6.3	Studies on Selective Ligand Removal Strategy	70
6.3.1	TGA of Mixed-ligand Fe-MOFs	70
6.3.2	In-situ DRIFTS Studies on Mixed-ligand Fe-MOFs	72
6.3.3	In-situ XRD of Mixed-ligand Fe-MOFs	75
6.3.4	Conclusion on Selective Ligand Removal Parameters.....	76

6.3.5	Characterization of Heat-treated MOFs.....	77
6.4	Effect of Heat-Treatment on Photocatalytic Nitrogen Reduction Reaction	87
6.5	Investigations of the Structure Activity Relationship	88
6.5.1	Structural Characterization of MIL-53-Fe.....	89
6.5.2	Influence of SBU Tuning of Photocatalytic Nitrogen Reduction.....	90
6.6	Investigations on the Rate-Determining Step	90
6.7	Structure and Photocatalytic Activity of Ce-Uio-66 MOF	92
7	Discussion	94
7.1	Influence of Ligand- and SBU-tuning	94
7.2	Influence of Heat-treatment.....	100
8	Conclusion	102
9	Outlook	104
10	References	105
11	Appendix.....	120

Abstract

Ammonia (NH_3) is an important industrial raw material which is widely used in fertilizers, refrigerants, and other chemical products. NH_3 also shows great potential as a clean energy carrier owing to its high energy density and clean combustion products with the main advantage of abundant availability of nitrogen (N_2) in the atmosphere. The current industrial conversion of N_2 to NH_3 , through heterogenous catalysis via the Haber-Bosch process is a cost-intensive process that needs to be manifested under economically unfavorable reaction conditions such as high temperatures and pressures. Recently, photocatalysis has shown promise as an alternative to this process, where the use of solar energy enables the fixation and conversion of N_2 at ambient conditions.

This thesis aimed at designing and testing metal-organic frameworks (MOFs) as catalysts for photocatalytic nitrogen reduction to ammonia. Accordingly, I synthesized a series of iron-based MOFs and modified them with different strategies, including ligand functionalization and post-synthetic modification through thermal treatment. The influence of different functional groups on structural and physiochemical properties of Fe-based MOFs was investigated with a wide range of state-of-the-art techniques, including XRD, SEM, FTIR, TGA, DRS and N_2 -physisorption. Mixed-ligand MOFs, with varying ratios of amino-terephthalic acid (NH_2 -BDC) to terephthalic acid (BDC) as well as single-ligand MOFs with opposing electronic tuning effect were utilized for photocatalytic nitrogen reduction reaction (NRR). In order to obtain insight into structure-activity relationships in MOFs, I evaluated the photocatalytic performance of Fe-based MOFs with different secondary building units (SBUs). Furthermore, the influence of thermal treatment on photocatalytic activity was studied.

Ligand modification with electron-donating NH_2 -group led to the formation of different Fe-terephthalate MOFs. Specifically, amino-substituted MIL-101 was successfully synthesized up to 17.5 mol.% of NH_2 -BDC, while samples with higher molar ratios adopted the MIL-88B crystalline structure. Furthermore, the introduction of nitro and bromo functional groups in MIL-101

resulted in the formation of phase-pure MIL-101 analogs. Particularly noteworthy was the successful synthesis of Br-MIL-101, a variant not documented in previous studies.

Photocatalytic studies showed that the ammonia production rate of mixed-ligand MOFs decreased with increasing NH₂-BDC content. In fact, proton-donating bromide group resulted in the highest production yield among all tested Fe-MOFs. Electrochemical measurements revealed that sluggish kinetics of the water oxidation half-reaction with proton-accepting amino ligand limited the overall conversion, which supported the assumption that Br-BDC functions as a proton pump. The studies on SBU-tuning in Fe-based MOF demonstrated that oxo-bridged trinuclear SBU exhibits 83 % higher yield compared to the mononuclear SBU.

Applying thermal treatment as a strategy for selective removal of thermolabile ligand in mixed-ligand Fe-MOFs created oxygen vacancy defects and defect-related electronic states. The presence of oxygen vacancy levels resulted in more efficient charge separation and improved photocatalytic performance.

This work provides a comprehensive understanding of the structure-related photocatalytic performance of Fe-terephthalate MOFs, elucidating the rate-limiting step of N₂ conversion to NH₃. It lays the groundwork for future catalyst enhancement, emphasizing the need for further exploration of the underlying mechanism and evaluating the impact of ligand tuning on electronic structure.

Zusammenfassung

Ammoniak (NH_3) ist ein wichtiger industrieller Rohstoff, der weiterhin in Düngemitteln, Kältemittel und anderen chemischen Produkten verwendet wird. NH_3 zeigt aufgrund seiner hohen Energiedichte und sauberen Verbrennung auch ein großes Potenzial als Energieträger mit dem Hauptvorteil einer enormen Verfügbarkeit von Stickstoff (N_2) in der Atmosphäre. Die klassische industrielle Ammoniaksynthese (Haber-Bosch) ist ein kostenintensiver Prozess, der unter extremen Reaktionsbedingungen stattfindet. Die photokatalytische Umwandlung wird als vielversprechende Alternative zu diesem Verfahren angesehen. Sonnenenergie ist die treibende Kraft für diesen Prozess und soll die Umwandlung von N_2 bei Raumtemperatur und Umgebungsdruck ermöglichen.

Das Ziel dieser Arbeit war es, metallorganische Gerüstverbindungen (MOFs) als Katalysatoren für eine photokatalytische Stickstoffreduktion zu Ammoniak zu verwenden. Deshalb, wurde eine Reihe von eisenbasierten MOFs synthetisiert und unterschiedlich modifiziert. Diese beinhalten die kontrollierte Funktionalisierung der Liganden mit elektronen-ziehenden oder -dotierenden Gruppen, sowie die selektive Entfernung von Liganden durch thermische Behandlung. Der Einfluss verschiedener funktioneller Gruppen auf die strukturellen und physikalisch-chemischen Eigenschaften von Fe-basierten MOFs wurde mit einer Vielzahl von State-of-the-Art Techniken untersucht, inklusive XRD, REM, FTIR, TGA, DRS und N_2 -Physisorption. Zudem wurden MOFs mit zwei unterschiedlichen Liganden ("mixed-ligand MOFs") untersucht. Um Einsicht in die Struktur-Wirkungsbeziehung zu erhalten, wurden die photokatalytische Eigenschaften von Fe-basierten MOFs mit verschiedenen sekundären Baueinheiten ("secondary-building units" - SBU) getestet. Des Weiteren wurde der Einfluss der thermischen Behandlung auf die photokatalytische Aktivität untersucht.

Die Modifikation des Liganden durch die elektronenliefernde NH_2 -Gruppe hat zur bevorzugten Bildung verschiedener Fe-Terephthalat-MOFs sowie zu unterschiedlichen physikochemischen Eigenschaften geführt. Aminosubstituiertes MIL-101 wurde bis zu 17,5 Mol-% NH_2 -BDC erfolgreich synthetisiert, während höhere NH_2 -BDC-Anteile zur Bildung der MIL-88B-Kristallstruktur führten. Darüber hinaus führte die Einführung von Nitro- und Bromfunktionen in

MIL-101 zur Bildung von reinphasigen MIL-101-Analoga. Besonders bemerkenswert ist die erfolgreiche Synthese von Br-MIL-101, einer Variante, die in früheren Studien nicht dokumentiert wurde.

Photoakatalytischen Studien zeigten, dass die Ammoniakproduktionsrate von Mischliganden-MOFs mit zunehmendem NH₂-BDC-Gehalt, abnimmt. Im Gegensatz dazu führte die Funktionalisierung des protonenspendenden Bromids zu der höchsten Produktionsrate unter den hergestellten Fe-MOFs. Elektrochemische Messungen zeigten, dass die begrenzte Stofftransport der Wasseroxidationshalbreaktion mit protonenakzeptierenden Aminoliganden eine limitierte Gesamtumwandlung aufwies, was die Annahme stützte, dass Br-BDC tatsächlich als Protonenpumpe fungiert. Es konnte zudem gezeigt werden, dass die SBU, d.h. die Konektivität der Metallzentren, einen überraschend großen Einfluss auf die Photokatalytischen Eigenschaften aufweisen. Das dreikernige μ_3 -oxo-verbrückte SBU weist, im Vergleich zur mononuklearen SBU eine um 83 % höhere Ausbeute auf.

Die selektive Entfernung des thermolabilen Liganden in „mixed-ligand“ Fe-basierten MOFs, hat zu Sauerstoff-Fehlstellen und defektbedingten elektronischen Energieniveaus innerhalb der Bandlücke, geführt. Das Vorhandensein von Sauerstoff-Fehlstellen führte zu einer effizienteren Ladungstrennung und einer verbesserten photokatalytischen Leistung.

Diese Arbeit bietet ein umfassendes Verständnis der strukturbezogenen photokatalytischen Leistung von Fe-Terephthalat-MOFs und klärt den geschwindigkeitsbestimmenden Schritt der Umwandlung von Stickstoff in Ammoniak. Sie legt den Grundstein für künftige Katalysatorverbesserungen und unterstreicht die Notwendigkeit einer weiteren Erforschung des zugrunde liegenden Mechanismus sowie der Auswirkung der Modifikation des Liganden auf die elektronische Struktur.

List of Abbreviations

ATR-FTIR.....	Attenuated Total Reflection – Fourier Transform Infrared Spectroscopy
BDC.....	Terephthalic acid
BSE.....	Backscattered electrons
CB.....	Conduction band
DRS.....	Diffuse Reflectance Spectroscopy
E_c	Conduction band energy level
E_v	Valence band energy level
E_f	Fermi energy level
E_g	Bandgap
EWG.....	Electron-withdrawing group
HOMO.....	Highest Occupied Molecular Orbital
IR.....	Infrared
LSV.....	Linear sweep voltammetry
LUMO.....	Lowest Unoccupied Molecular Orbital
NH ₂ -BDC.....	Amino-terephthalic acid
NRR.....	Nitrogen Reduction Reaction
OV.....	Oxygen vacancy
SBU.....	Secondary building unit
SE.....	Secondary electrons
SEM.....	Scanning Electron Microscopy
UV.....	Ultraviolet
VB.....	Valence band
WOR.....	Water oxidation reaction
XRD.....	X-ray Diffraction

List of Figures

FIGURE 2-1 ATOMIC ORBITAL HYBRIDIZATION OF NITROGEN IN N_2 ³⁷	8
FIGURE 2-2 MOLECULAR ORBITAL SCHEME OF N_2 , IN ACCORDANCE WITH ⁴⁰	9
FIGURE 2-3 SCHEMATIC REPRESENTATION OF PHOTOCATALYTIC N_2 REDUCTION TO AMMONIA ON SEMICONDUCTOR MATERIAL WITH BAND EDGE POSITIONS WITH RESPECT TO NHE AT PH=0.	12
FIGURE 2-4 SCHEMATIC REPRESENTATION OF DIFFERENT NITROGEN REDUCTION PATHWAYS.	14
FIGURE 3-1 GENERAL SCHEMATIC REPRESENTATION OF THE STRUCTURE OF METAL-ORGANIC FRAMEWORKS.	16
FIGURE 3-2 ILLUSTRATION OF 3D-MOF WITH PERMANENT POROSITY: IN THE LEFT $Zn_4(O)_{12}C_6$ CLUSTER OF MOF-5 WITH ZnO_4 TETRAHEDRA INDICATED WITH BLUE; O-RED; C-BLACK AND BRIDGING BDC LIGAND; IN THE RIGHT THE FRAMEWORK CAVITY IN $Zn_4(O)(BDC)_3$ REPRESENTED AS YELLOW SPHERE ⁶⁵	17
FIGURE 3-3 BALL AND STICK MODEL OF SBU UNIT OF MIL-101-FE ($(M_3O(H_2O)_2X(O_2CR_6))$). DRAWN WITH VESTA.	21
FIGURE 3-4 SCHEMATIC REPRESENTATION OF MIL-101 (FE) METAL-ORGANIC FRAMEWORK: A) TRIMERIC SECONDARY BUILDING UNIT BRIDGED BY THREE CARBOXYLIC FUNCTIONS; B) TEREPHTHALIC ACID LIGAND, WHICH LIES AT C) EDGES OF THE ST, D) SMALLER CAGE WITH F) PENTAGONAL WINDOW, E) LARGER CAGE WITH G) HEXAGONAL WINDOW. ALL STRUCTURES WERE DRAWN IN VESTA SOFTWARE.	22
FIGURE 4-1 ILLUSTRATION OF BRAGG'S DIFFRACTION LAW: D) – LATTICE PLACE SPACING; θ – ANGLE BETWEEN THE LATTICE PLANE AND INCIDENT BEAM (BRAGG ANGLE) ⁹⁵	24
FIGURE 4-2 CLASSIFICATION OF PHYSISORPTION ISOTHERMS BY IUPAC ⁹⁹	28
FIGURE 4-3 THE FOUR TYPES OF HYSTERESIS LOOP DEFINED BY IUPAC ⁹⁹	29
FIGURE 4-4 DIFFERENT EFFECTS PRODUCED BY ELASTIC AND INELASTIC INTERACTIONS OF PRIMARY ELECTRONS WITH THE SAMPLE SURFACE AND NEAR SURFACE REGIONS ¹⁰⁹	34
FIGURE 5-1 EXPERIMENTAL SET-UP FOR PHOTOCATALYTIC NITROGEN REDUCTION REACTION.....	39
FIGURE 6-1 PXRD PATTERNS OF AS-PREPARED SINGLE-LIGAND FE-MOFS COMPARED TO THE SIMULATED PATTERNS: A) BDC-MIL (MOF-235 PEAK IS MARKED WITH *); B) NH_2 -BDC-MIL.....	41
FIGURE 6-2 ENLARGED VIEW OF THE PXRD PATTERNS FOCUSED ON THE CHARACTERISTIC DIFFRACTION PEAKS: A) 5-13 2θ RANGE; B) 15-25 2θ RANGE (MIL-101 PEAKS MARKED WITH # AND MOF-235 PEAKS MARKED WITH *, UNASSIGNED PEAK IS MARKED WITH \diamond).	42
FIGURE 6-3 PXRD PATTERNS OF AS-PREPARED BDC-MIL, NH_2 -MIL AND MIXED-LIGAND XNH_2 -MIL FE-MOFS WITH DIFFERENT NH_2 -BDC CONTENT: A) ALL SAMPLES; B) 17 MOL.% AND HIGHER NH_2 -BDC CONTENT; C) – E) 17 MOL.% AND LOWER NH_2 -BDC CONTENT WITH SIMULATED SPECTRA AS REFERENCE.	44
FIGURE 6-4 CHARACTERISTIC CRYSTALLOGRAPHIC PLANES OF MIL-101: A) (5 1 1) PLANE; B) (4 4 0). EXPORTED USING VESTA.	45
FIGURE 6-5 FTIR SPECTRA OF SINGLE-LIGAND MOFS: A) BDC MIL; B) NH_2 -BDC MIL.....	48
FIGURE 6-6 HYDROGEN BONDING BETWEEN THE NH_2 -GROUP AND OXYGEN OF THE CARBOXYL GROUP.....	50

FIGURE 6-7 FTIR SPECTRA OF MIXED-LIGAND MOFS: A) ENLARGED HIGH FREQUENCY RANGE OF VIBRATIONAL SPECTRA B) ENLARGED VIBRATIONAL SPECTRA IN LOWER FREQUENCY RANGE. THE PEAKS COLORED WITH BLUE SHADE REPRESENT CHARACTERISTIC PEAKS OF MIL-101-FE; THE PEAKS MARKED WITH GREEN COLOR REPRESENTING THE NH ₂ -MIL-88B-FE PHASE.....	50
FIGURE 6-8 ENLARGED VIBRATIONAL SPECTRA IN RANGE BETWEEN 1700 AND 1300 CM ⁻¹	51
FIGURE 6-9 DIFFERENT FE-TEREPHTHALATE PHASES: A) MIL-101-FE; B) MIL-88B-FE; C) MOF-235-FE. EXPORTED USING VESTA SOFTWARE.	53
FIGURE 6-10 PROMOTING EFFECT OF DMF IN THE FORMATION OF μ ₃ -O-CENTERED SBU THAT BUILDS MIL-101 AND MIL-88B FE-MOFS. IN ACCORDANCE WITH ¹³³	55
FIGURE 6-11 CRYSTALLOGRAPHIC PLANES (1 0 2) AND (2 1 1) OF MOF-235 (BDC LIGAND) CORRESPONDING TO THE 2θ = 12.7 ° AND 22.2 ° DIFFRACTION PEAKS.	56
FIGURE 6-12 OPTICAL CHARACTERIZATION OF AS-PREPARED SINGLE-LIGAND MOFS: A) UV-VIS DIFFUSE REFLECTANCE SPECTRA; B) TAUC PLOTS OF THE CATALYST.	58
FIGURE 6-13 DIFFERENT EXCITATION PATHWAYS IN THE FE-MOFS: A) DIRECT EXCITATION IN THE METAL CLUSTER OF MIL-101-FE; B) DUAL EXCITATION PATHWAY IN THE AMINE-FUNCTIONALIZED MOFS.	60
FIGURE 6-14 OPTICAL CHARACTERIZATION OF AS-PREPARED MIXED-LIGAND MOFS: A) KUBELKA MUNK FUNCTIONS; B) TAUC PLOTS; C) SAMPLE COLORS.	61
FIGURE 6-15 CHARACTERIZATION OF SINGLE-LIGAND MOFS WITH DIFFERENT LIGAND FUNCTIONAL GROUPS: A) XRD PATTERNS OF NO ₂ -BDC AND BR-BDC SINGLE-LIGAND MOFS; B) FTIR SPECTRA OF BDC, NO ₂ -BDC AND BR-BDC SINGLE-LIGAND MOFS (NO ₂ BAND MARKED WITH RED SHADE).	63
FIGURE 6-16 OPTICAL CHARACTERIZATION OF AS-PREPARED SINGLE-LIGAND MOFS WITH DIFFERENT FUNCTIONAL GROUPS: A) KUBELKA MUNK FUNCTIONS; B) TAUC PLOTS.	64
FIGURE 6-17 AMMONIA DETECTION VIA NESSLER'S REAGENT METHOD: A) UV-VIS ABSORPTION CURVES OF DIFFERENT CONCENTRATIONS OF NH ₄ ⁺ IONS USING NESSLER'S REAGENT METHOD; B) A CALIBRATION CURVE USED TO ESTIMATE THE CONCENTRATIONS OF NH ₄ ⁺ IONS; C) STANDARD SOLUTIONS OF DIFFERENT NH ₄ ⁺ CONCENTRATIONS.	66
FIGURE 6-18: PHOTOCATALYTIC NH ₄ ⁺ PRODUCTION RATE UNDER AMBIENT CONDITIONS IN WATER WITHOUT SACRIFICIAL AGENT: A) MIXED-LIGAND MOFS WITH DIFFERENT RATIO OF NH ₂ -BDC LIGAND; B) SINGLE-LIGAND MOFS WITH DIFFERENT FUNCTIONAL GROUPS.	67
FIGURE 6-19 FORMATION OF CUS IN FE-TEREPHTHALATE MOF REPORTED BY YOON ET AL. ¹⁵¹	68
FIGURE 6-20 THERMAL STABILITY OF MIXED-LIGAND FE-MOFS WITH DIFFERENT RATIO OF BDC-NH ₂ TO BDC: A) TGA OF AS-PREPARED MOFS; B) ENLARGED REGION OF ONSET DEGRADATION TEMPERATURE.....	70
FIGURE 6-21 IN-SITU DRIFTS MEASUREMENTS OF 2%NH ₂ -MIL-101-FE DURING HEATING UP TO 600 °C WITH RAMP RATE OF 5 °C MIN ⁻¹	72

FIGURE 6-22 CHANGES IN THE INTENSITY OF CHARACTERISTIC IR BAND AS FUNCTION OF TEMPERATURE: A) IR BANDS ASSOCIATED TO THE NH ₂ -BDC LIGAND; B) IR BANDS OF THE OF THE CHARACTERISTIC FRAMEWORK VIBRATIONS.	73
FIGURE 6-23 ISOTHERMAL IN-SITU DRIFTS MEASUREMENTS OF 2%NH ₂ -MIL-101-FE AT 300°C IN AIR ATMOSPHERE.	74
FIGURE 6-24 IN-SITU XRD PATTERNS OF MIXED-LIGAND MOFS: A) 2%NH ₂ -MIL; B) 5%NH ₂ -MIL.	75
FIGURE 6-25 EX-SITU XRD MEASUREMENTS OF HEAT-TREATED MIXED-LIGAND MOFS THERMOLYZED IN AIR ATMOSPHERE AT 300°C FOR DIFFERENT TIME INTERVALS: A) 2%NH ₂ -MIL B) 5%NH ₂ -MIL.	78
FIGURE 6-26 N ₂ PHYSISORPTION ISOTHERMS AT 77K AND CORRESPONDING PORE SIZE DISTRIBUTION OF 5%NH ₂ -MIL: A) AND B) BEFORE TREATMENT; C) AND D) AFTER HEAT-TREATMENT FOR 3H AT 300 °C.	79
FIGURE 6-27 SEM IMAGES OF MIXED-LIGAND MOFS BEFORE AND AFTER HEAT TREATMENT: A) 2%NH ₂ -BDC MOF AS-PREPARED; B) 5%NH ₂ -BDC MOF AS-PREPARED C) 2%NH ₂ -BDC MOF HEAT TREATED; D) 5%NH ₂ -BDC MOF HEAT TREATED.....	80
FIGURE 6-28 COMPARISON OF TAUC PLOTS WITH CORRESPONDING OPTICAL BAND GAP VALUES BEFORE AND AFTER HEAT TREATMENT: A) 2%NH ₂ -MIL AS-PREPARED AND HEAT-TREATED SAMPLE; B) 5%NH ₂ -MIL AS-PREPARED AND HEAT-TREATED SAMPLE; C) 17%NH ₂ -MIL AS-PREPARED AND HEAT-TREATED SAMPLE; D) SINGLE-LIGAND MIL-101-FE AS-PREPARED AND HEAT-TREATED.	83
FIGURE 6-29 COMPARISON OF FTIR SPECTRA OF MIXED-LIGAND MOFS BEFORE AND AFTER HEAT-TREATMENT: A) 2%NH ₂ -MIL; B) 5% NH ₂ -MIL; C) 17%NH ₂ -MIL; D) MIL-101-FE AS REFERENCE.....	84
FIGURE 6-30 ENLARGED FTIR REGION OF NH AND OH BANDS FOR AS-PREPARED AND HEAT-TREATED MIXED-LIGAND MOFS.....	85
FIGURE 6-31 ISOTHERMAL TGA ANALYSIS OF MIXED-LIGAND MOFS CONDUCTED WITH REPRODUCED THERMOLYSIS PARAMETERS: A) 2 AND 5 MOL.% NH ₂ -BDC; B) 17 MOL.% NH ₂ -BDC.....	86
FIGURE 6-32 PHOTOCATALYTIC NH ₄ ⁺ PRODUCTION RATE OF MIXED-LIGAND MOFS BEFORE AND AFTER HEAT-TREATMENT.....	87
FIGURE 6-33 PHOTOCATALYTIC NH ₄ ⁺ PRODUCTION RATE OF MIL-101-FE BEFORE AND AFTER HEAT-TREATMENT... ..	88
FIGURE 6-34 SECONDARY BUILDING UNITS OF FE-TEREPHTHALATE MOFS: A) MIL-53-FE (FeO ₄ (OH) ₂ FROM; B) MIL-101-FE (Fe ₃ O(RCO ₂) ₆ (H ₂ O) ₂ X.....	88
FIGURE 6-35 CHARACTERIZATION OF AS-PREPARED MIL-53-FE: A) XRD PATTERN OF SYNTHETIZED MIL-53-FE IN COMPARISON WITH SIMULATED SPECTRUM OF MIL-53-FE; B) FTIR SPECTRA OF MIL-53-FE.	89
FIGURE 6-36 PHOTOCATALYTIC NH ₄ ⁺ PRODUCTION RATE OF FE-BASED MOFS WITH DIFFERENT SBU.....	90
FIGURE 6-37 J-V CURVES RECORDED IN 0.1 M Na ₂ SO ₄ WITH AG/AGCL ELECTRODE AND PT CATHODE, WITH POTENTIAL REPORTED VS. RHE: A) BDC-NH ₂ LIGAND INFLUENCE; B) SBU INFLUENCE.	91
FIGURE 6-38 CHARACTERIZATION OF CE-UIO-66 AS-PREPARED SAMPLES: A) XRD PATTERN; B) FTIR SPECTRUM.	92
FIGURE 6-39 PHOTOCATALYTIC NH ₄ ⁺ PRODUCTION RATE CE-UIO-66 AND ITS ANALOGUE MIXED METAL CE/ZR-UIO-66 UNDER AMBIENT CONDITIONS.	92

FIGURE 7-1 PROPOSED MECHANISM OF ELECTRON TRANSFER IN THE NH₂-BDC MOF ON THE EXAMPLE OF NRR.... 98

FIGURE 11-1 IN-SITU DRIFTS MEASUREMENTS OF 5%NH₂-MIL-101-FE DURING HEATING UP TO 600 °C WITH RAMP
RATE OF 5 °C MIN⁻¹..... 120

FIGURE 11-2 EX-SITU XRD PATTERNS OF HEAT-TREATED MOFS AT DIFFERENT PARAMETERS: A) SINGLE-LIGAND MIL-
101-FE; B) 17%NH₂-MIL; C) 50% NH₂-MIL; D) 80% NH₂-MIL..... 121

FIGURE 11-3 SEM IMAGES OF 2%NH₂-MIL-101-FE WITH 12 000X MAGNIFICATION: A) BEFORE; B) AFTER
HEATTREATMENT. 122

List of Tables

<u>TABLE 2-1: REDUCTION POTENTIALS (VS. NHE AT PH 0) OF TYPICAL HYDROGENATION REACTIONS RELATED TO THE REDUCTION OF N₂ TO NH₃^{54, 55}.</u>	13
<u>TABLE 5-1: PREPARATION DETAILS OF THE SINGLE-LIGAND FE-MOFS AS WELL AS MIXED-LIGAND FE-MOFS.</u>	37
<u>TABLE 5-2: DIFFERENT HEAT-TREATMENT PARAMETERS OF THE MIXED-LIGAND MOFS.</u>	38
<u>TABLE 6-1 THE MAIN BRAGG REFLECTIONS ASSIGNED TO THE CORRESPONDING PHASES AND FACETS (OBTAINED USING RIETAN FP IN VESTA).</u>	42
<u>TABLE 6-2: THE OPTICAL BANDGAP VALUES OF MIXED-LIGAND MOFS.</u>	61
<u>TABLE 6-3: THE CHARACTERISTIC FTIR BANDS OF NO₂-BDC AND BR-BDC SINGLE-LIGAND MOFS, AND MIL-101-FE AS REFERENCE.</u>	63
<u>TABLE 6-4: NORMALIZED NH₄⁺ PRODUCTION RATE WITH RESPECT TO SINGLE-LIGAND MIL-101-FE.</u>	67
<u>TABLE 6-5: FTIR BAND FOR COMPARISON OF ELECTRON WITHDRAWING EFFECT ON SIGNIFICANT BANDS IN THE SBU.</u>	69
<u>TABLE 6-6: WEIGHT RESIDUE AT DIFFERENT WEIGHT LOSS STAGES.</u>	71
<u>TABLE 6-7: SUMMARY ON OPTIMAL THERMOLYSIS PARAMETERS.</u>	77
<u>TABLE 6-8: BET SPECIFIC SURFACE AREA AND PORE VOLUME OF AS-PREPARED AND HEAT-TREATED SAMPLES.</u>	79
<u>TABLE 6-9: OPTICAL BAND GAP VALUES OF AS-PREPARED AND HEAT-TREATED SAMPLES.</u>	82
<u>TABLE 6-10 DETERMINED PERCENTAGE OF MISSING LIGAND OBTAINED FROM ISOTHERMAL TGA ANALYSIS REPRODUCING THERMOLYSIS PARAMETERS.</u>	86

1 Introduction

1.1 Environmental Sustainability Issues

Ammonia is an indispensable raw material that is widely used in industrial and household chemicals. Furthermore, industrial ammonia production as the first step of fertilizers production is highly important as the nutrition of almost half of the global population relies on it (Fig. 1-1). Ammonia production is associated with significant energy use of more than 1% of global consumption of nonrenewable fuel sources and consequently contributes to more than 1% of carbon dioxide emissions¹.

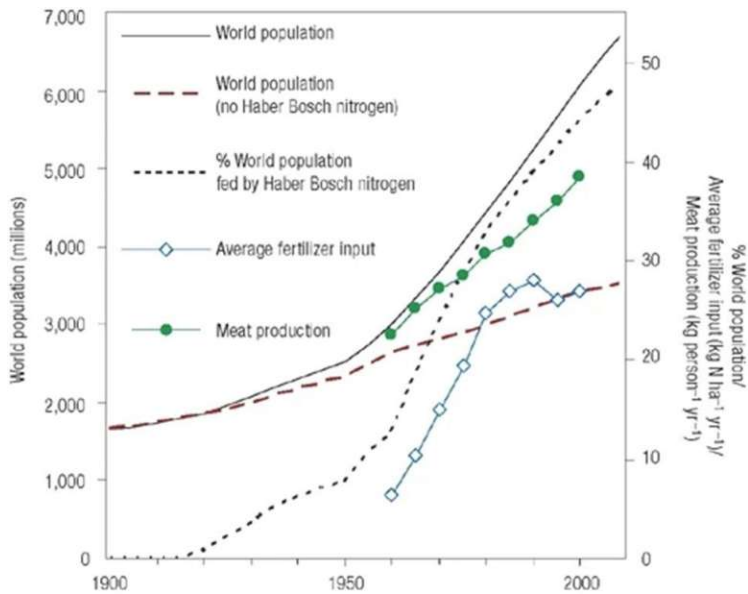


Figure 1-1: Trends in human population and nitrogen use throughout the twentieth century².

In addition, ammonia is also potential hydrogen carrier and distribution media of the future, possessing a high hydrogen content (17.6 wt.%) and large energy density (4.3 kWh·L⁻¹ at -33°C and 1 bar)³. Equally important, ammonia is readily liquefied at atmospheric pressure, enabling the storage and transport of liquid ammonia, contrary to technological challenges regarding the storage and transportation of liquid hydrogen⁴.

In the context of global energy consumption related to the population growth and associated rising demands, alternative chemical energy carriers are required to replace standard fossil fuels. Ammonia is highly attractive as a sustainable energy carrier that can be used in combustion engines as well as fuel cells⁵.

Despite constituting over 78% of the atmosphere, nitrogen exists in a chemically and biologically inaccessible gaseous form, rendering it unusable. In the first decade of the 20th century, German chemists Fritz Haber and Carl Bosch discovered how ammonia, a chemically reactive, feasible form of nitrogen, could be synthesized by reacting atmospheric molecular nitrogen with hydrogen in the presence of an iron catalyst. After the inventors, the process was named the Haber-Bosch process. Fritz Haber created the breakout and laid the foundation for high-pressure chemical engineering and Carl Bosch developed the process on the industrial scale, which was in 1931 awarded the Nobel Prize².

In his Nobel speech, Haber explained that his motivation for ammonia synthesis was the growing demand for food. The large-scale production of ammonia has accelerated the industrial manufacture of a large number of chemical compounds, therefore having a high impact on agriculture and industry. What could not be foreseen at this point was that the industrialization marking modern history had a negative side on the environmental changes upon the increased greenhouse gas levels correlated to air and gas pollution. Thus benefits that raised from industrial development began to have unintended consequences².

Annually, nearly 200 million tons of ammonia are synthesized by the Haber-Bosch process, which takes place under harsh reaction conditions (400 - 500°C, 15-25 MPa). Apart from nitrogen, hydrogen is used as a feedstock which is usually obtained from methane steam reforming leading to more than 300 million tons of CO₂- emissions^{6,7}.

The far-reaching consequences of ammonia production on both society and climate call for the urgent development of alternative production technologies that minimize or completely eliminate CO₂ emissions. So far, the main research interest is green hydrogen production. Besides conventional hydrogen production with reduced CO₂ emissions through coupling to e.g. carbon capture and storage concepts (blue ammonia), green ammonia production focuses on green hydrogen production with subsequent ammonia synthesis⁸.

One largely neglected but emerging approach is photocatalytic nitrogen conversion to ammonia. This process utilizes molecular nitrogen, water as a proton source, and light as the energy source to produce ammonia. This N₂ conversion to ammonia is possible only in the presence of a catalyst

with suitable activity and selectivity. A variety of photocatalytic materials is currently being researched, raising difficulties to comparability and development of comprehensive understandings. The research in the field of photocatalytic nitrogen reduction encounters a lot of challenges⁹.

1.2 Motivation and Aims

This work has been performed in photocatalysis, focusing on photocatalytic nitrogen reduction to ammonia. In recent times, diversified photocatalysts have been explored for N₂ reduction reactions, such as metal oxides [^{10,11,12,13}], metal sulfides [^{14,15}], g-C₃N₄ [^{16,17}], and MXene (Ti₃C₂) [^{18,19}], among others. Nonetheless, the overall conversion efficiency for N₂ reduction is still far from the value required in industry or any reasonable technological interest. This is essentially associated with the challenges of low light utilization, lack of effective active sites, rapid recombination of photoexcited electron-hole pairs, in addition to inertness of N≡N triple bond and poor adsorption and activation capability⁹.

Metal-organic frameworks (MOFs) are hybrid organic-inorganic materials composed of inorganic clusters connected with organic linkers. They provide well-defined active sites resembling the molecular complexes in homogenous catalysis. The coordination bonding with the linkers into the framework provides heterogeneous and isostructural features. Benefiting from the modularity of organic ligands and the inherent optoelectronic properties of different metal ions, MOFs have adjustable structures and exhibit different properties. Up to now, MOFs and MOF-based materials have shown high photocatalytic activity for a lot of reactions. Still, just recently, light-driven nitrogen fixation for ammonia synthesis catalyzed by MOFs has received more attention^{20,21}.

The difficulty lies in the fact that the nitrogen-nitrogen triple bond is very stable. Therefore, searching for a catalyst with both strong nitrogen adsorption and NH₃ destabilization to break the scaling relationship has become a key priority in photocatalytic ammonia synthesis research.

Certain transition metal, have generally been regarded as efficient active species for overcoming the thermodynamic and kinetic barrier in ammonia synthesis, due to their appropriate orbital energy and symmetry²².

Inspired by the structure of nitrogenase enzymes, which is responsible for the biological nitrogen fixation, with electron-donating Fe protein and industrial catalyst used in the Haber-Bosch process, the idea of exploiting Fe-based MOFs as nitrogen fixation photocatalyst has seemed promising^{23,24}.

The first part of the thesis is focused on exploring the influence of ligand functionalization in Fe-terephthalate MOFs on the material functional properties and photocatalytic performance. For that purpose, a series of mixed-ligand and single-ligand MOFs containing differently functionalized terephthalic acid ligands were synthesized, characterized, and applied for photocatalytic nitrogen conversion to ammonia.

The second part of the work focuses on creating open metal sites in the framework structure by post-synthetic modification through thermal treatment. The idea for the thermal treatment was raised from already published work on selective ligand removal strategy²⁵. Finding optimal parameter for the selective ligand removal and its effect on the application-related properties has been studied on a series of mixed-ligand amino-containing Fe-MOFs.

2 Theoretical Background

2.1 Photocatalysis

Photocatalysis is a type of catalysis, in which photons are used to drive or accelerate a chemical reaction. The photon energy typically lies in the range of ultraviolet (UV), visible or infrared (IR) light spectrum. When a material uses photon energy to drive thermodynamically exothermic reaction ($\Delta G > 0$), the process is termed as *photosynthesis*, in that case material is considered as photocatalyst only if the photon is reactant²⁶.

Conversely, a material that uses photon energy to facilitate an exothermic reaction ($\Delta G < 0$), only changing the kinetics of the reaction by changing the reaction pathway fits the definition of the *photocatalyst*²⁶.

Photocatalyst by IUPAC is defined as: "catalyst able to produce, upon absorption of light, chemical transformation of the reaction partners. The excited state of the photocatalyst repeatedly interacts with the reaction partners forming reaction intermediates and regenerates itself after each cycle of such reaction"²⁷.

The photoactive materials can absorb photons and generate excited electrons (e^-), paired with positively charged holes (h^+). These generated charge carriers can then be extracted to drive specific redox reactions²⁶.

The most important essence is the ability of catalyst to drive chemical reactions using photon energy. The pioneers in the photocatalysis field research were Honda and Fujishima with the discovery of photoelectrochemical water splitting over semiconductor material²⁸. After that the research interest in this field grows tremendously, parallel to the growing awareness of sustainability.

Photocatalysis can be divided into homogenous photocatalysis, where both catalyst and reactants exist in the same phase and heterogenous photocatalysis, where the catalyst and reactants have a different phase. In heterogenous photocatalysis, the materials can be categorized into a) molecular photocatalysts, b) semiconducting photocatalysts, c) traditional semiconductor-based

photovoltaic assisted catalysts and d) new material classes including plasmonic metal nanoparticles, quantum dots, 2D materials and metal-organic frameworks^{26, 29, 30}.

In heterogenous photocatalysis, the photocatalyst is often a solid material and a redox reaction between the reactants and catalyst occurs at the interface. The work for this thesis was carried out in heterogenous photocatalysis so the following discussion and more detailed description of relevant photocatalytic systems will be introduced.

2.2 Electronic Properties of Semiconductor Photocatalyst

There are different principles that govern photo-driven reactions and are dependent on the type of photocatalyst. In molecular photocatalysis, the molecular orbital theory is used to describe the system. For semiconducting photocatalysts, the band theory is relevant²⁶. The band theory describes the electronic states of the solids, where the energy levels of electrons lie so close to each other that they can be considered as a continuum, whereas these regions of possible energy levels are called bands³¹.

Two bands in the solid materials are relevant for the semiconductor photocatalysts termed valence band (VB) and conduction band (CB). The energy difference between these two bands is called the bandgap (E_g). The bandgap energy and the distribution of the electrons determine the electronic properties of material. Band theory is employed to distinguish between insulators, semiconductors, and conductors. In the conductors, the electrons are delocalized which means the valence band is either partially filled or it overlaps with the conduction band. Insulators and semiconductors have the same structure, where the width of the forbidden bandgap is different. Semiconductors show a bandgap between 0 and 4 eV, while insulators have a bandgap larger than 4 eV³².

In the context of charge carriers transfer between the semiconductor and redox species, it is crucial to identify the highest occupied and lowest unoccupied electronic levels, since they are involved in the redox reactions. In pristine semiconductor materials, all electronic levels of VB are occupied, whereas the levels in the CB are empty. Thus, the highest occupied level coincides with the top of VB, whereas the lowest unoccupied level of the most semiconductor materials coincides with the bottom of the CB. The band edge positions of the bulk material can be

identified as the ionization potential (I) of a valence band and electron affinity (A) as the energy level of the conduction band³³.

The Fermi level energy (E_f) is the absolute electronegativity $-\chi$ of the semiconductor, corresponding to the halfway between the conduction band and the valence band edges³³.

The relation between the band edge energies can be expressed as:

$$E_c = -A = -\chi + 0.5E_g \quad 2-1$$

$$E_v = -I = -\chi - 0.5E_g \quad 2-2$$

Incorporation of dopants or point defects in the structure leads to the presence of electron acceptor state levels or donor state levels within the bandgap. The presence of a donor or acceptor changes the position of the Fermi level. The introduction of acceptor states leads to p-type semiconductors, in which E_f is positioned just above E_v . Additional donor states shifts the Fermi level towards E_c , creating an n-type of semiconductor³³.

The photocatalytic reaction involves the charge transfer between the catalyst and the redox species. Upon the acceptance of electrons, a previously unoccupied electronic level becomes occupied, whereas upon electron donation an electron is removed from an occupied level. For an electron acceptor, the energy of the lowest unoccupied level is of importance, while for an electron donor, the energy of the highest occupied level is relevant.

Electrons will be transferred across the electrolyte/semiconductor interface until the Fermi levels of the solid and solution are aligned. As a result, the CB and VB edges are bent, establishing a potential barrier against further charge transfer. This the energies of the band edges at the interface deviate from their bulk values³⁴.

Interfacial electron transfer is a complicated process, and it is hindered by different thermodynamic and kinetic factors. At the interface, the electronic states deviate from those of the bulk band edges, therefore, these deviations need to be considered. The electron transfer can only occur at the semiconductor interface if the energy levels belonging to the semiconductor and the redox species are approximately of the same energy. Although the interfacial energetic states are controlling the charge carrier transfer, this simplified approach does not consider the energy change due to chemisorption, which of high relevance in catalytic activity and selectivity³³.

2.3 Perspective of Nitrogen Reduction to Ammonia

2.3.1 Properties of N₂ Molecule

Nitrogen molecules are formed by two nitrogen atoms connected by a strong non-polar N≡N triple bond. Each nitrogen atom possesses a pair of electrons in the 2s orbital and three lone pairs of electrons in the 2p orbitals with parallel spins³⁵. The sp-hybridization leads to the formation of four bonding orbitals (two σ and two π orbitals) and four antibonding orbitals (two σ^* and two π^* orbitals), with the shared electrons in the π and 2σ orbitals forming an N≡N bond³⁶.

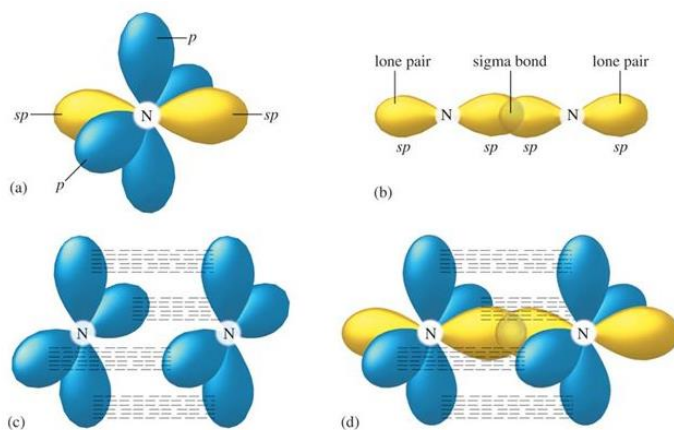


Figure 2-1 Atomic orbital hybridization of nitrogen in N₂³⁷.

The large energy gap between the highest occupied molecular orbital (HOMO) and the lowest unoccupied molecular orbital (LUMO) is 10.82 eV, which makes one or two-electron transfer reactions difficult³⁸. The N₂ molecule is extremely stable and kinetically inert with a binding energy (945 kJ mol⁻¹) and first-bond breaking energy (410 kJ mol⁻¹)³⁹. Among others, an N₂ molecule has both a large ionization potential (15.85 eV) and a negative electron affinity (-1.9 eV), making it difficult to be oxidized or reduced³⁵.

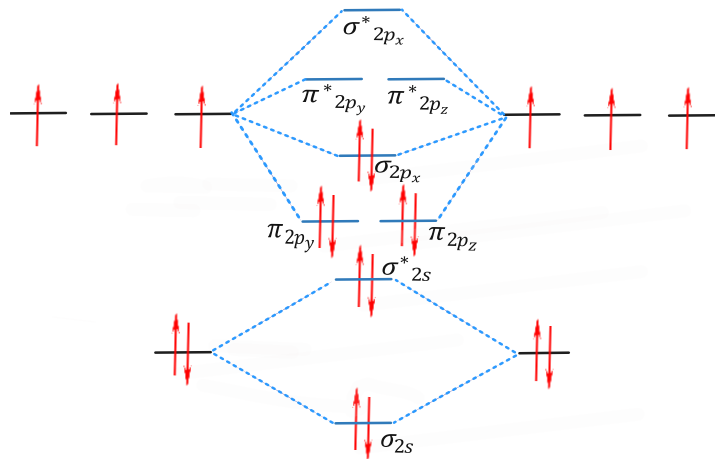
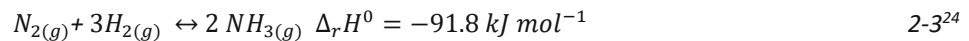


Figure 2-2 Molecular orbital scheme of N_2 , in accordance with⁴⁰.

2.4 Industrial Ammonia Synthesis

2.4.1 Thermodynamic Aspects of Nitrogen Conversion to Ammonia

The conversion of N_2 to NH_3 is slightly exothermic, meaning it is thermodynamically accessible.



The Haber-Bosch process is the main industrial ammonia production procedure, which is based on the thermodynamics of Eq. 4-3. This process converts atmospheric nitrogen to ammonia by reaction with hydrogen using a metal catalyst under high temperatures and pressures⁴¹.

According to Le Chatelier's principle the reaction would be favored at lower temperatures. On the other hand, the conversion rate is lower at lower temperatures. Thus, the compromise between the amount and production rate has to be accomplished. On the left side of the equation are four gas molecules, but only two on the right side. Thus, a higher pressure will favor the formation of the product⁴².

These facts have to be considered and bring a lot of challenges into industrial ammonia synthesis. Two opposing considerations are relevant: the reaction rate and equilibrium position. At low temperatures the reaction rate is nearly undetectable. However, temperature increase shifts the equilibrium position towards products following the Le Chatelier's principle. This is why the higher pressure has to be applied in order to favor the conversion to ammonia⁴³.

Technologically, this increases the costs due to two reasons: firstly, the production and maintenance of high pressures as well as the need for sufficient temperature, increase the energy consumption cost; and secondly, the requirements on pipeline and vessels material, which have to withstand high pressure, result in increased capital cost²⁴.

The catalyst in the Haber-Bosch process does not affect the equilibrium position but speeds up the production rate. The catalyst ensures that the reaction is fast enough for a dynamic equilibrium to be maintained at a very short time when the gases are in reactor vessels²⁴. In the following, I will describe the properties of industrial catalyst in more detail.

2.4.2 Conventional Heterogenous Catalyst for Industrial Ammonia Synthesis

Although the classical heterogeneous ammonia synthesis process is commonly referred to as the Haber-Bosch process, the development of the catalyst was primarily the achievement of Alwin Mittasch at BASF. In the early 20th century, he tested over 2,000 different catalyst formulations in more than 6,000 experiments⁴⁴.

The resulting catalyst was multiply promoted by iron catalyst and could reach the desired activity under the reaction conditions. Early research established that the catalyst's activity is sufficiently high only by using particular precursor material. Thus, by using magnetite (Fe_3O_4) with defined amounts of K_2O and Al_2O_3 promoters, as well as CaO , an active structure can be formed during the reaction. It was proposed that in the presence of ammonia, iron nitrides are formed on the catalyst surface. During the reaction the major bulk part of the material remains as the defective α -Fe phase which is referred as "ammonia iron". These ammonia iron clusters are kept apart by irreducible promoter oxides and surrounded by nitride iron pellets. The function of the oxide promoters is keeping the catalyst particle apart and optimizing adsorption and desorption energies⁴⁵.

Another industrially applied catalyst is the Ru-based catalyst which, due to its high costs, is used in nanoparticle form supported on the oxide or carbon substrates⁴⁴.

The mechanism of the industrial thermocatalytic ammonia synthesis will be described in the following chapter. An important consideration in industrial synthesis is that after the adsorption

of N_2 on the catalyst surface, the dissociation of N_2 has to occur and this step is often the rate-determining step in the overall process.

Through research it has been established that nitrogen activation is highly dependent on the exposure of the active sites. This phenomenon is well-known in the field of heterogeneous catalysis where it is recognized that a rough surface provides more active sites for catalytic process⁹.

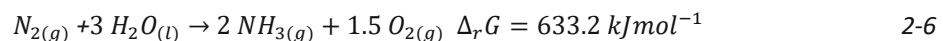
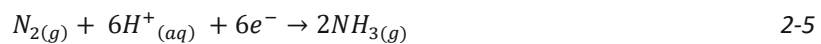
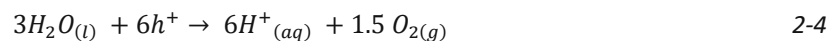
Accordingly, nitrogen activation critically depends on the exposure of the active sites. Due to the better stabilization of the adsorbed nitrogen on the steep sides compared to the bare terrace, nitrogen dissociation can proceed nine orders of magnitude faster at the steep sides⁹. This consideration is of high importance, as nitrogen dissociation is the rate-determining step, and only a small fraction of exposed sites with the appropriate electronic structure can effectively dissociate nitrogen⁴⁵.

Although the reaction pathway in the photocatalytic nitrogen conversion to ammonia differs from the industrial thermocatalytic conversion, the defective structure of the catalyst, its electronic properties and as well as adsorption and desorption energies in the industrial synthesis can be considered as criteria for selecting or designing a photocatalyst.

2.5 Basic Principle of Photocatalytic Nitrogen Reduction

2.5.1 Thermodynamics of Nitrogen Reduction over Semiconductor Photocatalyst

There are two coupled redox half reactions correlated to the photocatalytic nitrogen reduction to ammonia, including the oxidation of water (Eq. 2-4) with photogenerated holes in the valence band and the reduction of molecular nitrogen (Eq. 2-5) with photogenerated electrons in the conduction band, whereas N_2 is reduced to NH_3 after series of multi-step hydrogenation reactions with photogenerated electrons and water-derived protons. The overall conversion is an endothermic reaction (Eq. 2-6)⁹.



The photocatalytic conversion proceeds through three fundamental steps^{46,47,48}:

1. Generation of charge carriers (electrons and holes) by photon excitation under the condition that the photon energy is at least as high as the band gap energy ($E_{hv} \geq E_g$)
2. Separation and migration of electrons and holes to the catalyst surface
3. Redox reaction between surface-adsorbed species and electron-hole pairs, i.e., N_2 reduction producing NH_3 and water oxidation producing O_2 and H^+ .

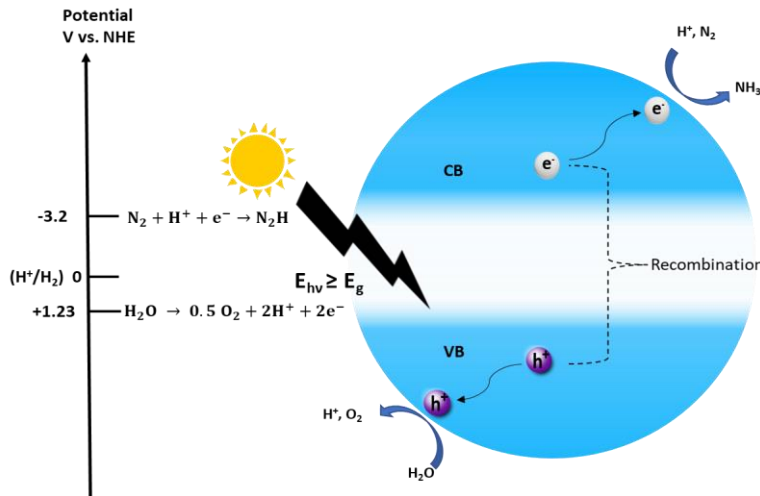


Figure 2-3 Schematic representation of photocatalytic N_2 reduction to ammonia on semiconductor material with band edge positions with respect to NHE at $pH=0$.

As already described in *Section 2.2* the capability of a semiconductor to absorb light and its photoreaction thermodynamics depend on its bandgap and band edge positions. In a photocatalytic nitrogen reduction, there are two coupled half-redox reactions, so it is important to consider the redox potentials of both conduction band electrons and valence band holes to satisfy the thermodynamics of reduction and oxidation reactions^{9,49}.

This means that whether the redox reaction can occur depends on the surface energy levels. The reduction potential of the adsorbate and position of the conduction band should be higher than the reduction potential of the N_2 hydrogenation. The position of the valence band should be lower than the water oxidation potential. The band edge positions of the semiconductor photocatalyst are schematically represented in *Fig. 2-3* with respect to NHE (Normal Hydrogen Electrode).

Elementary electrochemical reactions can be employed to help explain the hydrogenation process. At the very first proton-coupled electron transfer, the N₂ adsorbed on the catalyst surface gains one proton from the environment and one photogenerated electron from the catalyst surface to generate adsorbed hydrogenated chemical species (*N=NH)^{50,51,52}, as shown:



The first electron transfer is the one with the highest energy barrier (-4.16 V vs. NHE at pH=0) or proton-coupled electron transfer (-3.2 V vs. NHE) processes which constrain the overall kinetics of the reaction. Thus, photoexcited electrons need to overcome the maximum energy transition state during either first electron transfer, making this step the most difficult one⁵³. Subsequent conversion to ammonia proceeds through multi-step hydrogenation reactions, as summarized in *Table 2-1*.

Table 2-1: Reduction potentials (vs. NHE at pH 0) of typical hydrogenation reactions related to the reduction of N₂ to NH₃^{54,55}.

Reaction	E ⁰ (V)
$H_2O \rightarrow 0.5 O_2 + 2H^+ + 2e^-$	1.23
$2H^+ + 2e^- \rightarrow H_2$	0
$N_2 + e^- \rightarrow N_2^-$	-4.16
$N_2 + H^+ + e^- \rightarrow N_2H$	-3.2
$N_2 + 2H^+ + 2e^- \rightarrow N_2H_2$	-1.1
$N_2 + 4H^+ + 4e^- \rightarrow N_2H_4$	-0.36
$N_2 + 5H^+ + 4e^- \rightarrow N_2H_5^+$	-0.23
$N_2 + 6H^+ + 6e^- \rightarrow 2NH_3$	0.55
$N_2 + 8H^+ + 8e^- \rightarrow 2NH_4^+$	0.27

Interestingly, in the literature it is not found that a semiconductor satisfying the thermodynamics of single nitrogen hydrogenation would have a bandgap of an insulator. However, as presented in *Table 2-1* the N₂ molecule can be simultaneously hydrogenated with more than one proton and electron, and the redox potentials of these reactions are significantly lower than that of single hydrogenation.

2.6 Possible Pathways of Nitrogen Reduction in Heterogenous Catalysis

Based on DFT studies by Azofra *et al.*, it has been proposed that the first step involves a proton-coupled electron transfer (PCET) mechanism, leading to the formation of N_2H^* species bounded on the catalyst. Subsequently, there are two possible intermediates, hydrazine (N_2H_4) and diazene (N_2H_2) that may participate in the hydrogenation (protonation and reduction) process⁵⁰.

The reduction of N_2 to its intermediates, also involves positive standard enthalpies of formation with values of +212.9 and +95.35 kJ mol⁻¹ for diazene and hydrazine, respectively²².

According to different hydrogenation (protonation and reduction) sequences and the cleavage of $N\equiv N$ triple bond, NRR is generally divided into dissociative and associative mechanisms (Fig 2-4).

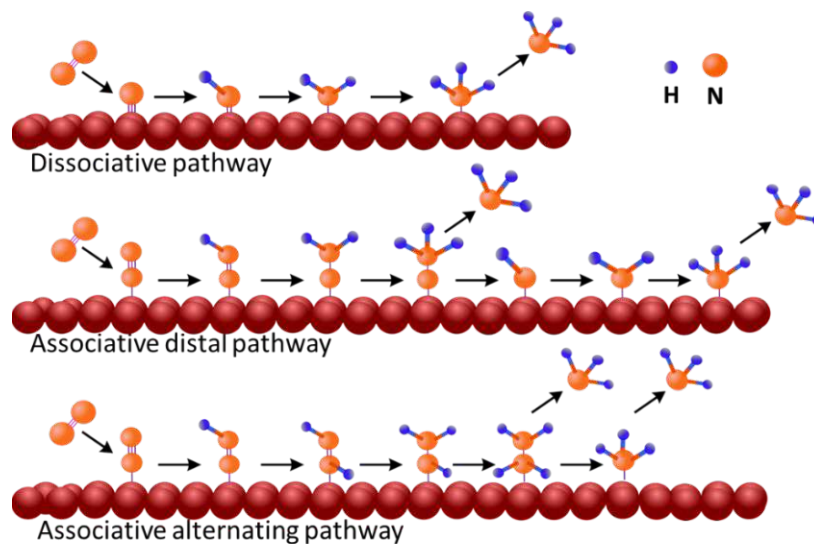


Figure 2-4 Schematic representation of different nitrogen reduction pathways.

In the dissociative mechanism, $N\equiv N$ bond is broken in the adsorption process, which leads to the adsorption of individual N atoms separated by evident distance. Subsequently, atoms are hydrogenated to form ammonia molecule⁵⁶. This mechanism requires high energy input and is the dominant mechanism in the Haber-Bosch process.

In the associative mechanism, the $N\equiv N$ triple bond remains intact after the molecule adsorption and breaks at a certain step in the process of hydrogenation. The associative process can be further generalized into distal and alternating depending on hydrogenation sequences⁴⁹.

In the distal pathway, hydrogenation occurs preferably on the distal N atom away from the catalyst surface to generate NH_3 . After the ammonia molecule is released, the other nitrogen atom on the surface is left for further hydrogenation, which is continuously hydrogenated until the second NH_3 molecule is formed and released⁴⁹.

In the alternating pathway, the hydrogenation occurs on two nitrogen atoms alternatively to $\text{N}\equiv\text{NH}^*$, $\text{HN}\equiv\text{NH}^*$, NH-NH_2^* , and finally, NH_3 . At the last step, the N–N bond breaks with the formation of first ammonia, which leaves one NH_3 behind⁵⁷.

The associative mechanism is a widely accepted mechanism of nitrogen conversion to ammonia in photocatalytic systems⁹.

3 Metal-Organic Frameworks

The prospective of metal-organic frameworks (MOFs) as photocatalyst for nitrogen reduction has been mentioned in *Introduction* but will be discussed here in more detail. MOFs are versatile functional materials with unique properties different from conventional semiconductor photocatalyst. Therefore, the historical development, structural and physiochemical properties of MOFs will be introduced in the following.

3.1 Introduction to Metal-Organic Frameworks

In the late 1990s, MOFs became a fast-growing research field, pioneered by Omar Yaghi at UC Berkeley. In August, 2020, the number of reported MOFs in Cambridge Structural Database (CSD) was 103,951^{21, 58}.

There is a disagreement among the MOFs researchers on the number of MOFs entries in CSD due to the 'ambiguity' in the definition of MOF. The term 'Metal-Organic Framework' (MOF) was first introduced by Omar Yaghi *et al.* in 1995⁵⁹, but it is still ongoing debate about the precise definition of MOFs. MOFs are generally considered as a subgroup of "coordination networks", which, in turn, are a subgroup of coordination polymers⁶⁰.

MOFs can be defined as coordination networks formed with organic ligands having "potential voids" (IUPAC)⁶¹. However, some scientists do not agree with this convention⁶⁰. Generally, the researchers agree that MOFs are crystalline materials with metal atom-centered clusters (metal nodes or metal ions) connected by organic linkers through covalent or ionocovalent bonds forming multidimensional networks (Fig. 3-1).

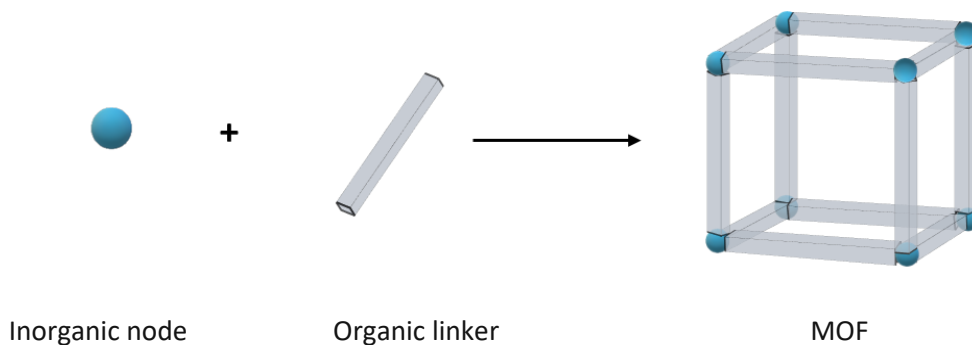


Figure 3-1 General schematic representation of the structure of metal-organic frameworks.

Before the discovery of MOFs, many researchers focused on assemblies of single metal ions and neutral donor linkers in order to construct a coordination network that could accommodate guest solvent molecules in their pores. These compounds were unstable and would collapse upon removing the guest molecules due to the coordination geometries based on single metals^{62, 63, 64}.

This issue was overcome in 1999 in the group of Omar Yaghi by using metal carboxylate cluster chemistry. It was published that 1,4-dicarboxylate (BDC) ligand forms rigid structure and 3D-framework of permanent porosity in Zn-based MOF named MOF-5⁶⁵.

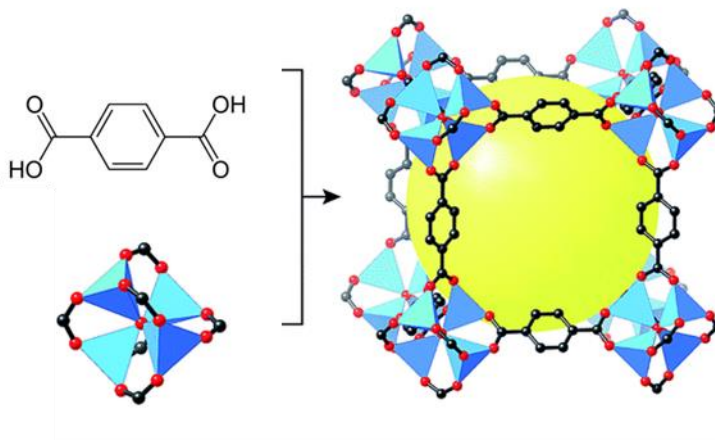


Figure 3-2 Illustration of 3D-MOF with permanent porosity: In the left $Zn_4(O)O_{12}C_6$ cluster of MOF-5 with ZnO_4 tetrahedra indicated with blue; O-red; C-black and bridging BDC ligand; In the right the framework cavity in $Zn_4(O)(BDC)_3$ represented as yellow sphere⁶⁵.

The representative example of MOF-5 constructed with coordination chemistry is used to describe the assembly process in MOF structure. The inorganic metal cluster is composed of ZnO_4 tetrahedra. Each cluster has an oxygen atom bonded to 4 Zn-atoms, whereas 4 Zn-centered tetrahedrons are bridged with carboxylate ligands resulting in $Zn_4(O)O_{12}C_6$ clusters as building blocks of the framework. The terephthalic acid ligand connects two metal centers with each bidentate function forming a 3D network⁶⁵.

Therefore, using the polynuclear inorganic cluster can provide a thermodynamically and mechanically stable environment, due to the entanglement of metal atom centers *via* chelation and bridging of polydentate ligands⁶⁶. These molecular complexes or cluster entities are building blocks of the MOFs termed secondary building units (SBUs) (Fig 3-2). Ligand coordination mode and metal coordination environment are utilized in the transformation of these structural fragments into extended porous networks. They are sufficiently rigid because metal ions are locked into their positions by ligands. Through the coordination bonding they are also neutral, meaning that there is no need for counterions in their cavities⁶⁷.

MOFs are also referred to as structures varying from 0D, 1D, 2D and up to 3D frameworks. Describing MOFs as crystalline material does not necessarily imply a solid, robust structure, but the main research focus is on three-dimensional framework structures accompanied by robustness and high porosity if the molecules are kept intact. The arrangement of the structure

is governed by the physiochemical properties of the constituents. The impact of SBUs on pore size and porosity can be achieved using different linkers. Using a longer linker can increase the spacing between the metal centers, which yields to increase of net void space termed as expansion⁶⁷.

Therefore, MOFs exhibit a typically large surface area, structural flexibility, tunable porosity, variable organic functionality as well as physical and thermal stability⁶⁸. The extraordinary degree of variability of both organic and inorganic constituents makes MOFs interesting materials for a broad range of applications. So far, different synthesis and characterization methods let to a plethora of different MOFs, with different application like sensing, water purification, catalysis, gas storage and separation, drug delivery and many more^{69, 70, 71, 72}.

3.2 Structural Features of MOFs Photocatalyst

An essential feature of MOFs is the high number of active metal sites, which are uniformly spatially distributed. The presence of pore entrances in the frameworks enables penetration of the reactant molecules. In contrast to other porous heterogenous catalysts, like zeolites and mesoporous metal–silicates, segregation of the active metal to form metal oxide species, which is highly undesirable for good catalytic performance, is hardly possible in the case of MOFs⁷³.

Another important aspect is that the porous nature and stability of the coordination networks provides unique structural features that differ from the common features of both homogenous and heterogenous catalysts.

In homogenous catalysis the catalysts have large number of specific active sites, high initial turnover frequency (TOF), well-defined structures and established reaction mechanisms. However, the drawback points of homogenous catalysis are low total turnover number because they are chemically and thermally unstable, tend to agglomerate and thus are limited in reaction number. In heterogenous catalysis the number of active sites is limited to the surface and the initial TOF is low. Furthermore, the structure is undefined disabling the possibility for reaction mechanism studies^{74, 75, 76}.

Through their hybrid heterogenous and isostructural features MOFs have distinct characteristics benefiting from both and gaining an extra contribution from interface. They hinge to application in which general requirements of single-site catalyst are desirable^{77,78}.

3.3 Prospective of MOFs for Photocatalytic Nitrogen Reduction to Ammonia

MOFs are attractive candidates for photocatalytic ammonia synthesis due to the infinitely tunable properties and ability for systematic photocatalyst development. MOFs offer a modular design of photocatalysts with desirable properties that allow fundamental studies on the structure activity relationship and reaction mechanisms²⁰.

In contrast to metal oxides^{79,80}, metal sulfides^{14,81}, and carbonaceous materials^{82,83,84} which are focus of current research MOFs are considered as candidates for NRR due to the following advantages²⁰:

- a) The porous structure enables N₂ to participate in the reduction reaction inside the pores, thereby reducing the migration distance of photo-generated electrons and holes.
- b) The crystalline porous structure of MOFs enables more efficient charge separation improving utilization efficiency.
- c) Both metal nodes and organic ligands in MOFs are adjustable, so that spectral light response can be tailored to improve the absorption efficiency.
- d) The dynamic equilibrium of weak coordination bonds can provide free metal sites for nitrogen adsorption.
- e) Furthermore, as the number of H atoms increases during reaction, the present bond acceptors such as O, N or halogens around the metal centers can form hydrogen bonds with the intermediate making it more stable and so promote the photocatalytic coverion^{20,85}.

In addition to general potential, coordination bonding in MOFs provides intrinsic stability enabling defect engineering and creating open metal coordinatively unsaturated active sites (CUS) that are capable of back-donating electrons to N₂ molecules⁸⁶.

3.4 Fe-based MOFs

In general transition metals with modest number of d-electrons have been regarded as efficient active species for the energy barrier and kinetic challenge in NH_3 synthesis. The ability to break the inert $\text{N}\equiv\text{N}$ triple bond arises from their unique electronic structures with unoccupied and occupied d-orbitals, which are of appropriate symmetry and energy for accepting from and back-donating electrons to nitrogen molecules, termed as π backdonation^{19,22}.

This knowledge can be applied to Fe-based MOFs. The empty d-orbitals of metal sites in MOFs could accept electrons from the occupied σ orbitals of N_2 , while at the same time the occupied d-orbitals can donate electrons to the empty π^* orbital of N_2 . Thus, weakening the $\text{N}\equiv\text{N}$ bond and strengthening the metal-nitrogen bonds leaving the activated N atoms feasible for further hydrogenation⁸⁷.

Since, in this thesis MIL-101-Fe MOF with different functionalities has been studied, its fundamental properties will be described.

3.4.1 MIL-101(Fe)

MIL-101(Fe) is an iron-based metal-organic framework with multiscale pore structure. It is one of the most representative MOFs in the MIL-n series, where 'MIL' stands for Materiau de l'Institut Lavoisier⁸⁸.

In 2005, Férey *et al.* discovered Cr-MIL-101, an isostructural chromium (III) terephthalate MOF. Their aim was to design a catalyst with large pores that could function as nanoreactors, thereby confirming the concept of a priori MOF design through targeted chemistry and computational modeling. The simulated PXRD pattern of MIL-101(Cr) was experimentally confirmed⁸⁹. Three years after this work, Bauer *et al.* synthesized an iron(III) analogue, Fe-MIL-101^{90,91}

The unit cell of MIL-101 consists of metal (III)-trimers crosslinked by terephthalic acid (1,2-dicarboxylic acid or BDC). Each trimer comprises three octahedra corresponding to 6-fold coordination of metal atom with four oxygen atoms of the bidentate BDC ligand, and one μ_3 -O atom. Among these three trimers, two feature a bound water molecule, while the third one is bonded to a halide or hydroxide ion, depending on the synthesis conditions.

Each octahedron is bridged laterally to another one by the carboxylic groups of two BDC molecules on both sides, resulting in a total of four connections with the other two octahedrons and a grand total of six bridging BDC ligands in the SBU⁹².

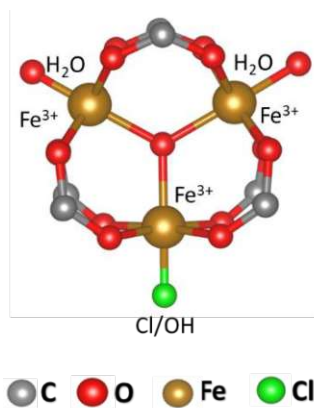


Figure 3-3 Ball and stick model of SBU unit of MIL-101-Fe ($(M_3O(H_2O)_2X(O_2CR)_6)$). Drawn with VESTA.

By crosslinking with the BDC ligand, trimeric SBU forms a super tetrahedron (ST). The μ_3 -oxo atom is located on the one vertex toward the center of the trimer. The trimers occupy the four vertices of the SBU tetrahedron, whereas the organic ligands represent the six edges of the super tetrahedron to give a microporous structure, with ~ 0.86 nm free opening for the windows⁹².

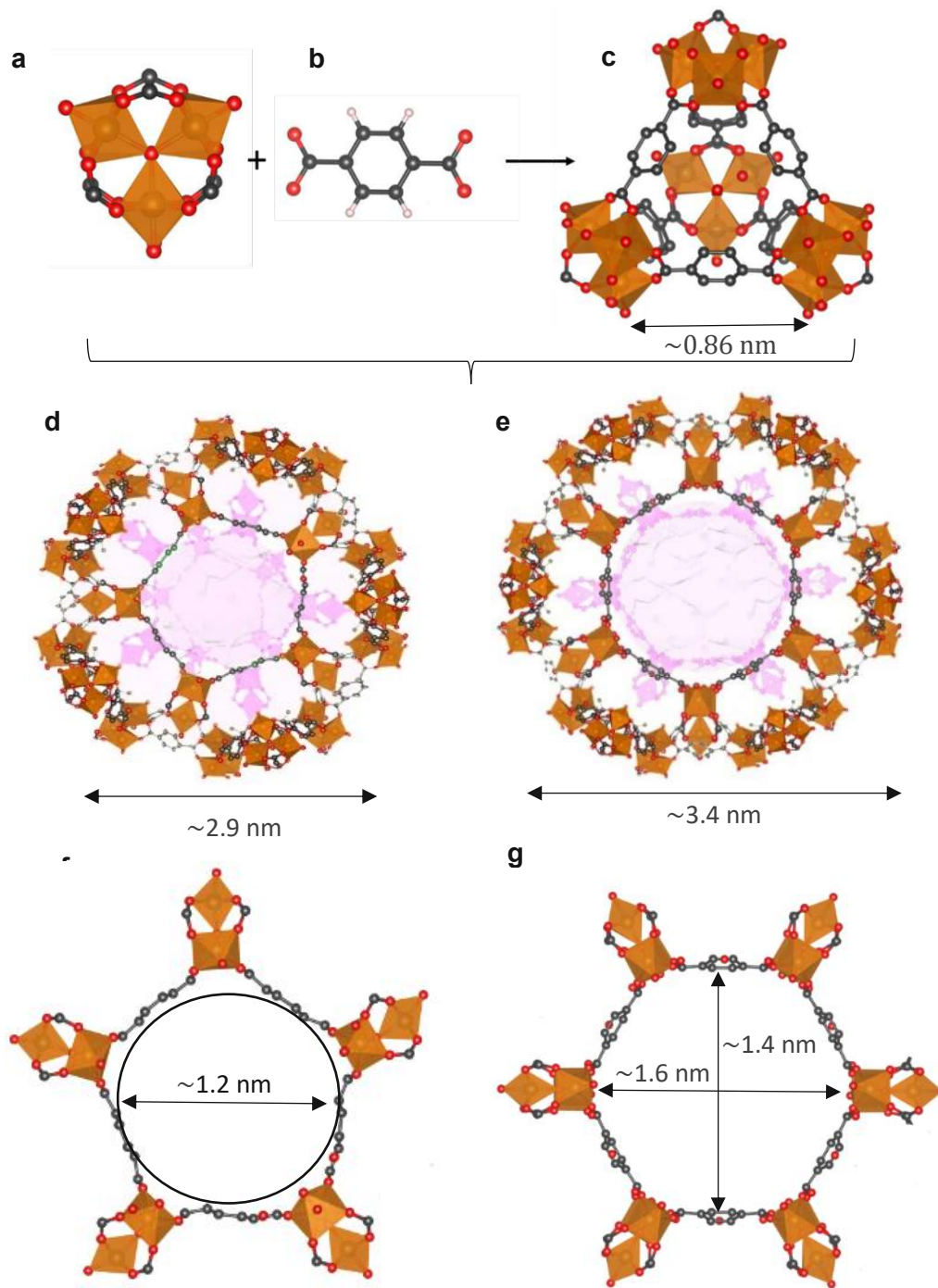


Figure 3-4 Schematic representation of MIL-101 (Fe) metal-organic framework: a) trimeric secondary building unit bridged by three carboxylic functions; b) terephthalic acid ligand, which lies at c) edges of the ST, d) smaller cage with f) pentagonal window, e) larger cage with g) hexagonal window. All structures were drawn in VESTA Software.

The connection of the SBUs propagates through the vertices forming two types of cages marked as 20 and 28 STs. The smaller cages enclose 2.9 nm diameter pores accessible through pentagonal shaped windows of ca. 1.2 nm. The larger cages possess internal diameters of 3.4 nm that exhibits a hexagonal-shaped window with 1.45 and 1.6 nm large openings. Two cages are embodied in the structure with a ratio of 2:1. The resulting architecture is a 3D corner-shared framework with mobil thirty-nine (MNT) zeotype structure⁹⁰.

From the point of view of HSAB ("hard and soft acids and bases") Fe^{3+} as hard Lewis's acid reacts with hard Lewis's bases (carboxyl-based ligands) forming hydrolytically and chemically stable MOFs. It was reported that the MIL-101 was stable over months under air atmosphere and was not altered after treating with various organic solvents at room temperature⁹⁰.

As already described in the structure evaluation, one of the three octahedrally coordinated metal ions are bound to the water molecules. According to the Hwang *et al.* (2009) this terminal water molecules can be easily removed by thermal treatment under vacuum, thus providing catalytically active coordinatively unsaturated sites (CUS)⁹³.

4 Methods

4.1 Powder X-ray Diffraction (PXRD)

Powder X-ray diffraction is a non-destructive technique used for determining phase composition, crystallite size, preferred orientation, crystal structure, layer thickness of films, the amount of amorphous phase or lattice strain (stress-strain analysis)⁹⁴.

The term diffraction is used to describe the phenomena that occurs when electromagnetic waves pass through or around an obstacle. X-ray diffraction is a phenomenon in which the atoms of a crystal, by virtue of their uniform spacing, cause an interference pattern of waves present in a incident X-ray beam. The beam of X-rays contacts a crystal with an angle of incidence θ and is reflected off the atoms of the crystal with the same angle θ . The interference pattern is formed when the X-rays reflecting off two different planes interfere constructively. The conditions which must be fulfilled for the constructive interference is that the difference in path length between the beams reflecting off two atomic planes must be a half integer multiple of the wavelength, which is formulated in a Bragg law⁹⁴:

$$n\lambda = 2d \sin \vartheta$$

4-1⁹⁴

n an integer
 λ wavelength
 d lattice plane spacing
 θ incidence angle.

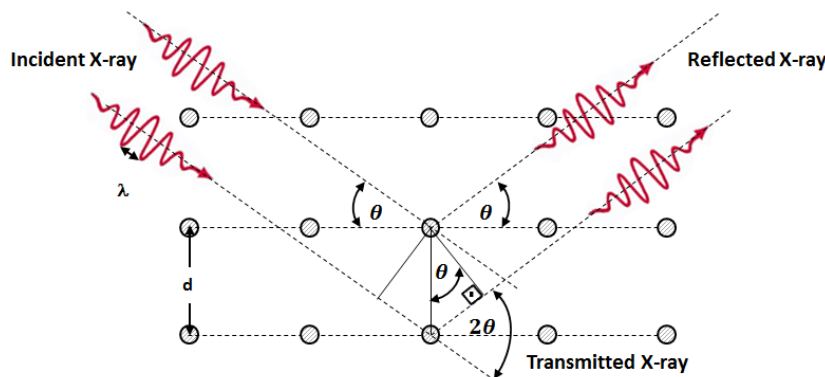


Figure 4-1 Illustration of Bragg's diffraction law: d – lattice place spacing; ϑ – angle between the lattice plane and incident beam (Bragg angle)⁹⁵.

From the positions of the reflexes, the lattice parameters can be derived as hkl-indices. The XRD can also be used for determining the atomic positions, vibration parameters and phase compositions, as well as crystallite size from the full-width half-maximum (FWHD). However, in this work the patterns were compared to the reference patterns from the database. It should be mentioned that the XRD is not a chemical analysis, since the crystal structure is not characteristic of an elemental composition. It provides just the crystallographic information, meaning that XRD pattern is identical for a crystallographic isotype.

The analysis is also semi-quantitative, so that the relative amount of different phases can be determined, but not the absolute one. The diffraction pattern can be influenced by the texture of the sample, where the crystallites of preferred orientation can show a higher intensity.

For the PXRD measurement the samples were grounded and placed as powders on silicon single crystal sample holder. All PXRD measurements were carried out using PANalytical X'Pert Pro multi-purpose diffractometer (MPD) in Bragg Brentano geometry operating with a Cu anode at 45 kV, 40 mA, equipped with a BBHD Mirror and an X-Celerator multichannel detector. The detector records the signal intensity as a function of an incidence angle giving a diffractogram as a graph of intensity versus 2θ , where the samples were scanned between 2θ angle of 5° and 50° .

Sample holders were rotated with 4 s per turn during the measurement. All measurements were conducted with Cu sealed tube K_{α} and K_{β} radiation (2:1 ratio) with a wavelength of $\lambda=1.54060 \text{ \AA}$ at a scan rate of $0.5^{\circ} \text{ min}^{-1}$ ²⁵.

4.2 Thermogravimetric Analysis (TGA)

Thermogravimetric analysis is a thermal analysis method in which the mass of a sample is measured over time as a function temperature profile. This method provides information about specific weight loss due to physical changes as phase transition, absorption, adsorption as well as chemical phenomena like chemisorption, thermal decomposition or solid-gas reactions. Depending on the atmosphere different reactions such as oxidation or reduction can occur⁹⁶.

The TGA experiment can be performed either with a constant heating rate (dynamic method), at a constant temperature (isothermal) or by combining both of them. The heating rate during the should not be too high to cause overheating in a case of exothermic reaction and to be sufficiently slow in order to follow individual changes⁹⁶.

TGA measurements were conducted on a PerkinElmer Thermogravimetric analyzer 8000 (Waltham, USA), using an aluminum oxide (Al_2O_3) crucible. Air was used as treatment gas and the samples were heated up to $800 \text{ }^{\circ}\text{C}$ with a ramp rate of $10 \text{ }^{\circ}\text{C min}^{-1}$.

The isothermal analysis was conducted using the experimental parameters from heat-treatment in order to obtain the relative weight loss after the treatment.

4.3 Physisorption

MOFs have high surface area which can be analyzed with physisorption to obtain the information about surface area and pore size distribution.

Adsorption can be defined as the enrichment of molecules, atoms or ions in the proximity of the interface. Depending on the type of intermolecular forces adsorption can be physical (physisorption) or chemical (chemisorption). In chemisorption, which will not be discussed further, the intermolecular forces involved lead to the formation of chemical bonds. Whereas, the physisorption occurs due to attractive dispersion forces, short range repulsive forces and

specific molecular interactions and is related to the geometric and electronic properties of adsorbent and adsorptive⁹⁷.

The term adsorption denotes the onward process of adsorption, while its counterpart is desorption as inverse process. Those two terms are used to indicate the direction from which experimentally obtained amounts of adsorptive have been detained. In case the adsorption and desorption curves do not coincide arises an adsorption hysteresis⁹⁷.

The adsorption isotherms represent the relation between the amount adsorbed (or the surface excess amount), and the equilibrium pressure of the gas. The surface of porous adsorbent material can be divided into an external and internal surface denoting two different approaches⁹⁷:

1. In general:
 - a) External surface is the surface outside the pores.
 - b) Internal surface is surface of all pore walls.
2. In the presence of microporosity – the external surface is a non-microporous surface.

The accessibility of pores is dependent on the size and shape of adsorptive so that the recorded values depend on its dimensions. Another important factor is the pore morphology which describes the geometrical shape and structure of pores including the pore width and volume⁹⁷.

Porosity of a material is defined as amount of the total pore volume to the volume of the whole particle or agglomerate⁹⁷.

In the context of physisorption, it is preferential to classify pores according to definition by IUPAC⁹⁸:

1. Pores with widths larger than 50 nm are called *macropores*;
2. Pores with widths between 2 nm and 50 nm are called *mesopores*;
3. Pores with widths smaller than 2 nm are called *micropores*.

The term nanopore refers to all of three categories of pores, but with an upper limit of ~100 nm. In the mesopores the physisorption takes place in three nearly distinctive stages. In *monolayer adsorption* all adsorbed molecules are in contact with the adsorbent surface layer. In *multilayer*

adsorption space consists of more than one layer of molecules so that not all adsorbed molecules are in contact with surface of the adsorbent. In mesopores, the multilayer adsorption is followed by *capillary condensation*.

Capillary condensation is a phenomenon whereby gas condenses to a liquid-like phase in a pores at pressures lower than saturation pressure p^0 of the bulk liquid. The equilibrium vapor pressure above curved liquid surface is dependent on the mean radius of curvature r_k of its meniscus. This relation is given by the Kelvin equation⁹⁹:

$$\ln \frac{p}{p^0} = - \frac{2\gamma v^1 \cos\theta}{r_k R T} \quad 4-2$$

γ surface tension

v^1 the molar volume of liquid condensate

R the gas constant

T temperature.

4.3.1 Classification of Physisorption Isotherms

In the 1985 IUPAC recommendations physisorption isotherms were classified into six types¹⁰⁰. To a large extent this classification is based on the experimental work of Everett (1967), Burgess *et al.* and others¹⁰¹.

The interpretation of physisorption hysteresis is important in the context of pore structure characterization.

Reversible **Type I** isotherms are characteristic of microporous solids with relatively small external surfaces. A type I isotherm is concave to the p/p^0 axis. Amount of adsorbed molecules approaches a limiting value due to the accessible micropore volume. The steep uptake is a result of micropore filling at very low p/p^0 . The type 1a and 1b are to distinguish referred to the different pore size distribution range, whereas the later one shows a broader range and does not exclude the possibility of narrow mesopores, not bigger than 2.5 nm⁹⁹.

Type II isotherms are a result of physisorption of the gases on nonporous or microporous materials. The shape is result of unrestricted uptake of gas molecules up to high p/p^0 . There is difference between the sharp change in curvature and the more gradual one. The former one is correlated to clear distinction between monolayer coverage and multilayer adsorption, whereas

the latter is indication of a significant amount of overlap of monolayer coverage and the beginning of multilayer adsorption⁹⁹.

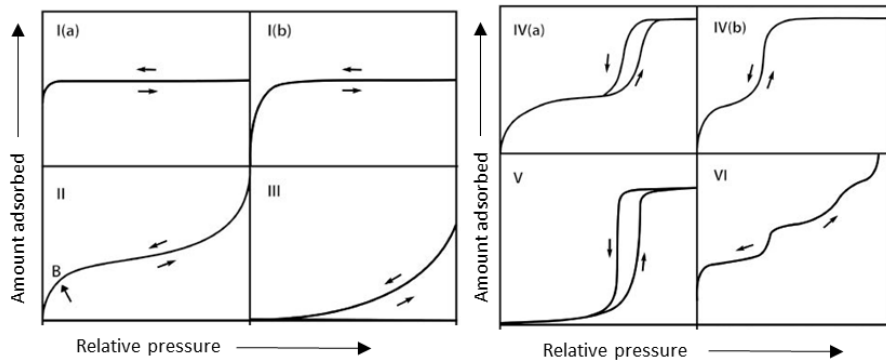


Figure 4-2 Classification of physisorption isotherms by IUPAC⁹⁹.

In the case of **type III** isotherms, there is no distinguishable monolayer formation. These isotherms are characteristic for materials in which the adsorbent-adsorbate interactions are relatively weak. Adsorbed molecules are clustered around the sites on the surface of microporous or even non-porous material. The amount adsorbed molecules remains limited at the saturation pressure⁹⁷.

In type **IVa** isotherms, capillary condensation results in hysteresis. This occurs when the pore width overreaches a critical value depending on adsorption system and temperature. For example, using N₂ or Ar as adsorptive at 77 and 87 K respectively, hysteresis starts forming after exceeding pore width of ~100 nm. The adsorbent with mesopores of smaller pore widths is showing the completely reversible **IVb** isotherms⁹⁷.

In the case of **type V** isotherms, the shape at very low p/p^0 resembles type III and can be assigned to the weak adsorbent-adsorbate interactions. This cluster formation is followed by the pore filling at higher p/p^0 ⁹⁷.

The reversible stepwise **type VI** isotherm is characteristic for layer-by-layer adsorption on the surface of highly uniform non-porous solid. An example of this type of isotherm can be found in the graphitized carbon blocks⁹⁷.

4.3.2 The Origin of Hysteresis

Reproducible hysteresis loops of the multilayer adsorption are generally associated with capillary condensation. This form of hysteresis can be attributed to the adsorption mechanism and or network effects, which leads to classification of hysteresis loops (*Figure 4-3*)

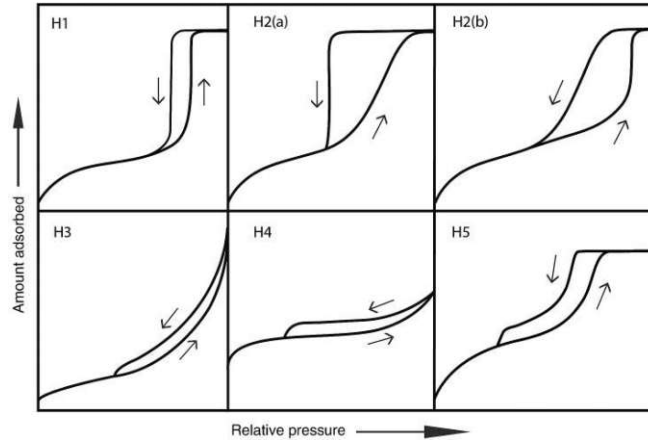


Figure 4-3 The four types of hysteresis loop defined by IUPAC⁹⁹.

4.3.2.1 Hysteresis Loops of Types H1 and H2

The hysteresis loop of **types H1** and **H2** in *Figure 4-3* are characteristic for a variety of mesoporous oxide xerogels and different forms of porous glass, which can be regarded as rigid. They have a well-defined plateau at high p/p^0 , therefore enabling defined mesopore volume. Materials with this hysteresis type exhibit a narrow range of uniform mesopores. The steep narrow loop is due to the delayed condensation on the adsorption branch. However, the type H1 hysteresis can also be found in the networks of ink-bottle pores where the width of the neck size distribution is similar to the width of the pore size distribution⁹⁹.

Hysteresis types of more complex pore structures are given by H2. The steep desorption branch, which is a characteristic property of H2(a) loops a can be attributed to the pore blocking in narrow range of pore necks or to cavitation- induced evaporation. Type H2(b) is also related to the pore blocking, but the size distribution of necks is now much larger. Desorption from these large cavities is determined by the neck size⁹⁹.

4.3.2.2 Hysteresis Loops of Types H3 and H4

There are two different features of the **type H3** loop. The one in which the adsorption branch resembles type II isotherm and second one - the lower limit of the desorption branch is normally located at the cavitation – induces p/p^0 . The H3 loop does not have a plateau at high p/p^0 values, so there is no well-defined mesopore volume. Although, only the initial section of isotherm is reversible, the whole adsorption branch has same shape as the type II isotherm⁹⁹.

The **H4 hysteresis loop** is similar to the H3, except the adsorption branch is composite of type I and type II. The initial region corresponds to the reversible region of micropore filling, which is followed by multilayer adsorption and capillary condensation⁹⁹.

The **H5** hysteresis loop has characteristic form associated with solids containing both open and partially blocked mesopores⁹⁷.

4.3.3 Principles of the Brunauer-Emmet-Teller (BET) Method

The Brunauer-Emmett-Teller method is the most widely used procedure for determining the surface area of porous and finely defined materials. It is a theoretical concept for multilayer adsorption, with assumption of solely van-der Waals interaction between single monolayers. Under certain well controlled conditions, the BET surface area of non-porous, microporous, and mesoporous solids can be regarded as accessible area for adsorptive molecules^{100,99}.

The first step in applying BET is transformation of physisorption isotherm into the BET plot and derivation of value for the BET monolayer capacity, n_m . In the second step, the BET surface area is calculated from n_m by fitting of molecular cross-sectional area (C)⁹⁷:

$$\frac{p/p^0}{n(1-p/p^0)} = \frac{1}{n_m C} + \frac{C-1}{n_m C} (p/p^0) \quad 4-3$$

n specific amount adsorbed at relative pressure p/p^0

n_m specific monolayer capacity.

According to the BET theory, parameter C is exponentially related to the energy of monolayer adsorption. And gives an indication of the shape of the isotherm in the BET range.

The physisorption isotherms were measured at Quantatec iQ2 instrument (Anton Paar, Boynton Beach, FL, USA). Before measurements the samples were heated at 150 °C over night to remove adsorbed gases and moisture. The physisorption measurements were carried out at 77K with nitrogen gas as adsorbate.

4.4 Spectroscopy Techniques

4.4.1 Diffuse Reflectance Spectroscopy (DRS)

Diffuse reflectance spectroscopy is a subset of absorption spectroscopy. The principle relies on reflection or back-scattering of light by a material. It can also be termed as remission spectroscopy where remission includes both specular and diffusely back-scattered light. In contrast to specular reflectance, where light is being reflected in such a way that the incident angle equals the reflected angle, diffuse reflectance means that incoming light is scattered in all directions. This type of reflectance is typically seen by rough samples, whereas specular reflectance occurs on the smooth surface, where the scale of surface roughness inhomogeneities is smaller than the incident wavelength. Like in the other absorption techniques, the sample absorbs photons of specific energy attaining the information on the sample optical properties¹⁰².

DRS is typically performed with wavelength between UV and mid-IR regions, where the diffuse-reflectance ultraviolet–visible spectroscopy implies on wavelengths in UV-Vis region.

In this work, DRS was used as a method to characterize optical properties of a catalyst in powder form. A Jasco V-670 Spectrometer with a sample holder for powder samples and an insert including integrated sphere was used for DRS measurements. The incident light was of 200 nm to 800 nm. MgSO₄ was used as baseline. Reflectance was converted according to Kubelka-Munk equation.

4.4.2 Attenuated Total Reflectance Fourier Transform Infrared Spectroscopy (ATR-FTIR)

Infrared spectroscopy is the analysis is an absorption spectroscopy technique, where the interaction of infrared light with a molecule is studied. The sample is irradiated with light of a specific wavelength and the intensity of the transmitted light is measured. Infrared light has less

energy than visible or UV light and cannot excite electronic energy levels. The mid-infrared, approximately $4000\text{--}400\text{ cm}^{-1}$ ($2.5\text{--}25\text{ }\mu\text{m}$) is generally used to study the fundamental vibrations and associated rotational–vibrational structure. The characteristic vibrational or rotational mode can be excited and assigned to functional group. Based on the structure the molecules absorb IR light of a characteristic frequencies, where this absorption occurs at resonant frequency, i.e. the one that matches the vibrational or rotational frequency. The energies are affected by the shape of the molecular potential energy surface, the masses of the atoms and the vibronic coupling¹⁰³. Generally, stronger bonds and light atoms will vibrate at higher frequencies.

Infrared spectroscopy was used as a method to identify the synthesized catalyst and compare the vibrational modes with expected one from literature. On the other relative intensities of characteristic peaks belonging to organic linkers of MOFs could be compared, the changes induced after the thermal treatment as well as the effect of photocatalytic experiments on the catalyst.

There are several measurement techniques for a transmission mode or the fabrication of a compact KBr sample mixture, but for powder samples ATR is the one with advantage of simple sample preparation. In the ATR-FTIR, the powder is pressed against the ATR-crystal and the infrared light is sent through the crystal while getting reflected through total internal reflection. When the light hits the interface of the sample and crystal, part of the wave travels out of the crystal into the sample as an evanescent wave (penetration depth between 0.5 and $2\text{ }\mu\text{m}$, with exact value determined by the wavelength, the angle of incidence, the probed medium and the indices of refraction. After the absorption occurs, the light gets reflected back internally and sent to the detector¹⁰⁴.

FT stands for a Fourier transformation, in which an FTIR spectrometer collects spectral data over a wide range of a spectrum and then converts the raw data into the actual spectrum using Fourier transformation¹⁰⁵.

4.4.3 Ultraviolet Visible Spectroscopy (UV-Vis)

UV-Vis Spectroscopy was used for determining ammonia production yield via Nessler's reagent method which will be described in the experimental part. UV-Vis spectroscopy probes the wave-

like nature of electrons and their interaction with electromagnetic waves. When a material is irradiated with an electromagnetic wave, different phenomena such as absorption, transmission, reflection or scattering can occur. Absorption occurs when the energy of incident light is equal to energy difference between molecules ground and excited state. UV-Visible Spectroscopy can be divided into ultraviolet (180-400 nm), and visible (400-800 nm). The spectrometer measures the transmittance of the amount of light which is transmitted through the sample. The intensity of the incident light (I_0) with respect to the transmitted light is expressed as ratio $T=I/I_0$ ¹⁰⁶.

The relationship between absorbance and transmittance is described in percentage using equation¹⁰⁷:

$$abs = 2 - \log \frac{I}{I_0} \cdot 100 \quad 4-4$$

Absorbance measurements are commonly used for determining the samples concentration by apply Lambert-Beer Law which describes how light is attenuated by passing through the sample¹⁰⁷:

$$A = \varepsilon \cdot c \cdot l \quad 4-5$$

A ... Absorbance
 ε ... molar absorptivity
c ... sample's concentration
l ... cuvette pathlength.

The amount of absorbed light depends on the concentration of sample. For comparison of two different samples there should be a constant variable to normalize data on it and is measured as background.

4.5 Microscopy Techniques

4.5.1 Scanning Electron Microscopy (SEM)

Scanning electron microscopy is technique used for imaging of microstructure and morphology of the materials by scanning the surface with a focused electron beam. In SEM electron beam with low energy is radiated on the material and scans the surface of the sample. Through the interaction of electrons with the sample surface, several signals are produced leading to emission of photons and electrons from or near the sample surface. As the electron beam is scanned in a raster scan pattern, the intensity of detected signal is used to produce an image¹⁰⁸.

Upon impact, the electrons interact elastically or inelastically with the specimen and depending on the acceleration voltage they penetrate the sample up to a specific depth. Inelastic interaction with specimen atoms can react differently which leads to different effects such as Auger electrons, characteristic X-rays or eject weakly bound valence electrons called secondary electrons (SE)¹⁰⁸.

Secondary electrons have a low kinetic energy ($E_{SE} \sim 1 - 20$ eV), which allows only the surface near electrons to escape the reach the detector. Secondary electrons enable morphological and topological imaging. Due to increased intensity of SE at higher incidence angles leading to a brightness contrast at a particular surface features¹⁰⁸.

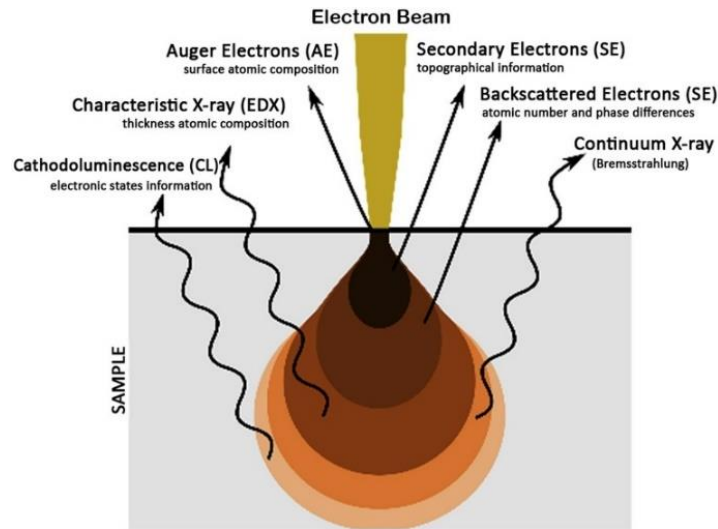


Figure 4-4 Different effects produced by elastic and inelastic interactions of primary electrons with the sample surface and near surface regions¹⁰⁹.

Important information can be gained from the Z contrast as a result of elastically backscattered electrons (BSE). BSE signal is generated from deeper layers of the sample due to the scattering through coulomb interaction at nuclei. Typically, heavier elements (higher atomic number), because of their bigger nuclei, can deflect incident electrons more strongly than the lighter elements. Thus, means that the heavy element appears brighter in comparison to the light elements. This contrast enables imaging of the microstructure of the specimen¹⁰⁸.

Depending on which information is required the SEM or BSE can be observed individually. The advantage of SEM is that there is no tedious preparation of the sample. The sample has to be conductive in order to gather sufficient information through the interaction of the sample and low energy electrons. The sensitivity of the sample to an electron beam has also to be considered, since the sample could be damaged during the analysis¹⁰⁸.

SEM images for this project were taken using a FEI Quanta 250 FEG SEM. Small amounts of the samples were attached to the sample holder with conducting carbon tape. Different accelerating voltages were used.

4.6 Electrochemical measurements

4.6.1 Linear Sweep Voltammetry (LSV)

The technique that was used is linear sweep voltammetry (LSV). The onset potential in the LSV at which the current starts to rise from zero indicates the beginning of a specific redox reaction. In the LSV the current is measured during potential scan to quantify the amount of chemical species which is undergoing a redox process. For an oxidation reaction the anodic current onset potential marks the beginning of the oxidation. Therefore, the electrode potential was scanned in a positive direction to estimate the oxidation onset potential¹¹⁰.

Electrochemical measurements were performed in the custom-made one compartment electrochemical cell using a standard three electrode configuration. The catalyst coated FTO substrate was used as working electrode, the Pt was used as the counter electrode and Ag/AgCl in 3M KCl was used as reference electrode. 0.1 M Na₂SO₄ was used as electrolyte for all measurements. After adding the electrolyte, the compartment was closed, and the headspace was purged with N₂ or Ar for 45 min before every measurement.

4.7 In-situ Techniques

Understanding the structural changes during heating could be obtained by using in-situ techniques, which are described in the following.

4.7.1 In-situ X-ray Diffraction (In-situ XRD)

In-situ XRD was used to observe the changes in XRD pattern as a function of temperature increasement. The principle of PXRD has already been explained in Section 6.1. In-situ XRD measurements were conducted on PANalytical, X'Pert Pro MPD diffractometer system, conducted with Cu-K $\alpha_{1,2}$ radiation ($\lambda = 1.54060 \text{ \AA}$, 1.54439 \AA) in Bragg Bretano Geometry with X-Celerator multichannel detector. The samples were heating with Anton Paar HTK 1200 N heating stage in air atmosphere up to $800 \text{ }^\circ\text{C}$ with a ramp rate of 5°C min^{-1} ²⁵.

4.7.2 In-situ Diffuse Reflectance Fourier Transform Infrared Spectroscopy (DRIFTS)

The changes in relative intensities of characteristic vibrational bands upon heating up to $600 \text{ }^\circ\text{C}$ and dwelling at constant temperature have been investigated with in-situ DRIFTS. In DRIFTS measurements the sample diluted in non-absorbing matrix (such as KBr) is probed with infrared energy through input mirror. The IR radiation interacts with solid samples by reflecting off their surface, causing the light to diffuse or scatter. Through the output mirror the sample scattered signal is collected and relayed to IR detector. The altered IR signal is recorded as an interferogram, which is then converted to spectrum using Fourier Transformation¹⁰³. DRIFTS measurements were performed with an IR-Tracer (Shimadzu, Japan) under air atmosphere. The samples were diluted with KBr (95:5), whereas pure KBr was used as background. The instrument was equipped with a heating stage and temperature controller. All measurements were conducted under air atmosphere²⁵.

5 Experimental Part

5.1 Material Synthesis

The catalysts for this thesis were synthesized *via* solvothermal method. The solvothermal method is based on heating both the precursor and a solvent in a closed system, allowing the temperature of the solvent to be brought near its critical point by heating while maintaining autogenous pressures¹¹¹.

5.1.1 Synthesis of Mixed-ligand MOFs xNH₂-MIL-101-Fe

A series of mixed-ligand MOFs with different NH₂-BDC to BDC ratios have been prepared by adding a certain amount of both ligands to produce samples with NH₂-BDC mol.% equal to 2, 5, 17, 50 and 80. The molar ratio of FeCl₃·6H₂O metal precursor to ligand was 2:1. BDC, NH₂-BDC and the precursor were dissolved in anhydrous DMF (20 mL) and stirred for 15 min at 300 rpm to ensure homogenization. The resulting mixture was poured into a 100 mL Teflon-lined steel autoclave and heated at 150 °C for 12 h. After cooling to room temperature, the resulting powder was washed three times with DMF and twice with methanol to remove the unreacted ligand and separated by centrifugation, before drying in vacuum at 100 °C overnight.

5.1.2 Synthesis of Single-ligand MOFs with Different Functional Groups

Single-ligand Fe-MOFs were synthesized by the same single-pot procedure, where 675mg (2.48) mmol of FeCl₃·6H₂O and 1.24 mmol of the terephthalic acid (H₂BDC), 2-aminoterephthalic acid (NH₂-BDC), 2-bromoterephthalic acid or 2-nitroterephthalic acid depending on the desired sample were homogenized in solvent. Preparation details are listed in the Table below.

Table 5-1: Preparation details of the single-ligand Fe-MOFs as well as mixed-ligand Fe-MOFs.

Samples	x mol.%-MIL-101-Fe								
	0	2	5	17	50	80	100	-	-
BDC-NH ₂ mol.%	0	2	5	17	50	80	100	-	-
BDC-Br mol.%	-	-	-	-	-	-	-	100	-
BDC-NO ₂ mol.%	-	-	-	-	-	-	-	-	100
BDC (mg)	206	202.3	196.1	171.4	103.2	41.3	0	-	-
BDC-NH ₂ (mg)	0	4.5	11.2	38.3	122.5	180.1	224	304.5	262.4
FeCl ₃ · 6H ₂ O (mg)	675	675	675	675	675	675	675	675	675
Solvent volume (mL)	20	20	20	20	20	20	20	20	20

5.1.3 Synthesis of Reference Single-ligand MOFs

5.1.3.1 MIL-53(Fe)

The previously reported synthesis method by Horcajada was used for the MIL-53-Fe synthesis⁶⁹. A mixture of FeCl₃·6H₂O and H₂BDC with a molar ratio of 1:1 was dissolved in 25 ml DMF and transferred into a Teflon-lined autoclave and heated at 150°C for 15h. After cooling down the product was washed with 150 mL methanol and 150 mL deionized water and filtered with nylon filter paper. After that it was dispersed in water and left to stir over night. Afterwards the product was filtered and dried under vacuum at 170 °C for 12 to remove trapped DMF.

5.1.3.2 Ce-UiO-66

A single ligand Ce-UiO-66 was synthesized via solvothermal method. 1,4-benzendicarboxylic acid (H₂BDC, 35.4 mg, 213 μmol) was added to a reactor. After the addition of N,N-dimethylformamide (DMF; 1.2 mL) an aqueous solution of cerium(IV) ammonium nitrate (400 μL, 0.5333 M) was added. The reaction mixture was stirred for 30 minutes at 300 rpm to ensure homogenization. The Teflon-lined steel autoclave was sealed and heated at 100 °C for 6h. The light-yellow precipitate was centrifuged in the mother liquor, which was then decanted off, before being re-dispersed and centrifuged twice in DMF (2 mL). To remove DMF from the product, the solid was washed and centrifuged with acetone (2 mL) four times. The resulting white solid was dried in air at 60 °C.

5.2 Heat-treatment of Mixed-ligand Fe-MOFs

The samples were heated in air with a constant ramp rate of 5 °C min⁻¹ to 300 °C and then held at that temperature for 3h. After thermolysis the samples were allowed to cool down to room temperature. Different temperature programs were applied for MOFs with higher amino content.

Table 5-2: Different heat-treatment parameters of the mixed-ligand MOFs.

NH ₂ -BDC mol.%	250°C 5h	300°C 1h	300°C 2h	300°C 3h
2	✓	✓	✓	✓
5	✓	✓	✓	✓
17	✓			✓
50		✓	✓	
80		✓	✓	

5.3 Photocatalytic Experiments

5.3.1 Photocatalytic Nitrogen Reduction Reaction (NRR)

Before the photocatalytic reaction the catalyst (5 mg) was heated at 100 °C on the Schlenk line for 3h in order to remove adsorbed gases including nitrogen. In following, it was left to cool down to room temperature under vacuum and then purged with Ar and evacuated interchangeably five times. 10 mL of HPLC-grade water, which was previously purged with Ar was added with a syringe needle through a septum. Photocatalytic experiments were conducted in a custom-made flow reactor under UV light irradiation by a 365 nm LED lamp. The reactor was placed in an intransparent box. The nitrogen source was provided through the bubbling of N₂. Before irradiation the solution was stirred in the dark for 30 min with N₂ bubbling to establish the equilibration of N₂ adsorption and desorption on the catalyst surface. The N₂ was pumped in the reactor at a constant rate of 80 ml L⁻¹ throughout the experiment. Three different control experiments were performed to verify the results. The solvent was high-purity water without any sacrificial agent.

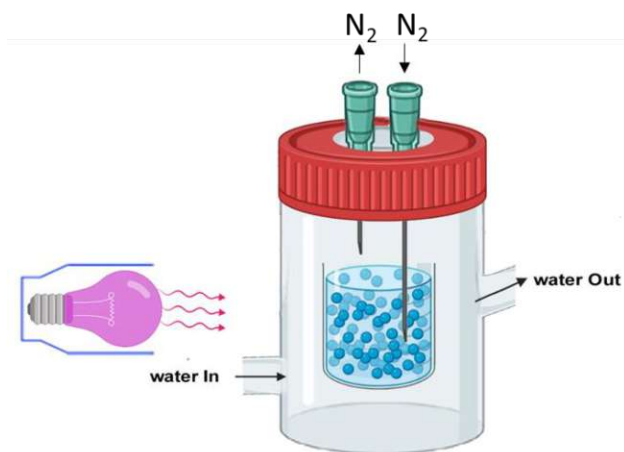


Figure 5-1 Experimental set-up for photocatalytic nitrogen reduction reaction.

5.3.2 Spectrophotometric Ammonium Detection

The NH₃/NH₄⁺ concentration was analyzed by Nessler's reagent method. The suspension was filtered through 0.22 μm PTFE filter. Then 1 mL of Nessler's reagent [K₂(HgI₄)] was added to the reaction solution followed by 1 mL of 1M NaOH. Then the mixture was left to stand for 20 minutes

for full-color processing. The concentration was determined using a UV-Vis spectrometer at 420 nm wavelength. The production rate was determined using the following equation:

$$r_{NH_4^+} = \frac{n_{NH_4^+}}{m_{cat} \cdot t} [r_{NH_4^+}] = \frac{\mu mol}{g \cdot h} \quad 5-1$$

5.4 Electrochemical Experiments

The ink for the electrode coating was prepared by dispersing the photocatalyst (5 mg) in the mixture of 0.5 ml ethanol and 10 μ l 5 wt.% Nafion solution (Sigma Aldrich 5wt.% in aliphatic alcohols and water). Subsequently the mixture was sonicated in an ultrasound bath for 60 min.

In the following 100 μ l of the above suspension was coated on fluorine-doped tin oxide (FTO) substrate. After the ethanol was evaporated the suspension coated FTO glass was dried at room temperature for 12 h under vacuum.

6 Results and Discussion

6.1 Influence of Ligand Tuning on Properties of Fe-based MOFs

One of the goals of this thesis was to study the influence of ligands with different functional groups on the MOFs structural and physiochemical properties as well as catalytic performance. In the following properties and performance of mixed-ligand MOFs $x\text{NH}_2\text{-MIL}$ with different ratios of 2-aminoterephthalic acid to terephthalic, as well as single-ligand Fe-MOFs with differently substituted BDC ligand will be presented and discussed.

6.1.1 Single-ligand and Mixed-ligand Fe-MOFs with Different $\text{NH}_2\text{-BDC}$ Content

6.1.1.1 The Crystalline Structure of Single-ligand Fe-MOFs

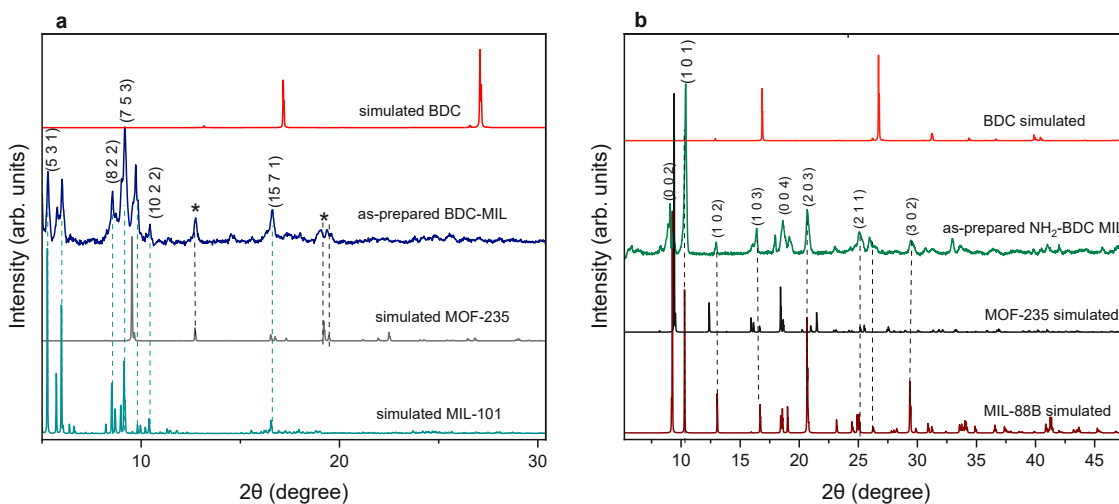


Figure 6-1 PXRD patterns of as-prepared single-ligand Fe-MOFs compared to the simulated patterns: a) BDC-MIL (MOF-235 peak is marked with *); b) $\text{NH}_2\text{-BDC-MIL}$.

The diffraction patterns of single-ligand BDC and $\text{NH}_2\text{-BDC MIL}$ do not resemble each other, although they were obtained using the same synthesis procedure. I compared these patterns with simulated patterns for defect-free crystals obtained from crystallographic information files using VESTA software. None of the peaks fits the simulated pattern of the BDC ligand, claiming the incorporation of the ligand in the framework of both single-ligand MOFs.

Furthermore, both patterns show significant peak broadening due to the crystallite size decreases to nanoscale dimensions¹¹².

The single-ligand NH₂-BDC MOF adopts the crystalline structure of MIL-88B phase. The PXRD pattern of the pristine NH₂-BDC MIL has been compared with topologically identical MOF-235 (Fe) to exclude the possibility of its formation. The representative peaks with corresponding Miller indices align well with the simulated pattern, and there is no indication of a secondary phase.

In single-ligand BDC MIL, the low angle feature at approximately 9.5° closely resembles peaks found in MOF-101(Fe), as shown in *Figure 6.1a*.

The additional peak at 2θ = 12.75°, corresponds to MOF-235 phase, which is another terephthalate-based MOF reportedly misidentified as MIL-101^{113, 114, 115, 116}.

Figure 6-2 provides enlarged view of the PXRD diffraction patterns, focusing on the representative diffraction angle range.

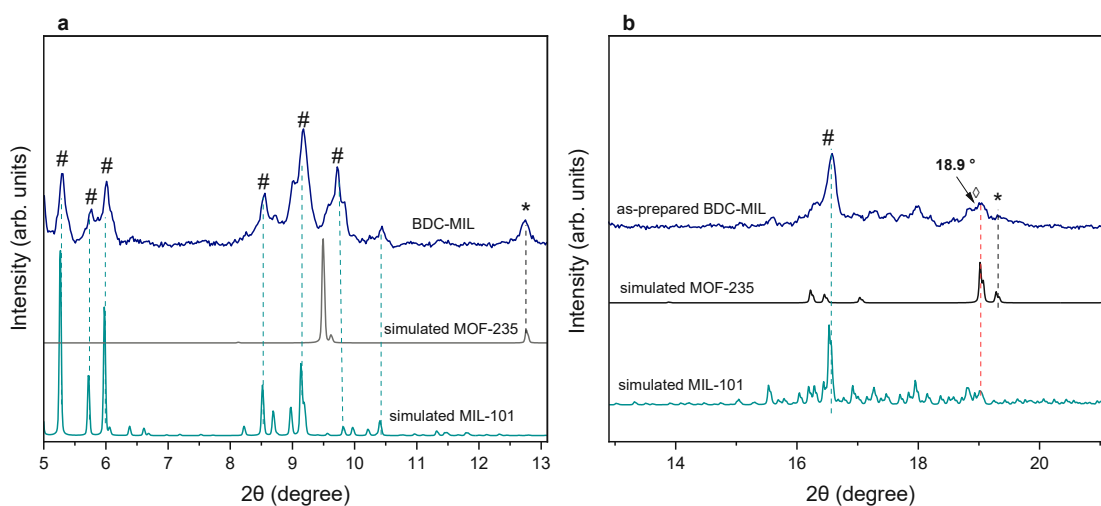


Figure 6-2 Enlarged view of the PXRD patterns focused on the characteristic diffraction peaks: a) 5-13 2θ range; b) 15-25 2θ range (MIL-101 peaks marked with # and MOF-235 peaks marked with *, unassigned peak is marked with ◊).

Table 6-1 The main Bragg reflections assigned to the corresponding phases and facets (obtained using RIETAN FP in Vesta).

2θ (°)	Phase	h k l	d _{hkl} (Å)
5.2	MIL-101	5 1 1	17.1
5.6	MIL-101	4 4 0	15.7
5.8	MIL-101	5 3 1	15.1
8.5	MIL-101	8 2 2	10.1
9.1	MIL-101	7 5 3	9.7
9.8	MIL-101	9 3 3	8.9
10.3	MIL-101	10 2 2	8.5
12.7	MOF-235	1 0 2	7.1
16.5	MIL-101	14 8 4	5.3

The obtained product does not exhibit a single prominent peak at 9.4° , which corresponds to the (1 0 1) facet of MOF-235, but instead shows several additional peaks in the $5 - 10^\circ$ range, which are associated with MIL-101^{117, 118}

Previously reported syntheses of MOF-235 have revealed significant variations in surface areas, suggesting the potential coexistence of both MOFs within the sample^{119, 118}.

As it will be discussed later, MOF-235 is considered an intermediate in the self-assembly of MIL-101¹²⁰. Therefore, it is highly possible that it is incorporated into the crystal structure of the MIL-101, suggesting it's incomplete reassembly.

To further validate this hypothesis additional characterization analyses may be necessary, such as transmission electron microscopy (TEM), to visualize the structure at a finer scale and identify the locations of MOF-235 incorporation.

A more detailed discussion on the preferential phase formation of different Fe-terephthalate MOFs will be annexed at the end of this section after summarizing the data from XRD and FTIR.

6.1.1.2 The Crystalline Structure of Mixed-ligand Fe-MOFs

To elucidate the effect of introducing the NH₂-BDC, the PXRD patterns of mixed-ligand Fe-MOFs with different molar ratios will be analyzed.

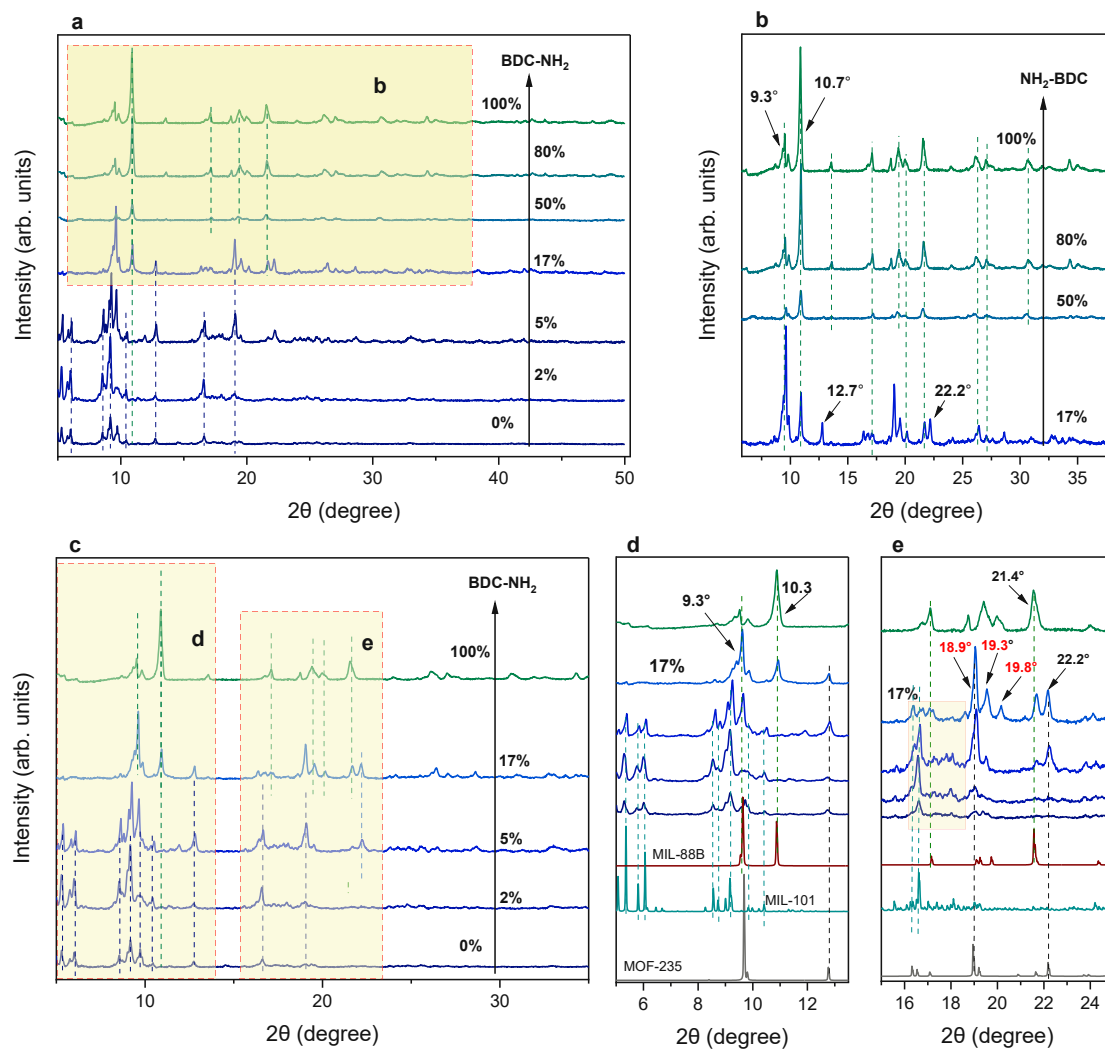


Figure 6-3 PXRD patterns of as-prepared BDC-MIL, NH₂-MIL and mixed-ligand xNH₂-MIL Fe-MOFs with different NH₂-BDC content: a) all samples; b) 17 mol.% and higher NH₂-BDC content; c) – e) 17 mol.% and lower NH₂-BDC content with simulated spectra as reference.

The PXRD patterns of as-prepared samples prepared by the same synthesis procedure reveal the formation of different phases as a function of NH₂-BDC content. The single-ligand BDC-MIL and mixed-ligand samples with a low percentage of NH₂-BDC ligand (2 and 5%) exhibit the same Bragg reflections, with a slight variation in peak relative intensities.

In the sample with 17 mol.% NH₂-BDC, different PXRD patterns are observed. The pattern corresponding to the lower amino-content ratio overlaps with the pattern of NH₂-BDC MIL, which has been assigned as the MIL-88B phase.

However, the 17 mol.% sample does not exhibit characteristic peaks of the MIL-101 phase in the $2\theta \sim 5^\circ$ region. The planes corresponding to the main peaks in this region are depicted in the Figure below and represent the MIL-101 pentagonal and hexagonal windows.

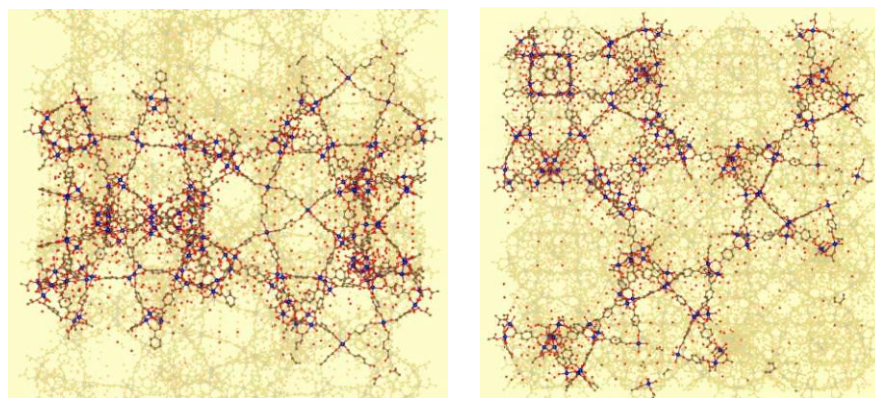


Figure 6-4 Characteristic crystallographic planes of MIL-101: a) (5 1 1) plane; b) (4 4 0). Exported using VESTA.

The absence of peaks corresponding to these planes in the 17 mol.% sample, unlike the samples with lower NH₂-BDC content, indicates incomplete crystalline growth of the MIL-101 phase. Additionally, the diffraction angle region between 16 and 18° (highlighted in yellow shade in Fig.6.3d) matches the simulated pattern of MIL-101 in the 17 mol.% sample, but the peaks exhibit very low intensity. This is expected due to the presence of different phases in the sample, potentially hindering the crystalline growth of MIL-101 and resulting in incomplete and defective formation of this phase.

In the 17 mol.% NH₂-BDC sample, the peaks corresponding to the MIL-88B phase are notably prominent. Of specific interest is the region around 9°, where all three Fe-based MOFs exhibit diffraction peaks. However, only MIL-101 displays multiple peaks in this region, as observed in samples with NH₂-BDC content lower than 17 mol.%. Therefore, the 9.3° peak in the 17 mol.% NH₂-BDC sample is characteristic of the MIL-88B phase.

Increasing the amino-ligand content is observed to have an inversely proportional effect on the peaks at 9.3° and 10.7° (Fig. 6.3b). More precisely, the peak intensity at 9.3° decreases as the amino-ligand content rises, while the peak intensity at 10.7° increases.

This trend suggests an opposing influence of NH_2 -group on the crystallization of distinct crystallographic planes within the Fe-MOFs. In the enlarged spectra (*Fig. 6.3d-e*), the trend in the growth of different planes can be followed.

The peaks at $2\theta = 12.7$ and 22° , corresponding to the MOF-235 phase, exhibit higher relative intensities with increasing amino-content up to 5 mol.%. These peaks are also present in the 17 mol.% sample, although their intensity is reduced compared to the main planes of the MIL-88B phase. As previously mentioned, MOF-235 acts as an intermediate during the assembly of MIL-101. The specific growth of (1 0 2) and (2 1 1) planes promoted by the NH_2 -group will be discussed in Section 6.1.2.3.

In the region between $2\theta = 18 - 20^\circ$, it is difficult to distinguish between different phases due to the similarities between the polymorphs, which have same structural motifs and differ just in the coordination environment leading to structural variation with minor differences^{121, 122, 121}. Due to the similar 2θ values of the Bragg reflections in this region, which also breath, the 18.9° , 19.3° and 19.8° peak cannot be with certainty attributed to any specific Fe-terephthalate phase This challenge is evident in the PXRD analysis of single-ligand BDC MIL, where the $2\theta = 18.9^\circ$ peak remains unclassified.

The peak at $2\theta = 22.2^\circ$, observed in the 5 and 17 mol.% samples, can be exclusively attributed to the MOF-235 phase. The irregular shapes of peaks in the region $2\theta = 16 - 19^\circ$, including the unassigned peak at 19.8° in 17 mol.% NH_2 -BDC sample, are a result of non-uniformity in the crystal lattice due to the coexistence of three phases. This consequently leads to the variation in interplanar spacings and observation of the peak at different angle than expected for the pure-phase sample¹¹².

The samples with 50, 80 and 100% of NH_2 -ligand correspond completely to the crystalline structure of the MIL-88B phase emerged in 17 mol.% sample.

However, the 50 and 80 mol.% samples show a much lower degree of crystallinity than the NH_2 -BDC MIL. Hence, there is an amorphization with decreasing of NH_2 -BDC content from 100 to 50 mol.% (*Fig.6.3b*).

A high content of amino ligand clearly promotes the formation of MIL-88B phase. However, in the case of 50 and 80 mol.% of NH₂-BDC, the regularity and connectivity of the crystal lattice may be disrupted. This deviation from desired interaction can lead to formation of disordered or amorphous regions¹¹².

In summary, the PXRD patterns confirm the crystalline nature of both single-ligand Fe-MOFs and mixed-ligand Fe-MOF samples. The formation of different crystalline phases is observed depending on the amino ligand content. Single-ligand NH₂-BDC MIL results in the formation of the MIL-88B phase, a trend also seen in samples with higher NH₂-BDC ratios (50 and 80%). Samples with lower ratios do not exhibit a pure MIL-101 crystalline phase. Instead, the PXRD pattern of single-ligand MIL shows two low-intensity peaks corresponding to MOF-235.

The relative intensity of reflections from different facets changes with NH₂-BDC content, indicating the significance of specific interactions during synthesis, despite using similar parameters. Single-ligand BDC-MIL samples with 2 and 5 mol.% NH₂-BDC exhibit the main diffraction peaks of MIL-101, with minor presence of the MOF-235 phase. The incomplete reassembly of MOF-235 intermediate clusters into MIL-101, a phenomenon previously reported in Al-analogues, will be discussed in the following section.

Moreover, mixed-ligand samples with 17 mol.% NH₂-BDC ligand represent a turning point, where major crystallographic planes align with the MIL-88B phase, with minor alignment in samples containing lower amino-ligand ratios.

Lastly, samples containing 50 and 80 mol.% of the amino-ligand show lower crystallinity compared to single-ligand NH₂-BDC MIL. Although NH₂-BDC can promote MIL-88B formation, disparities in specific interactions can lead to inconsistent synthesis conditions and asymmetric coordination environments. These factors limit crystal growth, as observed in the PXRD pattern. To gain deeper insights into the interactions influencing crystal growth and to understand the underlying mechanisms, computational simulations should be employed.

6.1.1.3 FTIR Spectroscopy of Single- and Mixed-ligand Fe-MOFs

6.1.1.3.1 FTIR Analysis of Single-ligand MOFs

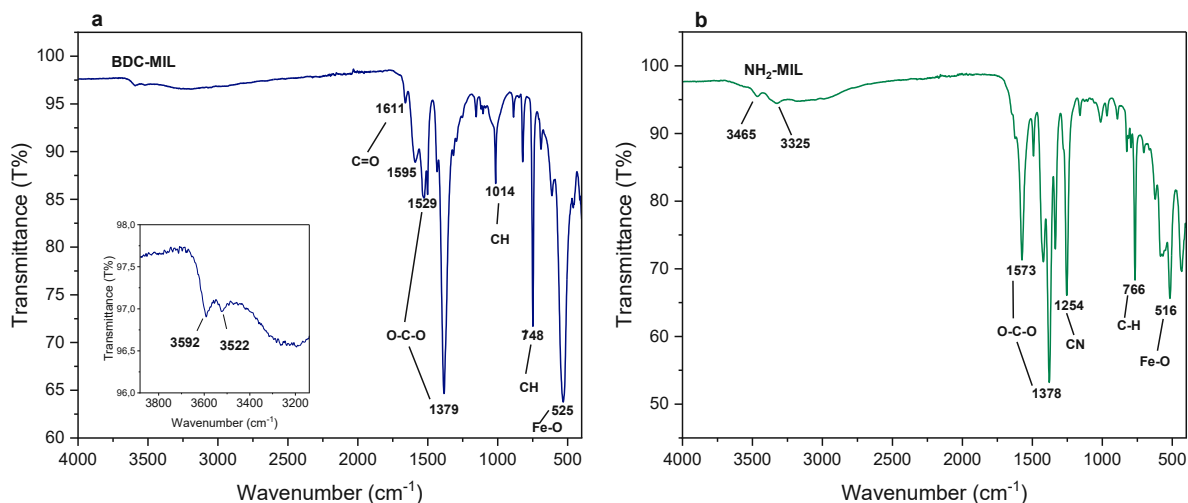


Figure 6-5 FTIR spectra of single-ligand MOFs: a) BDC MIL; b) NH₂-BDC MIL.

In Fig. 6-6 the FTIR spectra of two single-ligand MOFs are shown. The presence of the NH₂-BDC in the NH₂-MIL can be confirmed from the asymmetric and symmetric NH₂-stretch bands at 3465 and 3325 cm⁻¹, respectively¹¹³.

The OH range of BDC-MIL was magnified to see the exact peak positions. There are two distinguishable OH stretching vibrations. The one at a lower frequency (3522 cm⁻¹) can be assigned to the H-bonded OH group and the second one at 3592 cm⁻¹ can be attributed to free OH group of the iron-oxo cluster. The OH stretching vibration cannot be observed in the single-ligand NH₂-BDC MOF. This means that the H-bonds between the amine group and the OH groups are strong, which disables the hydroxy group stretching¹¹⁷.

The two peaks at 1592 and 1520 cm⁻¹ in the BDC-MIL are symmetric vibrations of carboxyl group^{79, 80}.

In the NH₂-BDC MOF the asymmetric O-C-O vibration modes can be observed at 1573 and 1500 cm⁻¹. The peak corresponding to the asymmetric O-C-O mode is red-shifted to 1573 cm⁻¹, in comparison to the same vibration at 1595 cm⁻¹ in single BDC-MOF. The shift can be attributed to the presence of NH₂-group and the resonance effect caused by its electron-donating properties⁸¹.

The asymmetric stretching in the NH_2 -ligand MOF has higher relative intensity than the same vibration in BDC-ligand MOF. The observed decrease in the relative intensity can be attributed to the presence of another phase with asymmetric carboxylic vibrational mode at 1529 cm^{-1} , which is consistent with the results obtained from the PXRD analysis.

Apart from the stretching vibrations of NH_2 there is also the CN vibration characteristic for the presence of the aromatic amine group in the NH_2 -containing MOF at 1254 cm^{-1} ¹²³.

The CN vibration in the free NH_2 -BDC is at 1235 cm^{-1} ³². The blue-shift indicates the incorporation of the ligand in the framework as the interaction gets stronger.

Another difference is the presence of carbonyl stretch corresponding to free carboxylic acid at 1661 cm^{-1} in the BDC single-ligand MOF which is not present in amino-substituted ligand MOF. Notably, the samples underwent washing after synthesis to eliminate unreacted BDC ligands. This suggests the presence of singly coordinated BDC ligands within the MOF framework, indicating a low degree of crystallization characterized by incomplete ligand coordination. This observation aligns with the results obtained from PXRD analysis, which identified the presence of a secondary phase characterized by a lower degree of crystallinity.

In the second region, the peaks at 1014 cm^{-1} , 748 cm^{-1} ($\gamma_{(\text{C-H})}$), 1159 cm^{-1} ($\sigma_{(\text{C-H})}$) and 821 cm^{-1} are attributed to the in-plane and out-plane bending of aromatic C-H bond⁸². The band at 1014 cm^{-1} appears due to aromatic C-H vibration mode and is quite prominent in the BDC-MIL, while it has low intensity in the NH_2 -MIL. This reduction in intensity can be attributed to the transfer of energy from the stretching vibrations of the C-H bond to the surrounding molecular vibrations involved in the hydrogen bond network^{79, 80}.

The apparent peak at 748 cm^{-1} of BDC-MIL is red-shifted in comparison to the same vibration in NH_2 -MIL at 766 cm^{-1} . This is obviously due to the presence of amino-group in the ligand, which restricts the in-plane bending because of more H-bonding. The same argument can explain the decrease in vibration at 1014 cm^{-1} , where the NH_2 -group reduces the degree of freedom of hydrogen atoms in the benzene ring.

Finally, the apparent band at 525 cm^{-1} in the BDC-MIL is associated with the Fe-O vibration. In the NH_2 -MIL the bands associated with the Fe-O vibration at 516 cm^{-1} are accompanied with shoulder

at 583 cm^{-1} , indicating the presence of different Fe-O coordination environments and variations in the Fe-O bond distances. The asymmetric coordination can be attributed to the hydrogen bonding of NH_2 group with the O atom, which can reduce the effective charge of the one of four oxygens as previously reported on MIL-125 (Ti)²⁵

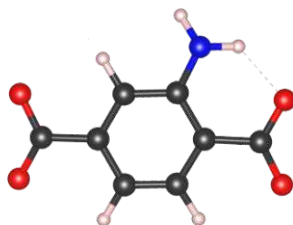


Figure 6-6 Hydrogen bonding between the NH_2 -group and oxygen of the carboxyl group.

6.1.1.4 FTIR Analysis of Mixed-ligand MOFs

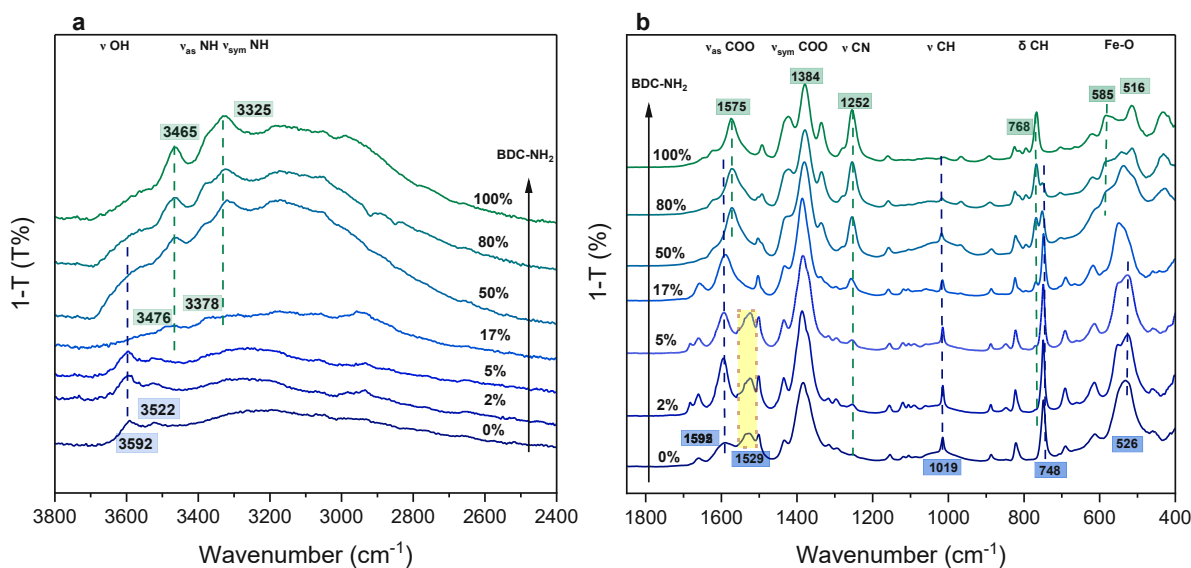


Figure 6-7 FTIR spectra of mixed-ligand MOFs: a) Enlarged high frequency range of vibrational spectra b) Enlarged vibrational spectra in lower frequency range. The peaks colored with blue shade represent characteristic peaks of MIL-101-Fe; the peaks marked with green color representing the NH_2 -MIL-88B-Fe phase.

The OH-band corresponding to the coordination of the SBU can be observed at 3592 cm^{-1} . As already discussed in the interpretation of single-ligand MOFs, this band is prominent in single-ligand and mixed-ligand samples featuring lower amino content. However, at NH_2 -BDC content of 17 mol.% and higher, the band exhibits increased broadening. This broadening can be attributed to the formation of hydrogen bonds between NH_2 -group and oxygen atoms originating from the SBU¹²⁴.

Apart from that, the simultaneous increase in aromatic NH bands (3465 and 3325 cm^{-1})¹¹³ and carbonyl band (1252 cm^{-1}) can be observed as the content of $\text{NH}_2\text{-BDC}$ increases, indicating the incorporation of the ligand in the framework.

More information on the characteristic peaks can be found in the region between 1800 and 400 cm^{-1} (Fig 6-8b). The peak corresponding to symmetric O-C-O stretching at 1595 cm^{-1} becomes more prominent with increasing $\text{NH}_2\text{-BDC}$ ratio and it is gradually shifted to the lower frequency. As already mentioned, the resonance effect due to the delocalized electrons causes different polarization which leads to this shift. Increasing amino content leads to the gradual redshift of this peak, meaning that the coordination bond strength gradually weakens. Additionally, there is another peak that can be assigned to the asymmetric C-O-C vibrational mode which can be found in the single-ligand BDC-MIL and mixed-ligand MOFs with 2 and 5% $\text{NH}_2\text{-BDC}$. To observe more clearly the change in band positions this part of the spectrum has been magnified.

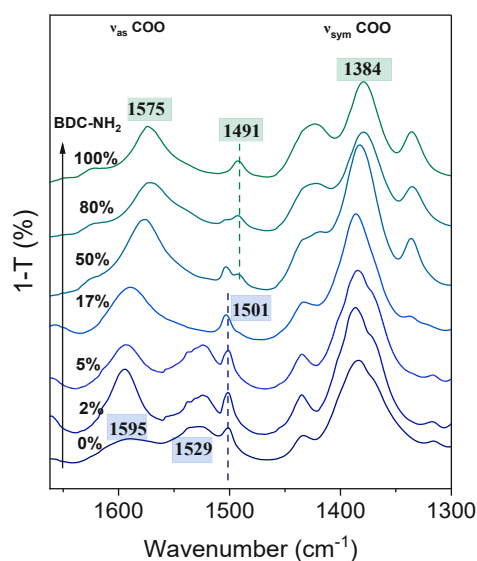


Figure 6-8 Enlarged vibrational spectra in range between 1700 and 1300 cm^{-1} .

Two distinguishable bands at 1529 and 1592 cm^{-1} are present in samples up to 17 mol.% $\text{NH}_2\text{-BDC}$, which is consistent with the observed secondary phase in diffraction patterns of these samples.

Furthermore, The C-C stretching vibration mode shows characteristic peaks at 1501 cm^{-1} and 1491 cm^{-1} corresponding to MIL-101-Fe and $\text{NH}_2\text{-MIL-88B}$, respectively¹²³.

The stretching at 1501 cm^{-1} corresponding to the C-C stretching vibration in the benzene ring has the same position in the 17% NH_2 -MIL like the samples with lower NH_2 -BDC content and single BDC MIL, whereas the samples with 50, and 80 mol.% are superimposed from the BDC-MIL and NH_2 -MIL, indicating that this functionality is solely affected by the NH_2 -content without contribution different Fe-terephthalate phases.

In summary, FTIR analysis complements PXRD results, providing insights into the influence of NH_2 -BDC ligand interactions and bond strengths. In the presence of the amino ligand, the OH band associated with terminal coordination to the metal center becomes less prominent due to hydrogen bonding with the NH_2 -group of the ligand. Additionally, the asymmetric stretching of the carboxyl group is significantly affected by the presence of the electron-donating amino-ligand, resulting in a red-shift of this band. The electron-donating properties of the NH_2 -group also impact the Fe-O coordination by weakening the effective charge on the O-atom, a phenomenon previously observed in MIL-125(Ti)²⁵.

6.1.1.5 Interpretation of Irregular Synthesis of Fe-terephthalate MOFs

In order to understand irregular synthesis outcomes under same time and temperature conditions, the structure of the different phases found in PXRD measurements has to be studied. MIL-101 and MIL-88B are constructed from a trinuclear oxo-centered SBU linked with terephthalic acid ligands, with the formula $[\text{Fe}_3\text{O}(\text{BDC})_3(\text{OH}_2)_2\text{X}]$, where X is a monoanion typically OH^- or Cl^- . They differ in the topology and pore structure⁷⁴. MOF-235 is topologically identical to MIL-88B(Fe), but contains a pore-located $[\text{FeCl}_4]^-$ counterion rather than a cluster bound monoanion, with the formula $[\text{Fe}_3\text{O}(\text{BDC})_3(\text{DMF})_3][\text{FeCl}_4]$ ¹¹⁷.

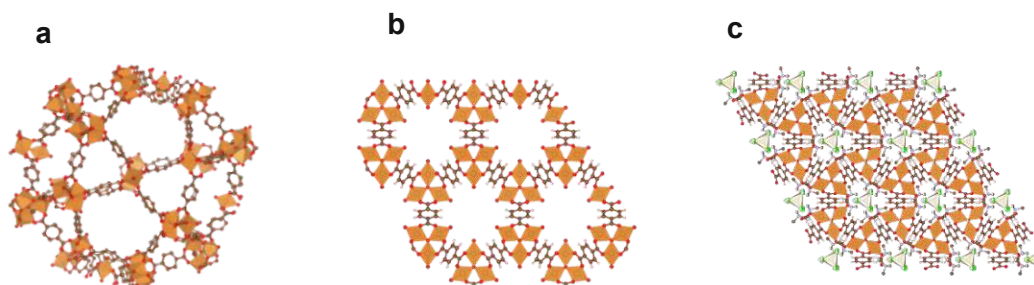


Figure 6-9 Different Fe-terephthalate phases: a) MIL-101-Fe; b) MIL-88B-Fe; c) MOF-235-Fe. Exported using VESTA Software.

The polymorphism of Fe-based MOFs has already been reported by Taylor-Pashow *et al.* They compared the formation of different Cr/Fe - mixed-metal terephthalate MOFs and found that the incorporation of iron in the framework results in the formation of different phases. Taylor-Pashow *et al.* were the first to synthesize the MIL-101(Fe) pure phase using an equimolar solution of FeCl_3 and BDC in DMF at 150 °C with microwave heating. They have also attempted to synthesize the amino-functionalized analogue. However, they successfully incorporated amino substituted MIL-101(Fe) up to 17.5 mol.% of NH_2 -BDC. The particles with higher molar ratios adopted the MIL-88B structure¹²⁵. This is in accordance with obtained results in my work.

Later it was stated that MIL-101 is the kinetic product, preferentially formed in one-pot shorter time synthesis, while longer reaction time at the same temperature promoted the synthesis of thermodynamically stable MIL-88B phase^{73, 75, 126}.

MOF growth proceeds through a dissociative mechanism, where ligand substitution is a repeated process of the growth. In this process, electrostatic interactions, along with other forces such as hydrogen bonding and van der Waals forces, influence the arrangement of metal clusters and ligands. Thus, the interplay of various forces determines the final structure¹²⁷.

The polar amino groups of the NH₂-BDC ligand can interact with solvent molecules, which are primarily van der Waals interactions and involve dipole-dipole interactions and H-bonding between the H-acceptor (O atom in the carbonyl group of DMF) and the NH₂-group (which acts as a H-donor). Due to these specific interactions the transport of the ligand to the metal core is likely restricted and the system is kinetically limited in growth.

MOFs were prepared by adding the metal precursor to the ligands, without any preferential bond forming between H₂BDC and FeCl₃ precursor, which could be exchanged by adding the NH₂-BDC. Consequently, the crystal growth is governed by the interactions of reactants with the solvent^{128, 129}.

The very early study by Bauer *et al.* investigated the influence of different preparation conditions on three *isorecticular* MOFs based on comparable trivalent metal ions and BDC bidentate linker one of which was MIL-101(Fe). They have synthesized NH₂-MIL-101 (Fe) from a 2:1 molar ratio of ferric chloride hexahydrate (FeCl₃·6H₂O) with 2-aminoterephthalic acid (NH₂-BDC), by dissolving it in DMF, stating that the increase in metal precursor favors the formation of MIL-101 phase⁹¹.

However, the synthesis of MIL-101-Fe is more sensitive to the synthesis parameters than other MIL-101 isomorphs. MIL-101 can be easily converted to another type of MOF. This means that a mixture of different phases can be obtained and the studies on synthesis parameters have been reported, where the possibility of different polymorphic iron(III) terephthalates (MIL-101-NH₂, MIL-88B-NH₂, MIL-53-NH₂ and MIL-68-NH₂) as a function of time, temperature, concentration and reaction media, has to be considered^{91, 121, 130}.

PXRD analysis confirmed the presence of the secondary phase MOF-235 in samples with lower amino ligand content. The absence of diffraction peaks corresponding to MOF-235 in single-ligand NH₂-BDC MOF, as well as in samples containing 50 and 80 mol.% of the amino ligand, suggests

that the formation of MOF-235 is hindered by an increased concentration of $\text{NH}_2\text{-BDC}$ ligand. The exact reasons for this inhibition require further literature research.

Studies by Goesten *et al.* on isomorphous MOF-235(Al) and MIL-101(Al) phases have indicated the coexistence of both MOF-235 and MIL-101 in the same system. This behavior is consistent with the crystallization of MOF-235 occurring in the intermediate temperature regime. When the temperature is raised sufficiently, MOF-235 clusters can undergo further assembly, leading to the formation of the MIL-101 phase^{131, 120, 132}.

Researchers monitored temporal changes during crystallization using small angle X-ray spectroscopy (SAXS), confirming the formation of MOF-235 prior to MIL-101. By quenching the synthesis, they successfully isolated MOF-235¹³³. Following studies on Al-terephthalate MOFs, it is plausible that the fragments of MOF-235 phase in my synthesis conditions were unable to reassemble into the MIL-101 phase.

The mentioned studies highlighted the stabilizing role of DMF in the formation of MIL-101. DMF acts as a molecular promotor due to the formation of H-Cl-DMF complex, a crucial factor confirmed through DFT studies.¹³³ This complex is essential as it provides the hydroxide ligands necessary for facilitating ligand exchange and forming $[\text{Fe}_3\text{O}(\text{BDC})_3(\text{OH})_2\text{X}]$ cluster, as illustrated in the figure below.

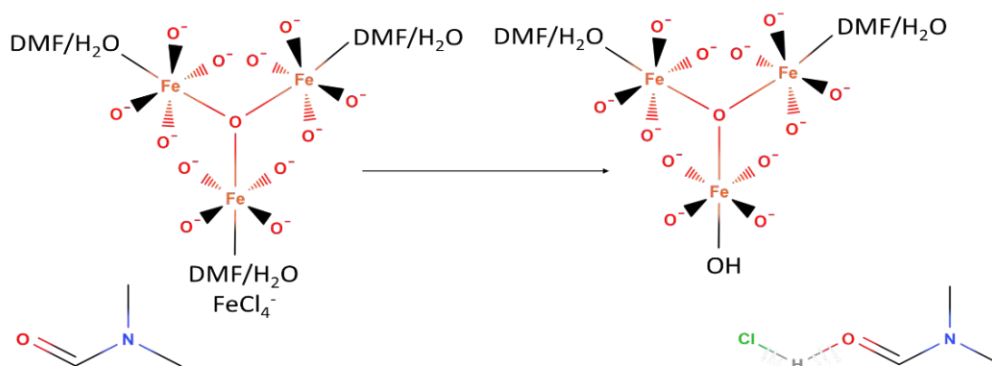


Figure 6-10 Promoting effect of DMF in the formation of $\mu_3\text{-O}$ -centered SBU that builds MIL-101 and MIL-88B Fe-MOFs. In accordance with¹³³.

Additionally, these studies confirmed that the reassembly of MOF-235 to MIL-101 is rate-determining step in aprotic solvents like DMF¹³³.

Let's examine the specific crystallographic planes associated with the 12.7° and 22.2° peaks in my samples.

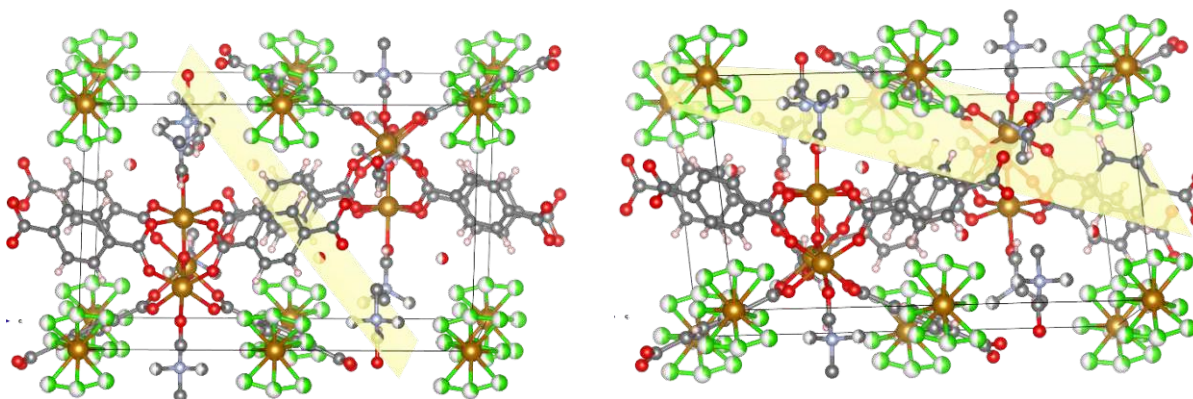


Figure 6-11 Crystallographic planes (1 0 2) and (2 1 1) of MOF-235 (BDC ligand) corresponding to the $2\theta = 12.7^\circ$ and 22.2° diffraction peaks.

The (1 0 2) plane is perpendicular to the planar plane of terephthalic acid and intersects the C-atoms of the benzene ring, in which NH_2 is located in presence of an amino-containing ligand. This plane also passes through one of three terminal DMF molecules in the SBU of MOF-235. Similarly, the (2 1 1) plane passes through the positions of terminal DMF molecule and NH_2 -group. Hence, within this crystallographic plane, DMF engages in the van der Waals interactions with the NH_2 -group. These interactions are notably abundant in this plane, making the lattice fragment of MOF-235 particularly stable. As a result, it would demand a substantial amount of energy to disassemble this structure fragment and make them available for assembly into MIL-101 phase.

These findings explain why the peak at 12.7°, indicating the presence of MOF-235, is more prominent in samples with 2 and 5 mol.% of NH_2 -BDC ligand.

However, the presence of the MIL-88B phase at high NH_2 -BDC ligand ratios, such as 50, 80, and 100 mol.%, contradicts this explanation, as no peaks corresponding to the MOF-235 phase were observed.

The key distinction between MOF-235 and MIL-88B lies in how the charge-balancing anions are situated: in MOF-235, they reside within the pores, while in MIL-88B and MIL-101, the OH^- or Cl^- coordinates directly with the $\text{Fe}-\mu_3$ -oxo-cluster. So how are the available hydroxide or chloride anions provided and why is the exchange of aqua or DMF terminal group in the case of NH_2 -MIL formation energetically favorable?

The weak base character of the NH_2 -group might increase the concentration of hydroxide ions, which are stronger nucleophiles compared to Cl^- , aqua and DMF ligands in polar aprotic solvent¹³⁴. Consequently, the exchange of Cl^- by OH^- in the coordination sphere of Fe^{3+} becomes energetically more favorable, leading to the formation of $[\text{Fe}_3\text{O}(\text{BDC})_3(\text{OH}_2)_2\text{X}]$.

Another factor contributing to the absence of MOF-235 SBU as an intermediate could be the reduced availability of DMF, which is essential for the formation of $[\text{Fe}_3\text{O}(\text{BDC})_3(\text{DMF})_3][\text{FeCl}_4]$ cluster in MOF-235. This reduction occurs due to interactions with the NH_2 -group of the ligand, diminishing its capacity to occupy the coordination site.

In summary, the polar amino groups of NH_2 -BDC interact with solvent molecules, influencing ligand transport and the growth kinetics of amino-containing MOFs. This interaction results in the formation of two distinct Fe-terephthalate phases: MIL-101 as the kinetic product in samples with low NH_2 -BDC content, and MIL-88B, considered the thermodynamic product in samples with high amino ligand content.

In previous studies, the formation of diverse phases in Fe^{3+} terephthalate frameworks have been documented. DMF plays a crucial role in stabilizing MIL-101 by forming an essential H-Cl-DMF complex, facilitating ligand exchange necessary for the creation of the $[\text{Fe}_3\text{O}(\text{BDC})_3(\text{OH}_2)_2\text{X}]$ cluster. . Despite the use of DMF as a solvent, PXRD analysis identified MOF-235 in single-ligand BDC and low NH_2 -BDC samples. The presence of diffraction peaks corresponding to specific crystallographic planes of MOF-235, such as (1 0 2) and (2 1 1), indicates strong van der Waals interactions between DMF and the NH_2 -group in MOF-235. These interactions explain the stability of MOF-235 and the prominent peaks observed at 12.7° in samples with 2, 5, and 17 mol.% NH_2 -BDC content.

The presence of MIL-88B at high NH_2 -BDC ratios suggests complex interplay between hydroxide, chloride, and DMF coordination. DMF availability for the formation of $[\text{Fe}_3\text{O}(\text{BDC})_3(\text{DMF})_3][\text{FeCl}_4]$ cluster diminishes, due to NH_2 -group interactions, influencing coordination dynamics. Moreover, the weak base character of NH_2 group provides necessary hydroxide ions for the formation of MIL-88B cluster.

In conclusion, it is likely that MIL-88B formation does not proceed through the MOF-235 intermediate. Further computational simulations could provide better insight into interactions during MOFs crystal growth. Combining molecular dynamics, which models growth dynamics and specific interactions, with DFT calculations could predict energetically stable structures during MOFs formations.

6.1.1.6 UV-Vis Diffuse Reflectance Spectra of Single- and Mixed-ligand Fe-MOFs

To study the optoelectronic properties of the as-prepared samples, diffuse reflectance spectra were recorded. The DRS of a semiconductor can be used to construct the Tauc-plot, from which the band gap can be determined. The absorption coefficient of the powder samples can be calculated from the reflectance spectra with the Kubelka-Munk equation^{76, 135}.

$$F(R_{\infty}) = \frac{(1-R_{\infty})^2}{2R_{\infty}} \propto \alpha(E) \quad 6-1$$

where R_{∞} is the diffuse reflectance and F is a function proportional to the absorption coefficient and can be used in a good approximation to construct the Tauc-plot. The bandgap was determined by extending the linear portion of the Tauc-plot to the abscissa.

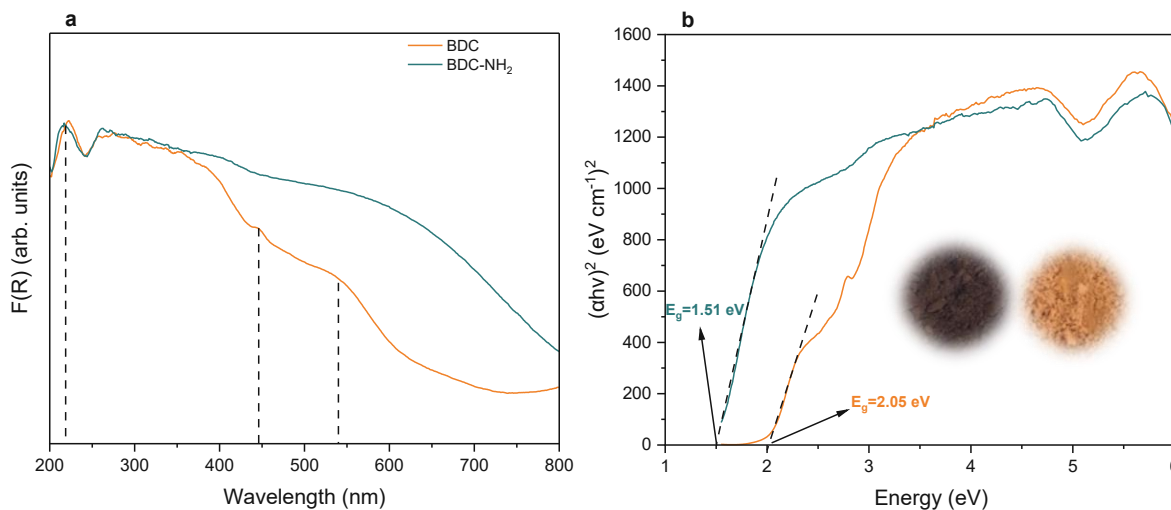


Figure 6-12 Optical characterization of as-prepared single-ligand MOFs: a) UV-Vis diffuse reflectance spectra; b) Tauc plots of the catalyst.

UV-Vis DRS spectra of MIL-101-Fe (Fig 6-3a) show that the sample exhibits high absorption in the UV range, which can be attributed to $\pi-\pi^*$ transitions in the terephthalic acid ligands, but also

absorbs in the visible range due to excitations in the Fe-oxo cluster. A peak centered at 445 nm can be ascribed to the direct transition from the O 2p orbitals to empty Fe(III) orbitals ($O^{2-}_{2p} \rightarrow Fe^{3+}_{3d}$). A wide range of absorption with the peak center at 545 nm can be attributed to spin-allowed d-d transition ${}^6A_{1g} \Rightarrow {}^4A_{1g} + {}^4E_g(G)$ in Fe(III)^{136, 137}.

Figure 6-3b displays Tauc plots of the two single-ligand MOFs with the assumption of direct band gap. The optical band gap energies were determined as 2.05 and 1.51 eV for MIL- and NH₂-MIL, respectively. The narrowing of the band gap is in accordance with sample colors (*Insert in Fig. 6-3b*).

The obtained band gap values are in accordance with the literature which characterizes the iron terephthalate-based MOFs as semiconducting MOFs^{138, 139, 140}.

The band gap values are highly relevant, since they reveal at which wavelength range the catalyst can absorb. The band gap value of 2.05 eV for BDC-ligand MOF means it can absorb wavelengths lower than 605 nm. The NH₂-MIL displays a much higher visible light response than BDC-ligand MOF and can absorb up to 821 nm, this increasing the wavelength range into near-infrared region¹⁴¹. Considering that both samples contain the same Fe₃-μ₃-oxo clusters, the amine-group from the linkers contributes to the enhanced visible light response.

Lie *et al.* reported that NH₂-containing MIL-88B(Fe) exhibits a dual excitation pathway¹⁴². The dual excitation charge generation pathway has also been previously reported for NH₂-MIL-101-Fe. In the amino functionalized BDC MOF the charge carriers are generated through the excitation in the ligand in addition to direct charge generation in the metal cluster. The electrons from an excited ligand can be further transferred to the oxo-cluster contributing to specific redox reaction. This transfer is termed ligand-to-metal charge transfer (LMCT)^{143, 144}. The different excitation pathways are schematically illustrated in the Figure below.

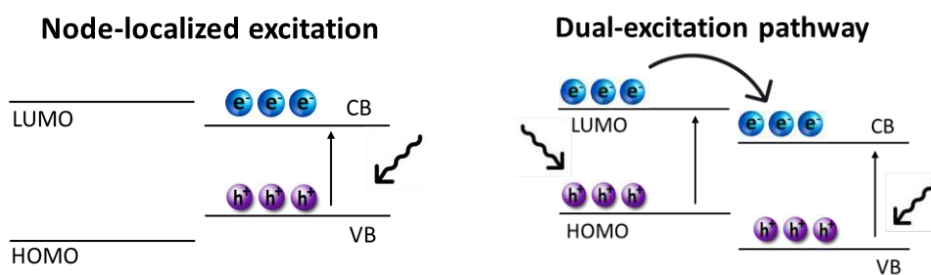


Figure 6-13 Different excitation pathways in the Fe-MOFs: a) Direct excitation in the metal cluster of MIL-101-Fe; b) Dual excitation pathway in the amine-functionalized MOFs.

Shi *et al.* reported that the separation efficiency and lifetime of photogenerated charge carriers in the NH₂-BDC MOF can be improved due to the LMCT⁷⁸. This additional electron transfer can reduce the hole-electron recombination rate and will be considered in the interpretation of photocatalytic performance. Additionally, a slower recombination rate can be expected due to the spatial separation of electrons in close proximity to the Fe ion and the holes located at the NH₂ functionality of the ligand, as reported in NH₂-MIL-101-Ti studies.¹⁴⁵

In the same paper from Shi *et al.* it was stated that the incorporation of the amine group leads to the shift of the valence band maxima (VBM) but does not affect the conduction band position, considering that the conduction band of the Fe(III)-based terephthalates is constructed from Fe 3d and O 2p states, while the N 2p states construct the valence band edge⁷⁸. In conclusion the narrower band gap is due to the shift of the HOMO level in ligand towards higher position as a direct consequence of new electronic states in NH₂-BDC.

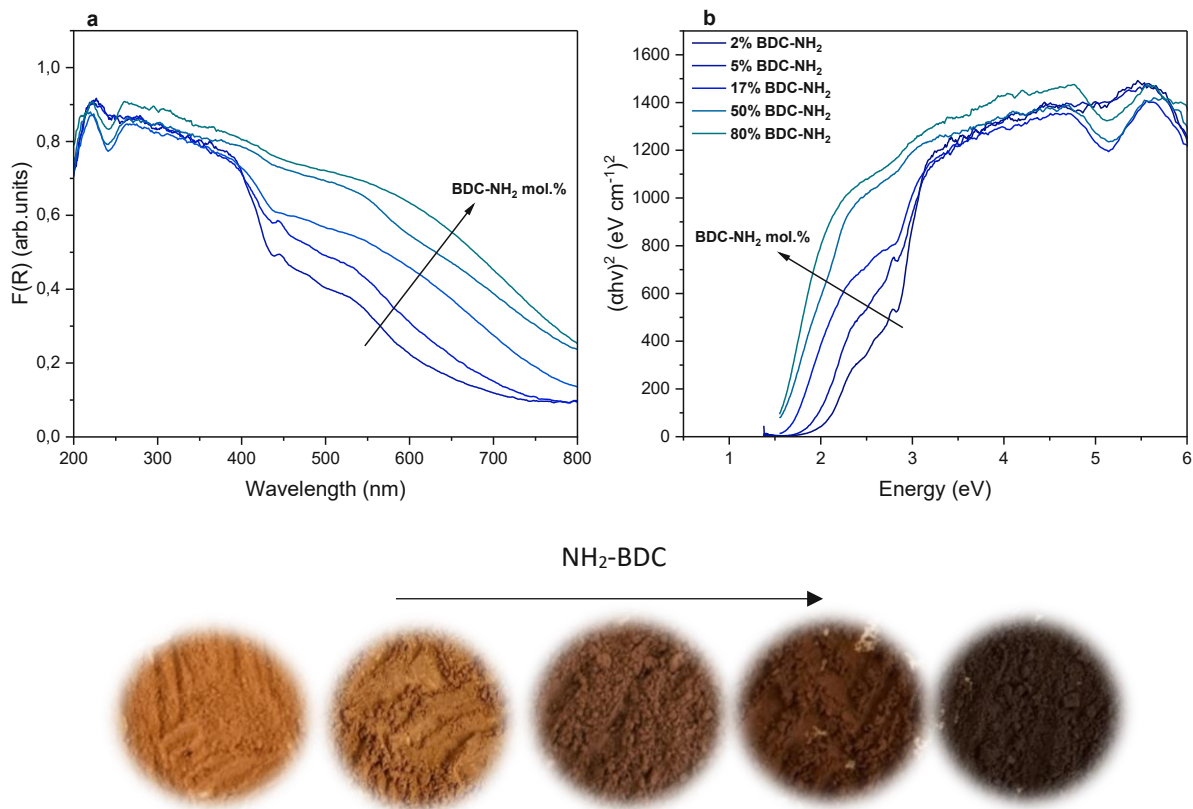


Figure 6-14 Optical Characterization of as-prepared mixed-ligand MOFs: a) Kubelka Munk functions; b) Tauc plots; c) sample colors.

Table 6-2: The optical bandgap values of mixed-ligand MOFs.

NH ₂ -BDC mol.%	E _g value (eV)
2%	2.99
5%	1.87
17%	1.64
50%	1.57
80%	1.53

The optical properties of mixed-ligand MOFs have been analyzed with UV-Vis DRS likewise. Kubelka Munk functions and Tauc plots are displayed in Fig. 6-5. The optical band gap energies are estimated and shown in Table 6-1.

The increase in NH₂-BDC ligand content enhances absorption in the visible range. This is reflected in the trend of bandgap decrease. The reason for bandgap narrowing has been described for the single ligand NH₂-MIL. Likewise, the HOMO level of the ligand is shifted to higher energies due to new bands introduced by electron donating NH₂ group.

The excitation in the oxo-cluster Fe_3O at 445 nm can be observed in samples with 2 and 5% amino-ligand. At higher substitution it is overlapped by a broad peak attributed to excitation and LMCT of $\text{NH}_2\text{-BDC}$.

In summary, the analysis using DRS demonstrates that introducing NH_2 groups through ligand modification alters the optoelectronic properties of the MOFs. Specifically, the NH_2 groups cause a shift in the position of the ligand's LUMO to higher energy levels, creating new electronic states within the bandgap of the BDC ligands. This modification enables a transfer of charges from the ligand to the metal, a process not observed in Fe-MOF without amino groups. This additional charge transfer, combined with the NH_2 groups' ability to keep holes away from electrons, suggests an expected decrease in the rate at which electron-hole pairs recombine. This finding is highly relevant for photocatalysis.

6.1.2 Single-ligand MOFs with Opposite Electronic Tuning Effect

In the previous section the influence of electron-donating $\text{NH}_2\text{-BDC}$ ligand on structural properties has been studied. To investigate the influence of functional groups with opposing electronic effect, single-ligand MOFs containing monosubstituted carboxylate ligands with electron-withdrawing groups (EWG) with different effects on the benzene ring of the ligand have been characterized and applied for the photocatalytic NRR. One of the MOFs studied was $\text{NO}_2\text{-MIL-101(Fe)}$, which has been previously reported¹⁴⁶. The other, Br-MIL-101 , has not been reported until now.

6.1.2.1 Structural Characterization of Single-ligand Fe-MOFs with Different Ligand Functionality

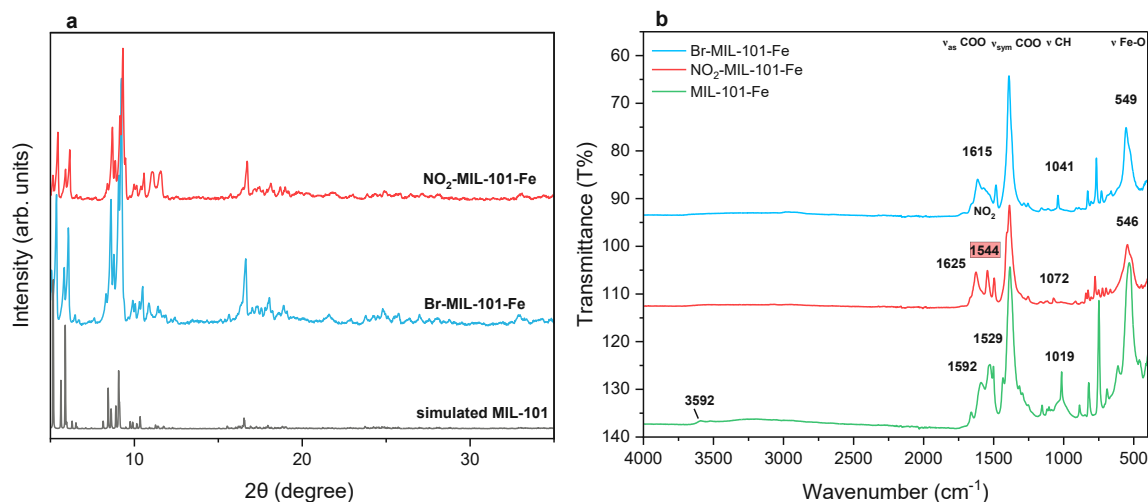


Figure 6-15 Characterization of single-ligand MOFs with different ligand functional groups: a) XRD patterns of NO₂-BDC and Br-BDC single-ligand MOFs; b) FTIR spectra of BDC, NO₂-BDC and Br-BDC single-ligand MOFs (NO₂ band marked with red shade).

The XRD pattern of the nitro- and bromo-ligand functionalized MOFs show a high crystallinity and corresponds to the MIL-101-Fe phase, without impurity compounds or secondary phases.

Once again ligand substitution model will be used to explain the formation of pure MIL-101 phase. In comparison to the amino ligand where the hydrogen bonding favored the formation of thermodynamic product MIL-88B, the lack of H-bonding in the NO₂-BDC and Br-BDC MOFs highly possible - enables the kinetic control over crystal growth because the transport of the ligands to the metal core is not restricted¹²⁷.

The FTIR spectra in Fig. 6-14b reveal the characteristic bands of as-prepared NO₂-BDC and Br-BDC Fe- MOFs, depicting the chemical and structural properties.

Table 6-3: The characteristic FTIR bands of NO₂-BDC and Br-BDC single-ligand MOFs, and MIL-101-Fe as reference.

Band (cm ⁻¹)	NO ₂ -MIL-101-Fe	Br-MIL-101-Fe	MIL-101-Fe (Reference)	Comment
ν OH	none	none	3592	-
ν _{as} COO	←1625	←1615	1592	Blue shift
ν _{sym} COO	1384	1384	1384	≡
ν CH	←1072	←1041	1019	Blue shift
δ CH	←772	←768	748	Blue shift
ν Fe-O	←546	←549	526	Blue shift
ν _{as} N-O	1544	-	-	Additional band

An additional band at 1544 cm^{-1} in NO_2 -BDC MOF can be attributed to the N-O asymmetric vibration (marked with red shade), indicating the incorporation of the ligand in the framework¹⁴⁶.

There is a blueshift of characteristic IR bands in comparison to the MIL-101-Fe reference. The stronger bonds are vibrating at higher frequencies, thus the positions of this bands in IR spectra is blue-shifted¹²³. This is the case in Br and NO_2 functionalized ligands, indicating that the interaction between the COO^{-1} ligands in NO_2 -BDC and Br-BDC MOFs is stronger than in a single-ligand non-modified BDC MOF.

It is intuitive to conclude that the EWG makes a coordination bond stronger, by pulling away the electron density and increasing the electron affinity of COO group. This is why asymmetric stretching of carboxyl group occurs at higher wavenumber. Furthermore, it affects the C-H stretching and bending of the benzene ring. This blueshift is stronger in the NO_2 -BDC MOF than in the Br-MOF due to the positive mesomeric effect and hybridization of NO_2 orbital with the linker orbitals in comparison to the electron withdrawal induced by bromine substitution¹⁴⁷.

6.1.2.2 UV-Vis DRS Spectra of Single-ligand Fe-MOFs with Different Ligand Functionality

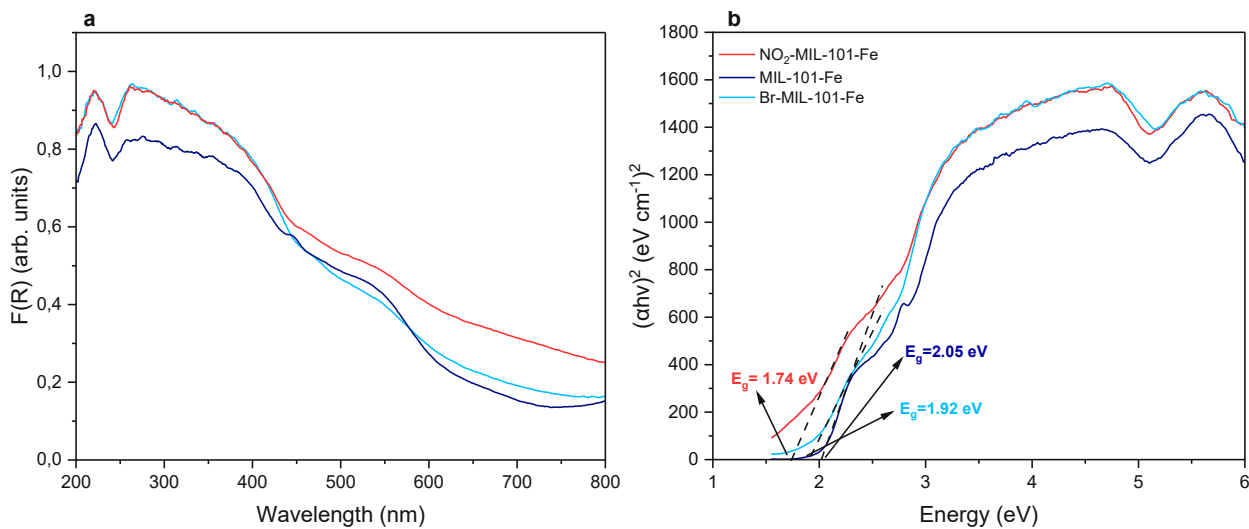


Figure 6-16 Optical Characterization of as-prepared single-ligand MOFs with different functional groups: a) Kubelka Munk functions; b) Tauc plots.

The electron transfer from the O 2p orbitals of oxygen to the iron unoccupied orbitals that was present in the DRS spectra of MIL-101-Fe, cannot be observed in ligand functionalized MOFs with electron-withdrawing groups. The reduced band gap in the NO_2 -BDC MOF could be due to the LMCT, since NO_2 has strong ability to accept electrons and hybridize with the rest of the ligand

orbitals¹⁴⁸. Based on other studies it can be hypothesized that the presence of the NO₂ group can shift the HOMO of the ligand to lower values (absolute vacuum scale) and that photoexcited electrons from the ligand into the NO₂ orbital can be subsequently transferred to the cluster by LMCT¹⁴⁸.

In the Br-BDC MOF the amount of bandgap narrowing is less significant, in comparison to MIL-101-Fe reference. There is no literature on d-orbital splitting in Fe-MOFs or more precisely the influence of negative inductive effect, which is present in Br-BDC. Searching for relevant literature I have found a report on the ligand-substitution effect on the bandgap values and positions of the orbitals in Ce-UiO-66, which is constituted of the same ligand. In the Ce-MOF bromine substitution can shift down the LUMO of the BDC ligand¹⁴⁸. Considering that the ligand in MIL-101 is the same as in Ce-UiO-66, the reported LUMO shift could be relevant, and result in this non-negligible bandgap narrowing.

None of the samples with EWG shows peak centered at 450 nm attributed to electron transfer from oxygen to iron. Thus, both EWGs influence the charge transfer properties due to the higher binding strength between ligands and the cluster. The hybridization of NO₂ with ligand orbitals could hinder this electron transfer, by changing the position of O 2p orbitals. On the other hand, the negative inductive effect of bromine on BDC ligand can influence the splitting of energy levels in cluster disabling the O²⁻_{2p} → Fe³⁺_{3d} electron transfer.

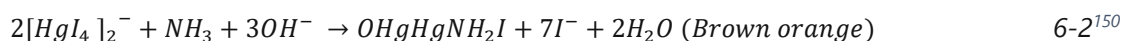
6.2 Effect of Ligand Tuning on Photocatalytic Nitrogen Reduction Reaction

DRS analysis has provided insight into optoelectronic properties of the as-prepared MOFs. It was discussed that the introduction of amine functional groups changes the position of the VBM, not affecting the CB position. The reduced bandgap resulted in extended light response. Furthermore, the introduction of functional groups with opposite electronic effect results also in the band gap narrowing, which is stronger in nitro containing MOF. In order to further investigate the effect of ligand tuning on activity in the photocatalytic NRR, varying ratios of NH₂-BDC ligand in the mixed-ligand Fe-MOFs and single-ligand Fe-MOFs factionalized with different ligands have been investigated. The experimental set-up was described in *Section 5.3.1*. Parameters have been set identically for all experiments. The experiments were conducted in water without sacrificial

agent. All samples were activated in vacuum at 100 °C overnight in order to remove adsorbed surface molecules.

6.2.1 Nessler's Reagent Ammonia Detection Method

Nessler's reagent is a solution containing K_2HgI_4 and KOH or NaOH. Iodide and mercury ions react with ammonia under alkaline conditions to produce a reddish-brown complex. This complex absorbs at 420 nm. This absorbance is directly proportional to the ammonia concentration¹⁴⁹.



In comparison to other detection methods like ion chromatography which offers high sensitivity and reproducibility, Nessler's reagent method does not differ. These methods were previously compared and showed that the determined concentration corresponds to the nominal ammonia concentration. As reported Nessler's reagent method is also insensitive to the pH value at pH 7 and above¹⁵⁰.

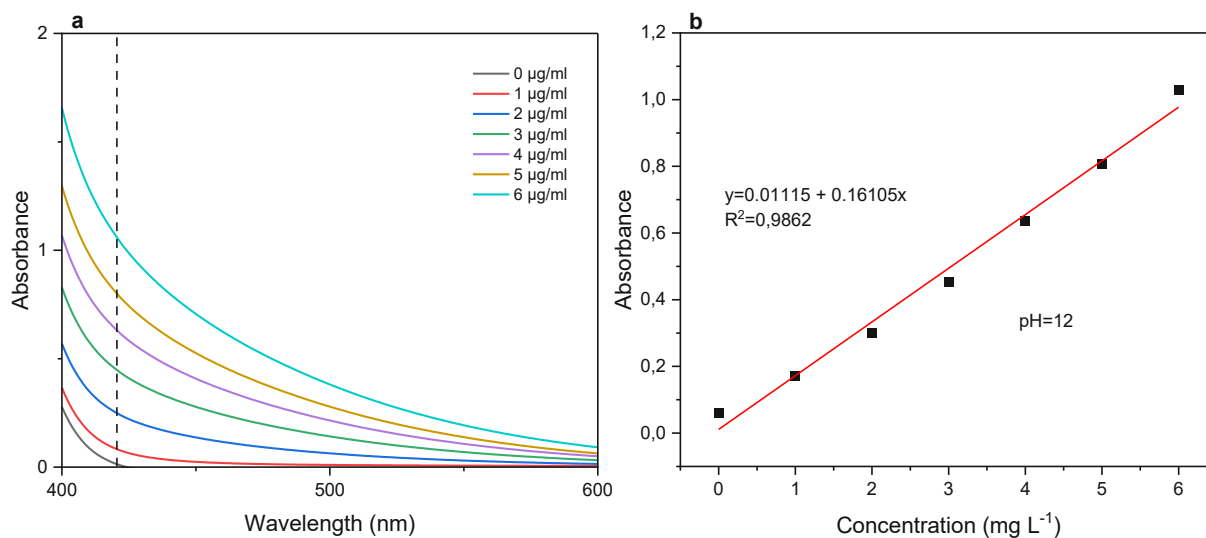


Figure 6-17 Ammonia detection via Nessler's reagent method: a) UV-Vis absorption curves of different concentrations of NH_4^+ ions using Nessler's reagent method; b) A calibration curve used to estimate the concentrations of NH_4^+ ions; c) Standard solutions of different NH_4^+ concentrations.

6.2.2 Investigation of Photocatalytic Behavior of Single- and Mixed-ligand Fe-MOFs

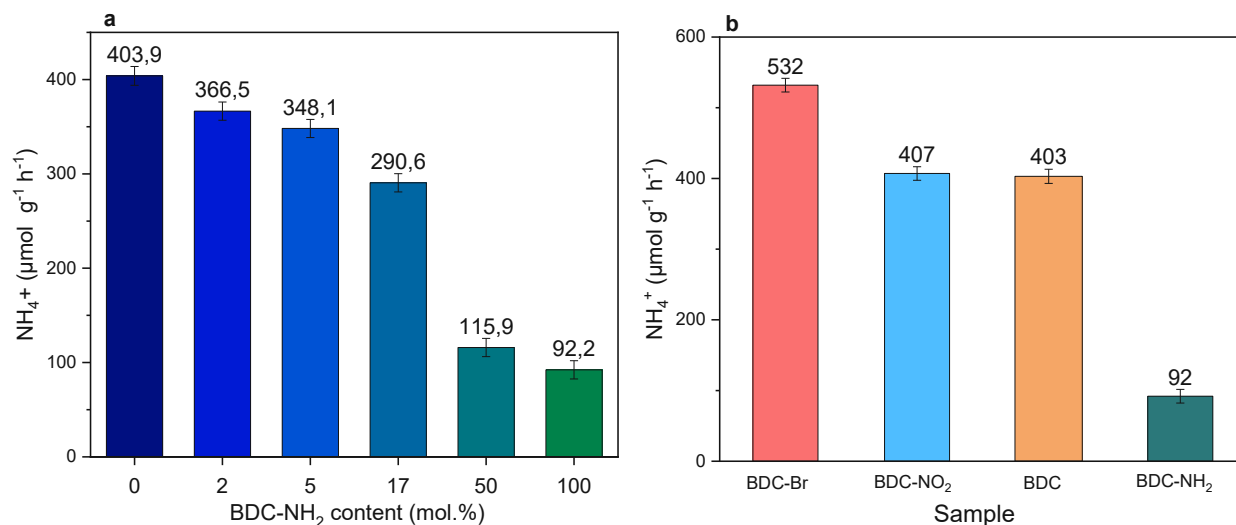


Figure 6-18: Photocatalytic NH_4^+ production rate under ambient conditions in water without sacrificial agent: a) Mixed-ligand MOFs with different ratio of NH_2 -BDC ligand; b) Single-ligand MOFs with different functional groups.

Table 6-4: Normalized NH_4^+ production rate with respect to single-ligand MIL-101-Fe.

NH_2 -BDC mol.%	NH_4^+ ($\mu\text{mol g}^{-1} \text{h}^{-1}$)	Yield ratio vs. MIL-101-Fe (%)
0	403.9	100
2	366.5	90.7
5	348.1	86.2
17	290.6	71.9
50	115.9	28.7
100	92.2	22.8

In Fig. 6-14a the NH_4^+ production rate of mixed-ligand Fe-MOFs is displayed, whereas the single ligand BDC and NH_2 -BDC MOFs were used as reference.

Increasing the BDC-NH₂ content leads to a decrease in NH_4^+ production rate. The production rate of NH_4^+ in BDC-MOF was $403.9 \mu\text{mol g}^{-1} \text{h}^{-1}$ and decreased to $92.2 \mu\text{mol g}^{-1} \text{h}^{-1}$ for NH_2 -BDC MOF. The decrease is proportional to the percentage of NH_2 -BDC, but it is not linear (Table 6-3). The difference in the yield between single BDC MOF and 2% NH_2 -BDC MOF is 10%. Further yield decrease between 5 and 17mol.% NH_2 -BDC is proportional to the difference in relative amount of amino ligand. The sample containing 50 mol.% of NH_2 -BDC produces 28% initial of yield obtained with single-ligand BDC MOF. The MOFs with 50 and 100 mol.% NH_2 -BDC show just 6% difference in NH_4^+ production rate.

The yield decrease with increasing BDC-NH₂ ligand content could be attributed to the decrease of relative amount of active BDC-ligand SBU. Since the relation is not linear the amount of NH₂-BDC ligand does not reduce the effect of active species but has another contributory effect.

To further examine the reason behind different photocatalytic performances, the influence of ligand tuning, with electron-withdrawing groups compared. The ammonium production rate of single-ligand MOFs is shown in Fig. 6-14b. The difference in NH₄⁺ production rate between single-ligand BDC and NO₂ is negligible, while the bromine functionalization results in 23.5% of yield increase.

One of the possible interpretations could be increasement in acidity of Fe³⁺ centers, which act as Lewis's acids or electron acceptors. The Lewis's acidity of the Fe³⁺ centers has been reported by Ferey's group on MIL-100-Fe. The terminal water molecules from these sites are removed after activation at elevated temperature and become accessible¹⁵¹.

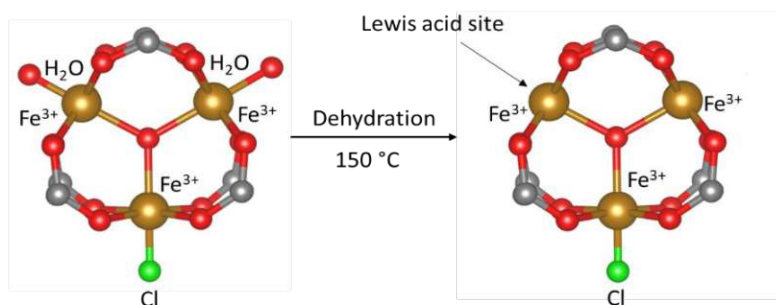


Figure 6-19 Formation of CUS in Fe-terephthalate MOF reported by Yoon et al.¹⁵¹.

Since the SBU of MIL-101 is identical containing same ligand, assuming the creation of open metal centers after activating MOFs is reasonable. The introduction of EWG onto ligands could enhance the acidity of metal centers. The electron density could be pulled away from the BDC-ligand lowering its electron affinity and affecting the activity of metal center. This effect has been reported on the NO₂-MIL-101-Cr for the application in gas sorption, where the Lewis acidity of metal center increased due to the substituent induced electron withdrawl¹⁵².

To check if this theory is relevant, the FTIR spectra have been compared and the most significant bands are presented in Table 6-4.

Table 6-5: FTIR band for comparison of electron withdrawing effect on significant bands in the SBU.

Band (cm ⁻¹)	NO ₂ -MIL-101-Fe	Br-MIL-101-Fe	BDC-MIL (Reference)
v _{as} COO	1625	1615	1592
v _{sym} COO	1384	1384	1384
v CH	1072	1041	1019
δ CH	772	768	748

The effect of electron withdrawal from iron-oxo cluster, could be already observed in the blueshift of IR bands (Figure 6-1b) corresponding to the vibrational modes of incorporated ligands. However, the effect is more significant in the nitro containing MOF. Except for the symmetric COO⁻¹ stretching mode, which is identical, other bands of the ligand are vibrating at higher frequencies. Hence, the increase in Fe³⁺ acidity should be more significant in NO₂-BDC than in Br-BDC MOF.

Since ammonium production yield is inversely proportional to this effect, it has to be another effect contributing to the enhanced activity of bromine substituted Fe-MOF. Recall that the single NH₂-BDC MOF had lowest production yield. A possible explanation of this trend is that the decrease is a consequence of proton capture by the amine group of terephthalic acid ligand which is Bronsted base.

In addition to its beneficial impact on the NRR, where it enhances the acidity of Fe³⁺, the nitro group, characterized by its electron-withdrawing properties, readily accepts electrons, leading to an accumulation of negative charge on the oxygen atoms within the NO₂ group. This excess negative charge may act as a potent sink, effectively capturing photogenerated holes. Consequently, this process dampens the kinetics of the oxidation half-reaction, diminishing the number of available protons and impeding the conversion rate.

Conversely, incorporation of acidic bromine in the structure of Fe-MOF through mono-substituted terephthalic acid raises the intrinsic acidity of the ligand. This modification effectively acts as a proton pump, increasing the reservoir of available protons at the catalytically active site. This, in turn, accelerates the kinetics of proton-coupled electron transfer process and the overall conversion efficiency^{2.5}.

6.3 Studies on Selective Ligand Removal Strategy

The second part of the thesis focuses on the investigation of heat-treatment on mixed-ligand $x\text{NH}_2\text{-MIL Fe-MOFs}$. This part of the work is based on already reported selective ligand removal strategy as approach for improving accessibility of active metal sites²⁵. The effect of thermal treatment and the possibility of thermolabile ligand removal will be described. All the studies have been conducted in under air atmosphere. Throughout the studies heating-rate has been kept constant for reproducibility of the data.

6.3.1 TGA of Mixed-ligand Fe-MOFs

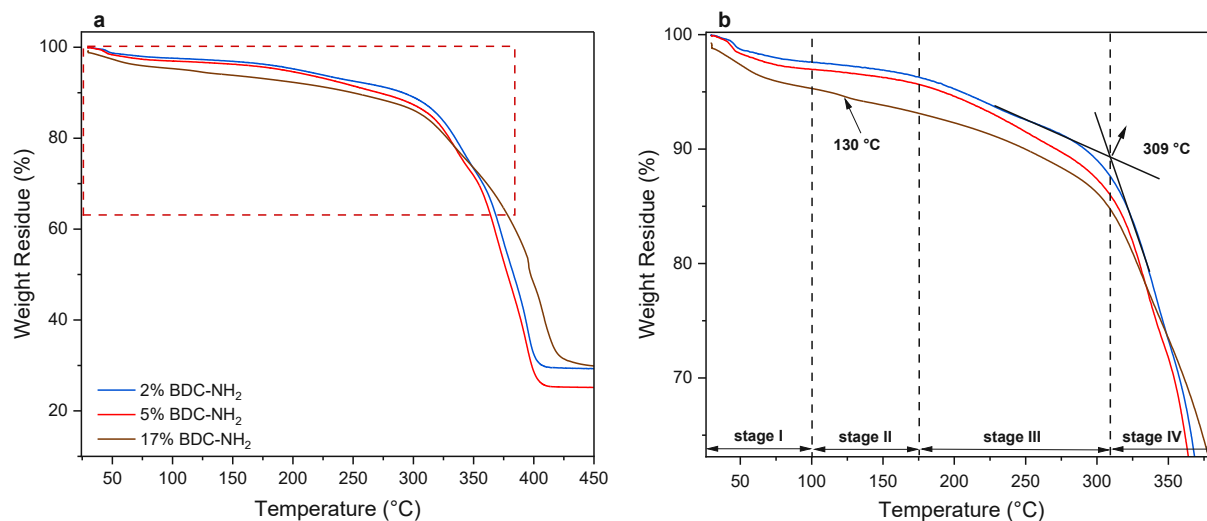


Figure 6-20 Thermal stability of mixed-ligand Fe-MOFs with different ratio of BDC-NH₂ to BDC: a) TGA of as-prepared MOFs; b) Enlarged region of onset degradation temperature.

TGA analysis displayed the presence of three main weight losses within the temperature range of 25-400 °C. In the temperature range between 25 and 175 °C, weight loss has occurred due to the evaporation of adsorbed guest molecules such as solvent and water and solvent molecules trapped inside the pores of the MOFs. This region can be divided into 2 stages. The first one belongs to the evaporation of adsorbed species from the surface up to 100 °C, and Stage II marks the release of trapped solvent molecules. Although pure DMF would evaporate at 153 °C, the stronger interaction with the matrix requires higher temperature up to 175 °C to remove trapped solvent.

In the second stage of weight loss in 17 mol.% NH₂-ligand there is a change in slope at 130°C which can be due to the different phases but cannot be stated with certainty, because it can also be that there is a lot more adsorbed molecules that interact stronger with framework which makes this slope change significant.

The second weight loss can be assigned to the decomposition of the NH₂-BDC ligand, which occurs between 175 °C and 310 °C. This is intuitive interpretation of the weight loss in the second stage. However, previously reported TGA analysis of on isomorphic single-ligand Cr-MIL-101 has interpreted a second stage of weight loss as a departure of OH/Cl group from the SBU⁴¹.

The onset temperature of decomposition of the framework increases with increasing NH₂-ligand ratio. Most probably this is related to the kinetic restrictions as the relative content of NH₂-BDC is higher.

Above 310 °C decomposition of the terephthalic acid can be observed. The residual weight of mixed-ligand MOFs decreases with increasing NH₂-BDC fraction and equals to 29.5% for 2%NH₂-MIL and 25.3% for 5%NH₂-MIL.

The residual weight loss for 17%NH₂-MIL-101-Fe is 30.7% which is opposite to the trend before, indicating that the framework structure is more stable. This is in accordance with the previously observed secondary thermodynamic phase (*Section 6.1.1*).

Table 6-6: Weight residue at different weight loss stages.

NH ₂ -BDC (mol.%)	Stage I + II (°C)	Weight residue (%)	Stage II (°C)	Weight residue (%)	Stage III (°C)	Weight residue (%)
2	25-175	96.6	175 – 312	89.3	309 - 406	29.5
5	25-175	95.7	175 – 314	86.8	311 - 411	25.3
17	25-175	94.8	175 – 304	87.5	306 - 426	30.1

Based on TGA studies it can be concluded that NH₂-BDC ligand is more thermolabile than BDC ligand and that heating in the temperature range of Stage II allows removal of this ligand. However, it has to be noted that onset temperature of framework degradation is in the range between 306 and 311 °C depending on NH₂-BDC content and heat-treatment has to be applied carefully in order to preserve the structure.

6.3.2 In-situ DRIFTS Studies on Mixed-ligand Fe-MOFs

The 2%NH₂-MIL-101-Fe has been chosen as a representative sample to gain further understanding in the mechanism of selective ligand removal and structural changes upon heat treatment *via* in-situ DRIFTS.

6.3.2.1 In-situ DRIFTS Study of 2%NH₂-MIL-101-Fe upon Ramp Heating

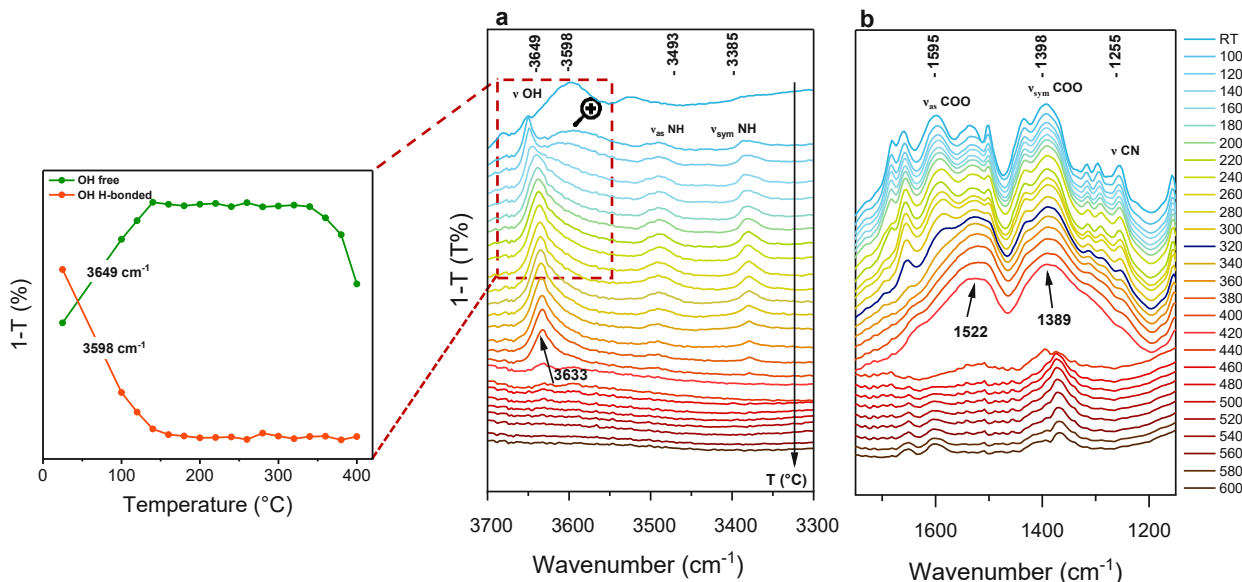


Figure 6-21 In-situ DRIFTS measurements of 2%NH₂-MIL-101-Fe during heating up to 600 °C with ramp rate of 5 °C min⁻¹.

In the enlarged spectrum the shift of the OH-group can be observed with temperature increase. Broad peak at 3598 cm⁻¹ presents H-bonded OH group. The peak at 3649 cm⁻¹ corresponds to the free OH group form the coordination with metal. H-bonded OH group can still be observed until 140 °C, when the DMF is released from the framework structure. The free OH-group is quite prominent after solvent removal and is preserved coordinated, but it shifts as the rest of the framework goes through structural changes upon heating. Still, this band is presents up to 400°C temperature at which the frameworks are completely degraded, indicating strong interactions. This observation supports the hypothesis that the formation of [Fe₃O(BDC)₃(OH₂)₂X] is favorable in the presence of amino-containing ligands, as introduced in Section 6.1.1.5.

At 320 °C (dark blue line in Fig. 6-17b) all framework representative bands disappear. This can be observed on asymmetric and symmetric COO⁻¹ bands with resonance frequency at 1595 and 1398

cm^{-1} , respectively. This stretching disappears completely after 320 °C denoting the structure collapse and appearance of free BDC ligand with carboxylate group vibration modes at 1522 and 1389 cm^{-1} .

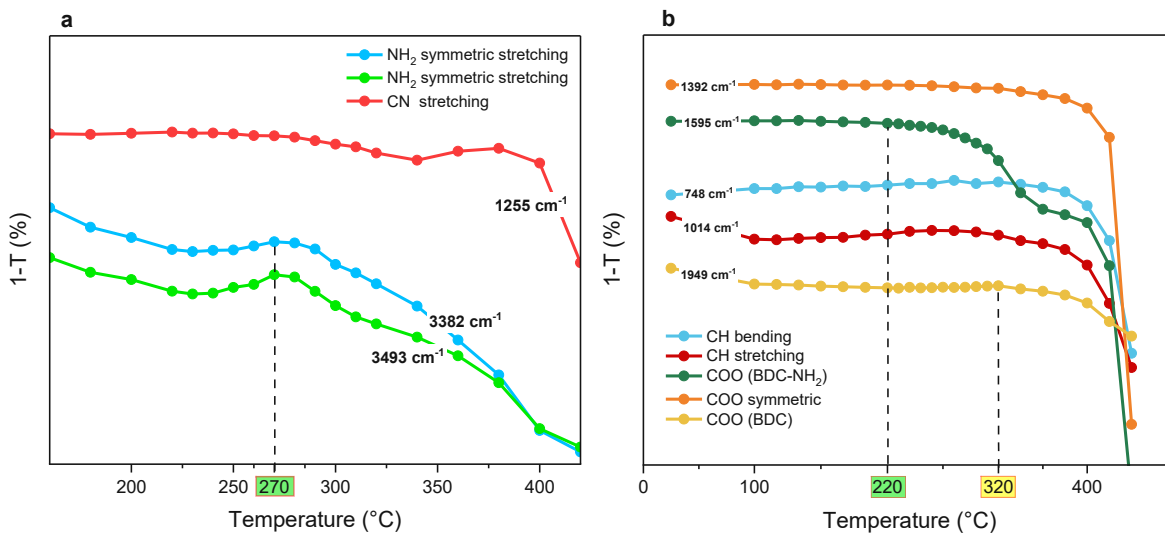


Figure 6-22 Changes in the intensity of characteristic IR band as function of temperature: a) IR bands associated to the NH_2 -BDC ligand; b) IR bands of the characteristic framework vibrations.

The NH_2 stretches are highly H-bonded before the removal of the DMF from the framework. Thus, the intensity of these bands decreases as the solvent is removed (Fig 6-18a). Finally, they have the highest relative intensity at 280 °C and take a descending trend upon further temperature increase. The intensity of CN vibration decreases simultaneously with NH vibration. The information obtained from observing this band has to be carefully interpreted, since the relative intensity is very low, and it looks like the intensity increases after 340 °C although the framework degrades at this temperature.

At 220 °C the intensity in COO^{-1} asymmetric stretching characteristic for NH_2 -BDC ligand (green band in Fig. 6-18b), starts to decrease and follows 2-step cleavage from the SBU, as previously reported on MIL-125²⁵. The intensity of this band at 1595 cm^{-1} decreases in the temperature range between 220 °C and 400 °C. The first step is the one-side cleavage of SBU-BDC- NH_2 coordination, followed by continuous transition in the second stage of bond cleavage, in which second ligand-SBU coordination breaks.

In Fig. 6-18b other framework representative bands are displayed. The relative intensity of these bands gradually decreases after 320 °C, meaning that the cleavage of BDC-SBU coordination begins.

In conclusion, the cleavage of the BDC-NH₂ ligand starts considerably before the cleavage of BDC ligand; however, the former process occurs over a wide temperature range. Complete ligand removal cannot be accomplished before the framework begins to collapse. Nonetheless, the partial cleavage of one coordination side which provides free active metal centers can be achieved at optimal conditions. The temperature window of the partial cleavage is between 220 and 320 °C. For finding optimal temperature and time further experiments are needed.

6.3.2.1.1 Isothermal In-situ DRIFTS Study of 2%NH₂-MIL-101-Fe

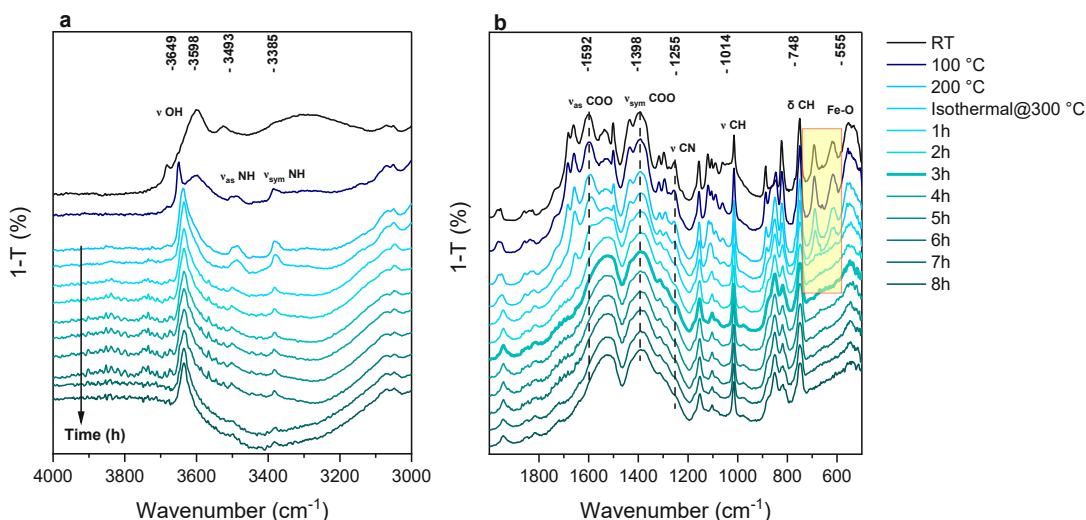


Figure 6-23 Isothermal in-situ DRIFTS measurements of 2%NH₂-MIL-101-Fe at 300°C in air atmosphere.

Isothermal DRIFTS studies have been conducted in order to obtain an optimal time at which maximal intensity of NH₂ bands decrease could be achieved. In the range of higher frequencies between 3000 and 4000 cm⁻¹ the OH band and NH₂ stretching can be observed. At room temperature the symmetric and asymmetric NH vibrations are overlapped by the broad band of adsorbed solvent molecules. The bands can be seen more clearly at 100 and 200 °C. The intensity of these bands starts to decrease at 300 °C with the dwelling time. Parallel to the NH vibrations the CN stretching mode of the benzene ring at 1255 cm⁻¹ follows the same trend and becomes insignificant after 3h isothermal heating at 300 °C.

The prominent band of C-H bending and stretching at 748 and 1014 cm^{-1} which have been assigned in the interpretation of FTIR spectra (Section 6.1.1.3) are being preserved also after 8 hours of dwelling at 300 °C. The intrinsic Fe-O stretching vibrations in the sample 2%NH₂-BDC as already discussed has two different modes corresponding to the different phases. The one at higher frequency was the one belonging to the thermodynamic stable phase and is more stable upon thermal treatment. The other one vanished above 200 °C. The two bands marked with yellow shadow assigned to the C-H bending of the benzene ring disappear after dwelling for 1h at 300 °C. The effect of thermal treatment on asymmetric carboxyl stretching results in a similar behavior of this group like the increasing the NH₂-BDC ligand content. The additional peak at 1529 cm^{-1} corresponding to the MIL-101 phase merges with the O-C-O band at 1592 cm^{-1} to a broad peak.

In summary, the isothermal DRIFTS studies reveal broader bands attributed to the partial cleavage of ligands and increased hydrogen bonding between framework constituents. However, structural integrity is maintained for up to 3 hours at 300 °C during isothermal heating.

6.3.3 In-situ XRD of Mixed-ligand Fe-MOFs

As candidates for the evaluation of thermal stability the samples with 2 and 5 mol.% NH₂-BDC were chosen. Based on previous TGA analysis these samples are stable up to temperatures of 309 and 311 °C, respectively, at which decomposition of the main framework linker BDC starts.

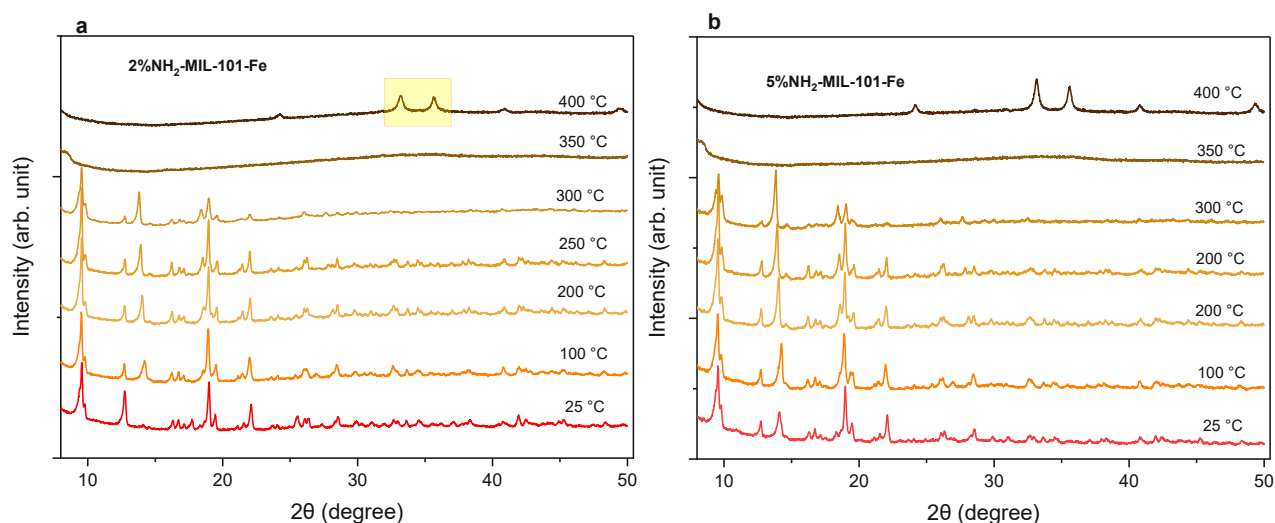


Figure 6-24 In-situ XRD patterns of mixed-ligand MOFs: a) 2%NH₂-MIL; b) 5%NH₂-MIL.

The measurements for both samples were conducted under compressed air flow and a temperature of up to 800°C. Selected XRD patterns for characteristic temperatures of 2% NH₂-MIL and 5%NH₂-MIL are shown in *Figure* above.

Heating up to 250 °C has not affected the crystalline structure of the samples as the characteristic diffraction pattern is preserved. Further heating up to 300 °C leads to a remarkable decrease in peak intensity. The diffraction pattern of the MOF disappears completely at 350 °C, indicating degradation of the BDC, which is in accordance with TGA analysis. Above 400°C new peaks can be observed at 32.2° and 35.7 °, which are due to the formation of α -Fe₂O₃¹⁵³ particles after removal of the ligands and subsequent oxidation to hematite.

In accordance with TGA data the framework decomposition due oxidative degradation process occurs above 300 °C. No phase transformation can be observed by increasing the temperatures. The fact that increase of the amino-ligand content does induce the phase transformation and the thermal heating does not, implies the formation of different phases at the nucleation stage. This highlights the significance of varied electrostatic interactions between amino and non-amino containing ligands during this stage.

6.3.4 Conclusion on Selective Ligand Removal Parameters

Based on the data obtained from the in-situ XRD and DRIFTS as well as the TGA analysis, mixed-ligand samples decompose into amorphous state at temperatures above 300°C. The starting temperature of decomposition increases with increasing NH₂-BDC content due to kinetic restriction. Dwelling the samples at 300 °C for 3h leads to a significant decrease in the characteristic IR bands. Ramping DRIFTS studies imply the possibility of partial removal of the thermolabile ligand from the framework structure. However, the second stage of 2-step removal coincides with the framework degradation process. Terminating the removal process after partial cleavage on one coordination side which could provide unsaturated metal sites is feasible.

The parameters obtained from preliminary experiments can be summarized as follows:

Table 6-7: Summary on optimal thermolysis parameters.

TGA	>306 °C framework degradation.
DRIFTS	220 °C NH ₂ -BDC ligand cleavage start. 320 °C BDC ligand cleavage start. 3h at 300 °C significant decrease in NH ₂ -ligand bands.
XRD	3h at 300 °C crystallinity preserved.

Based on the parameters from this table, the optimal time and temperature were chosen to be 3h and 300 °C. After treatment the samples showed high crystallinity (*Fig.6-21*), but not expected properties, as will be discussed in following sections.

6.3.5 Characterization of Heat-treated MOFs

The highest NH₂-BDC ratio in the mixed-ligand MOFs with crystalline structure after thermal treatment was the one containing 17mol.% BDC-NH₂ ligand. Relying on data obtained from XRD measurements of mixed-ligand MOFs, this can be grounded on the fact that the thermodynamic framework structure is dominant and that removing of main framework constituent in MOFs with 50 and 80% NH₂-BDC, causes the overall framework collapse.

6.3.5.1 XRD of the Heat-treated Mixed-ligand Fe- MOFs

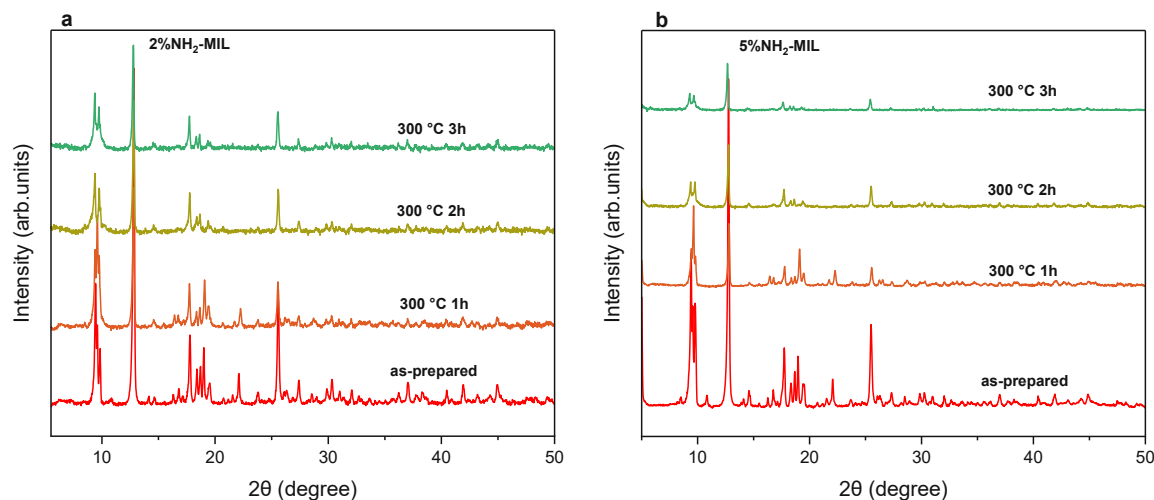


Figure 6-25 Ex-situ XRD measurements of heat-treated mixed-ligand MOFs thermolyzed in air atmosphere at 300 °C for different time intervals: a) 2%NH₂-MIL b) 5%NH₂-MIL.

The crystalline pattern is preserved upon isothermal heat treatment at 300 °C. The samples that have been thermolyzed for 2 and 3h show significant loss of the peak intensities but all reflex positions are still maintained. The sample containing 5 mol.% of NH₂-BDC has a more notable loss of the peak intensity than the sample with 2 mol.% NH₂-BDC. Assuming that the ligands are distributed randomly over the framework, the relative amount of thermolabile NH₂-BDC ligand is higher so that during thermal treatment structural planes are affected equally. This can explain why the decrease in peak intensity after thermal treatment is inversely proportional to the amount of NH₂-BDC ligand.

Based on presented data the parameters at which the crystallinity has been preserved and NH bands have been noticeably reduced are the temperature of 300 °C and time of 3h. The samples thermolyzed at these parameters have been further characterized.

6.3.5.2 Effect of Heat-treatment on Porosity of Mixed-ligand Fe-MOFs

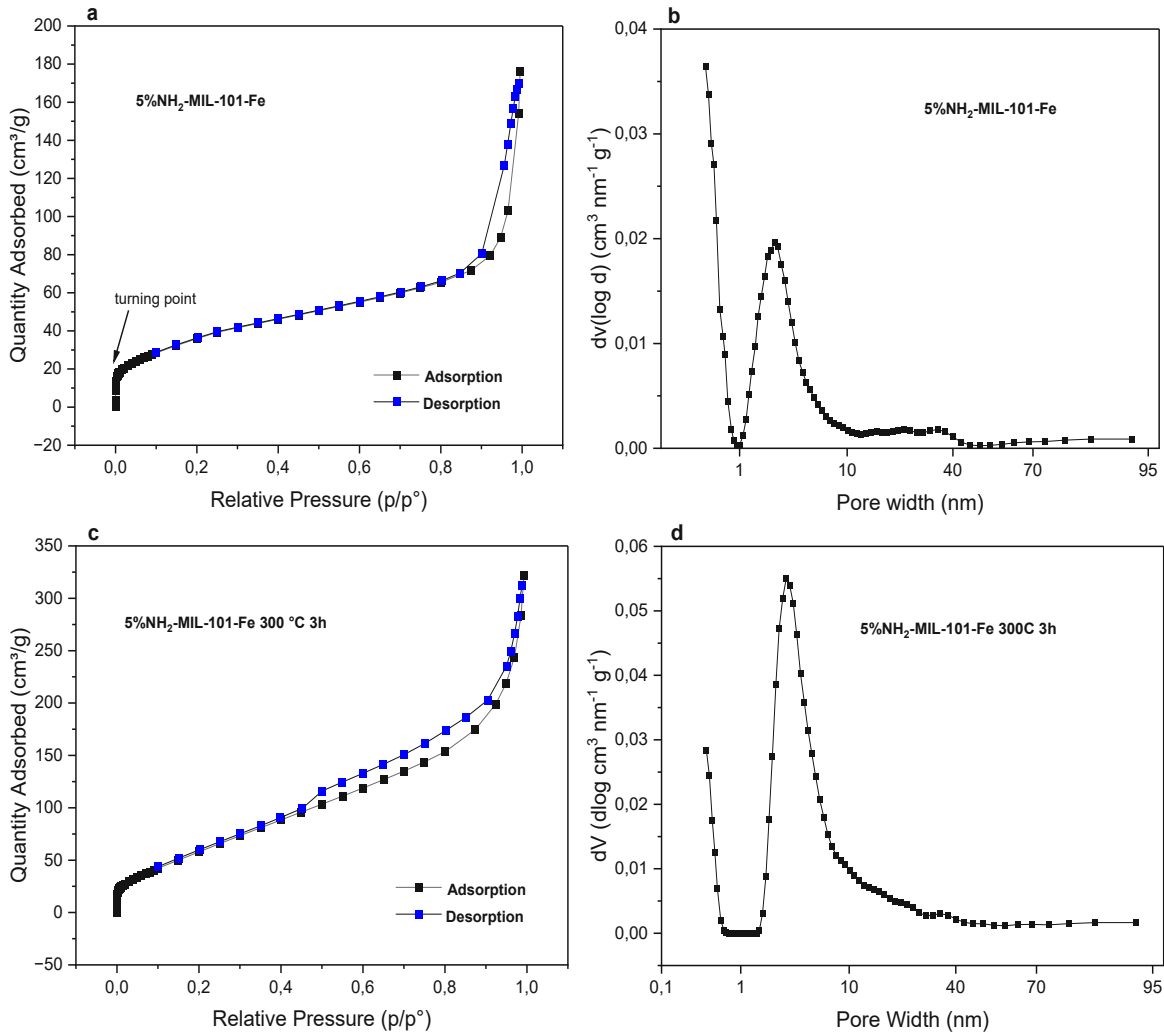


Figure 6-26 N₂ physisorption isotherms at 77K and corresponding pore size distribution of 5%NH₂-MIL: a) and b) before treatment; c) and d) after heat-treatment for 3h at 300 °C.

Table 6-8: BET specific surface area and pore volume of as-prepared and heat-treated samples.

Sample	S _{BET} (m ² g ⁻¹)	Pore volume (cm ³ g ⁻¹)
5%NH ₂ -MIL pristine	332	0.408
5%NH ₂ -MIL SeLiRe	247	0.337

The isotherms before and after thermal treatment correspond to the Type IVa isotherms by IUPAC where the capillary condensation is accompanied by a hysteresis loop, indicating the mesoporous material¹⁵⁴.

At low pressure an almost vertical curve indicates the micropore filling, where all the adsorbent molecules are in contact with the surface. The monolayer coverage can be distinguished from the multilayer coverage, since there is a turning point in both samples. The hysteresis loop is narrow corresponding to the H4 type indicating the cavitation induced desorption due to the pore blocking.

Regarding the pore size distribution, the amount of micropores is dominant in untreated mixed-ligand sample.

After heat treatment the hysteresis loop has less steep gas uptake at high relative pressures denoting that there is less defined mesopore volume and a broader pore size distribution. This can be confirmed in the incremental pore size distribution graph where the relative amount of the mesopores centered at 3 nm dominates over the amount of micropores.

6.3.5.3 Effect of Heat-treatment on the Microstructure of Mixed-ligand Fe-MOFs

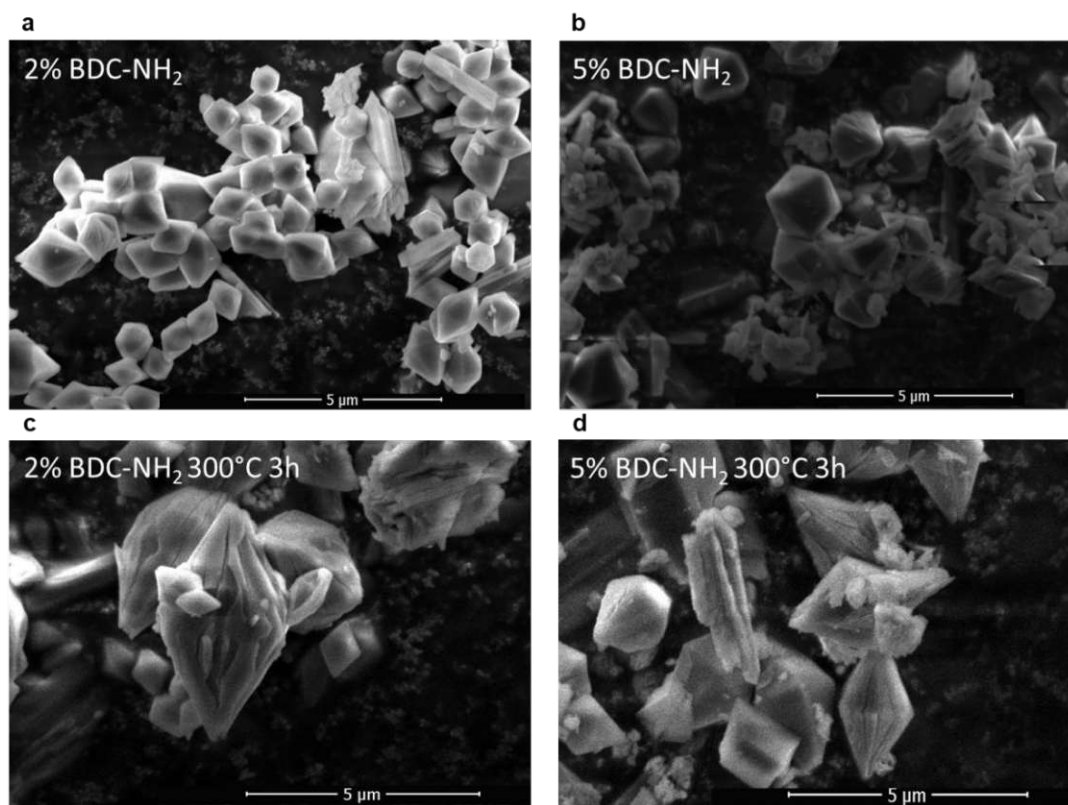


Figure 6-27 SEM images of mixed-ligand MOFs before and after heat treatment: a) 2%NH₂-BDC MOF as-prepared; b) 5%NH₂-BDC MOF as-prepared c) 2%NH₂-BDC MOF heat treated; d) 5%NH₂-BDC MOF heat treated.

The as-prepared samples have a regular hexagonal morphology. The average length of 2%NH₂-MIL samples is 1.54 μm and the average diameter is 1.32 μm, whereas the average length of 5%NH₂-MIL is 1.50 μm and 1.22 μm average diameter. Although, average particle size is inversely proportional to BDC-NH₂ content, SEM images have been collected for just 2 mixed-ligand MOFs, making it difficult to determine the impact of the ligands on the crystal growth.

After heat-treatment the particle size distribution is very inhomogeneous, so average values were not estimated. The surface cracks are introduced after treatment. Considering the significant crack growth and initial concentration of the NH₂-BDC ligands of 2 and 5 mol.%, it can be barely stated that the treatment resulted in partial cleavage of the coordination bonds. After treatment of 2% NH₂-BDC MIL (*Fig. 6-22c*) the magnified octahedral particle has quite deep cracks that could not be due to the cleavage of the present ligand. There is another effect to be considered, which is yet unclear.

However, it is foreseeable that particles with rough surfaces could be beneficial for photocatalytic activity. The benefits of cracks for photocatalytic NRR have been introduced by Guo *et al.* In the paper aiming at the same application of Fe-based MOF, the adsorption of the reactants on the rough surface was promoted. Additionally, as reported multiple refractions of light as a consequence of structural defects resulted in increased light utilization¹¹⁵.

6.3.5.4 UV-Vis Diffuse Reflectance Spectroscopy of Heat-treated MOFs

DRS spectra of as-prepared mixed-ligand MOFs have been compared to investigate the influence of thermolysis on optoelectronic properties. Additionally, single BDC MIL-101-Fe has been subjected to thermal treatment as a reference.

Table 6-9: Optical band gap values of as-prepared and heat-treated samples.

NH ₂ -BDC mol.%	E _g as-prepared (eV)	E _g Heat-treated (eV)	E _g Difference
0	2.05	1.81	0.24
2	1.98	1.74	0.24
5	1.86	1.65	0.21
17	1.67	1.49	0.18

The results of DRS analysis with corresponding differences in band gap values after heat-treatment is summarized in *Table 6-7*. All samples show the same trend in band gap narrowing.

The narrowing of the optical band gap can be explained as the ligand removal accompanied with vacant coordination place that is not replaced by any other bond. Since the ligand bridges the metal center with oxygen atoms, these vacant places can be regarded as oxygen vacancies (OVs)¹⁵⁵.

Oxygen vacancies have been well studied in the field of ceramics and lately a lot of research on functionality tuning of the perovskite and shifting the conduction band minima to lower energy values has been carried out. In the other fields of material science, oxygen vacancies and their effect on the physical and optoelectronic properties have been studied immensely in fundamental studies as well as in application related research. Introducing of additional electronic levels below the conduction band through a defect engineering has also been widely applied in the photocatalysis^{83, 84, 85}.

Although the interpretation of the band edge positions in the MOFs consisting of the cluster and ligand is not as simple as the assignment of the edge positions in the metal oxides, the Fe-MIL consists of the metal cluster that is responsible for charge generation. Therefore, defect introduction in the cluster could provide new levels below the conduction band of as-prepared MOFs.

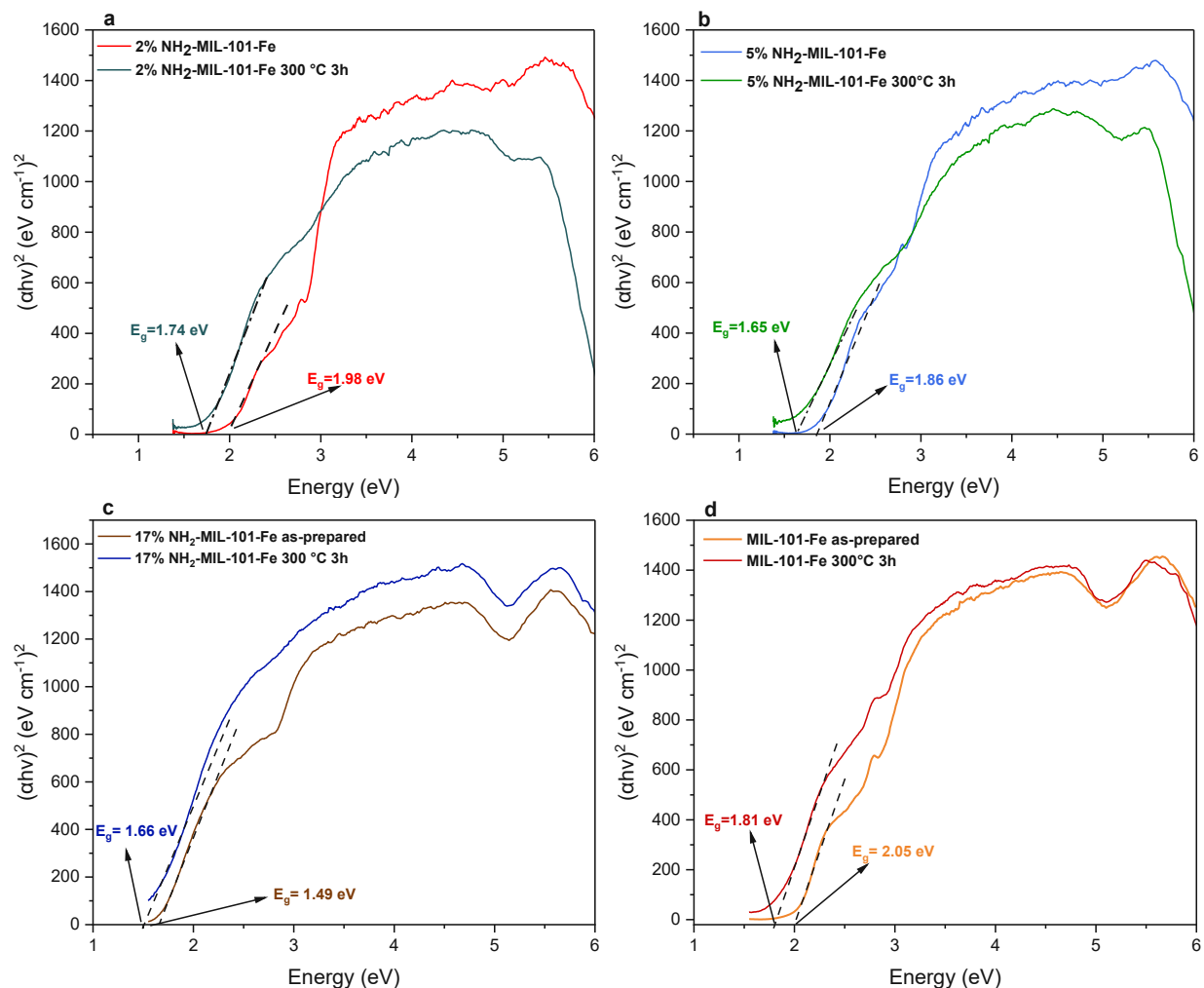


Figure 6-28 Comparison of Tauc plots with corresponding optical band gap values before and after heat treatment: a) 2%NH₂-MIL as-prepared and heat-treated sample; b) 5%NH₂-MIL as-prepared and heat-treated sample; c) 17%NH₂-MIL as-prepared and heat-treated sample; d) single-ligand MIL-101-Fe as-prepared and heat-treated.

The reference spectra of MIL-101-Fe displayed in Fig. 6-24d do have the same decrease in band gap as the mixed-ligand MOFs, indicating that thermal treatment could introduce a significant amount of structural defects also in the non-amino ligand MOF. The position of created mid-gap electronic states is assumably the same for all samples. The peak belonging to the transition of the oxygen electrons to unoccupied d-orbitals of Fe³⁺ localized at 445 nm, has vanished after thermolysis confirming the hypothesis on OV's creation, which are positively charged and can trap electrons. Since the conduction band of as-prepared samples is constituted of Fe 3d and O 2p states, the new oxygen vacant electronic levels explain the disappearance of this band.

6.3.5.5 FTIR Spectra of Heat-treated MOFs

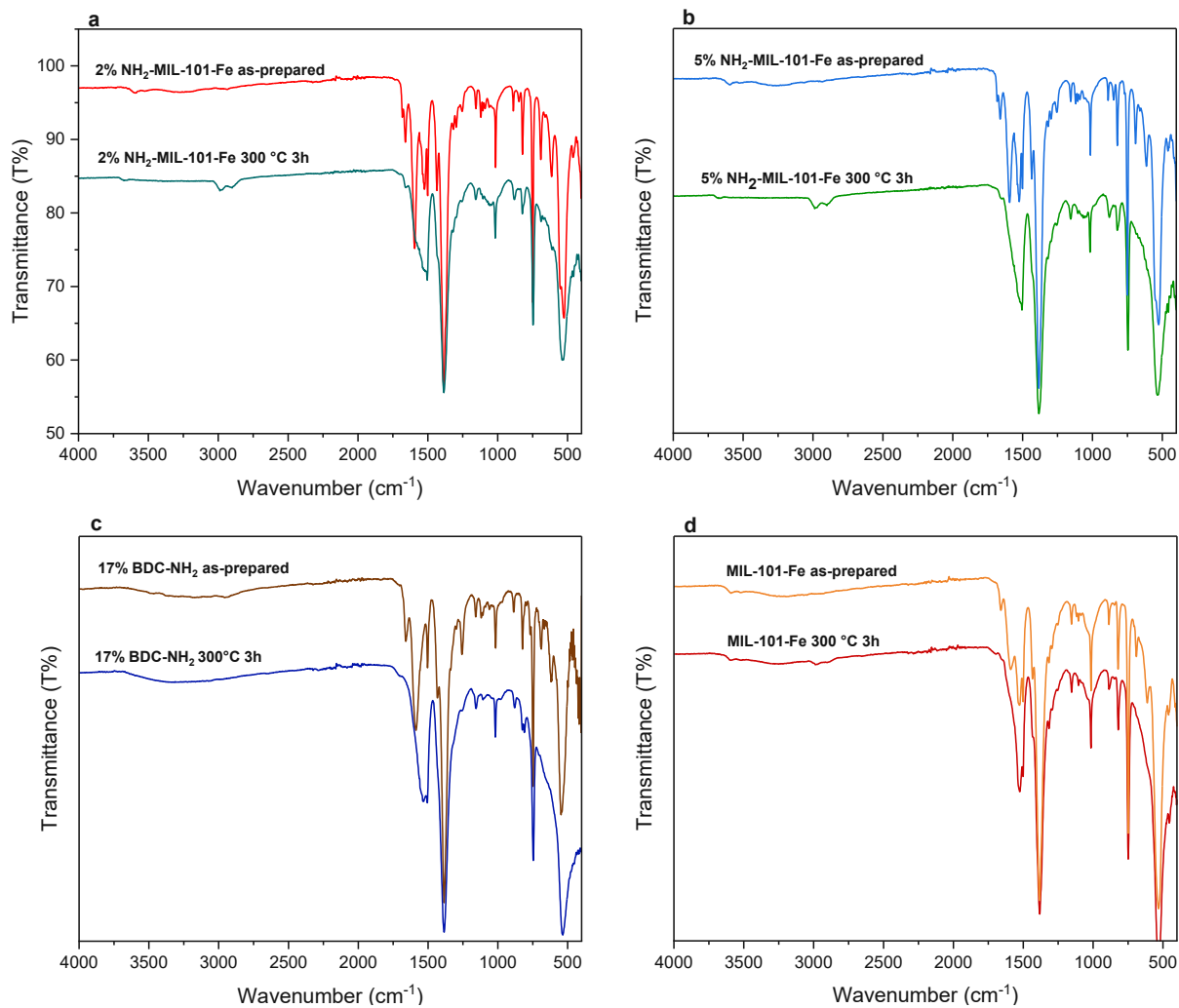


Figure 6-29 Comparison of FTIR spectra of mixed-ligand MOFs before and after heat-treatment: a) 2%NH₂-MIL; b) 5% NH₂-MIL; c) 17%NH₂-MIL; d) MIL-101-Fe as reference.

In the FTIR spectra of the mixed-ligand MOFs obvious structural changes due to the thermal treatment can be observed. The carboxylic asymmetric stretching vibrations, that showed two clearly distinguishable bands converted into one broad band. The structure of the framework is not as refined with well-oriented rigid ligands and corresponding IR bands as before thermolysis. As already discussed in the interpretation of DRS spectra, there are a lot of structural defects in heat-treated MOFs. The bond cleavage of the thermolabile NH₂-BDC as well as BDC ligand has partially occurred. Moreover, the O-Fe-O stretching at 527 cm⁻¹ is still present after thermolysis, but it is significantly weaker than expected due to the missing ligands. In comparison to the

mixed-ligand MOFs the single BDC-ligand MIL has more prominent band after heat treatment at the same parameters.

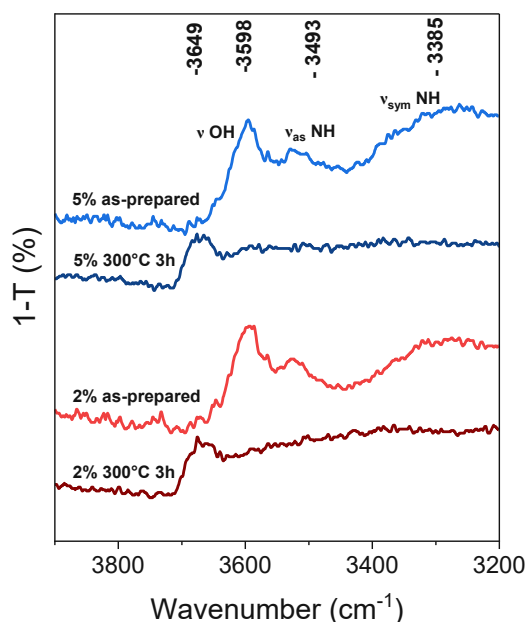


Figure 6-30 Enlarged FTIR region of NH and OH bands for as-prepared and heat-treated mixed-ligand MOFs.

After thermolysis, a new OH bond appeared at 3649 cm^{-1} , although its presence has not been observed in the DRIFTS spectra of these samples. However, considering the possibility of missing or singly coordinated ligands, the presence of the OH bond would be expected, as it is necessary to compensate for the charge arising from the absence of ligands.

The precise determination of the cleavage mechanism and the formation of new bonds would require DFT calculations.

6.3.5.6 Quantification of defects

TGA analysis was performed, replicating the temperature profile of heat treatment. The obtained residual weight was used to estimate the molar ratio of missing ligands after undergoing the temperature profile. The initial sample composition is assumed to be $(\text{Fe}_3\text{O})(\text{BDC}_x\text{NH}_2\text{BDC}_{1-x})_6(1-y)(\text{OH})$ in its dehydrated form, where x represents the molar fraction of the first ligand, and y stands for molar fraction of the missing ligands. The SBU has been considered in its dehydrated form, as at the temperature of thermal treatment, it exists in this state. To align this data with

the calculations, the initial decrease in the TGA curve corresponding to the removal of adsorbed and bound water molecules was subtracted from the initial weight.

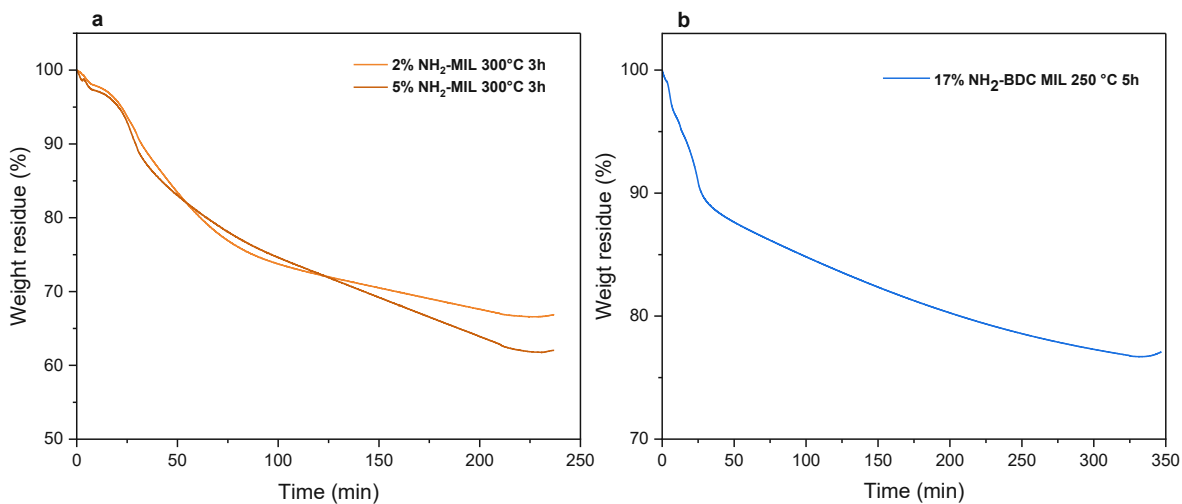


Figure 6-31 Isothermal TGA analysis of mixed-ligand MOFs conducted with reproduced thermolysis parameters: a) 2 and 5 mol.% NH₂-BDC; b) 17 mol.% NH₂-BDC.

Table 6-10 Determined percentage of missing ligand obtained from isothermal TGA analysis reproducing thermolysis parameters.

NH ₂ -BDC mol.%	Residual weight %	Missing ligands %
2	67	30
5	62	32
17	87	10

6.4 Effect of Heat-Treatment on Photocatalytic Nitrogen Reduction Reaction

Based on previous results of the DRS, FTIR and XRD the samples could be heat-treated introducing defects into a structure due to the missing ligands and correlated oxygen vacancies. Heat-treated MOFs have been further tested for photocatalytic NRR.

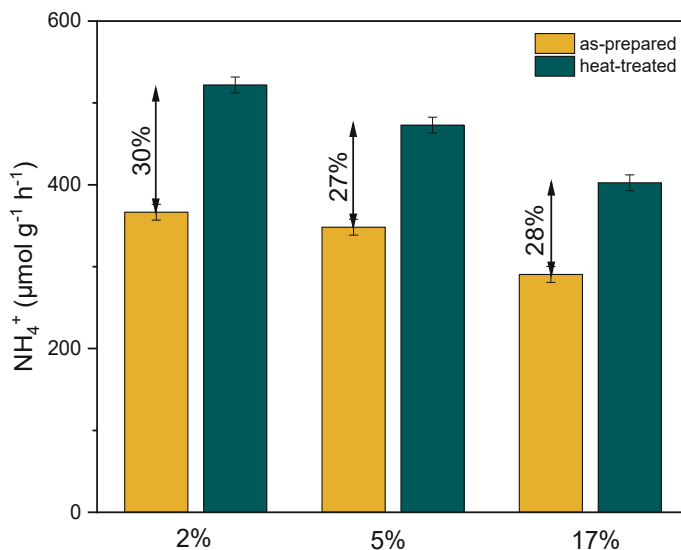


Figure 6-32 Photocatalytic NH_4^+ production rate of mixed-ligand MOFs before and after heat-treatment.

All samples show approximately the same increase in photocatalytic NH_4^+ production rate after thermolysis. The different behavior on the photocatalytic NRR before and after thermolysis is at first correlated to the ligand removal and generation of the active metal sites, as previously reported on MIL-125²⁵.

Here it can be connoted that thermal treatment increases photocatalytic activity of MOFs by introducing coordinatively unsaturated sites, which can serve as adsorption and activation sites for N_2 . However, the same yield increase independently on amino ligand content in as-prepared samples has another cause.

For reference, heat-treated single BDC MOF has been tested for NRR, which shows the same improvement of production rate after treatment with highest yield among all tested samples of $571.55 \mu\text{mol g}^{-1} \text{h}^{-1}$.

The introduction of defects provided accessible sites in which spatial and electronic synergy resulted in activity enhancement. This hypothesis is strongly supported by DRS and FTIR spectra in Fig. 6-24d and Fig.6-25d, respectively.

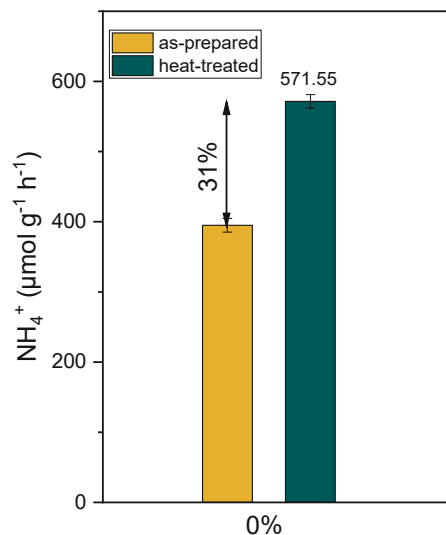


Figure 6-33 Photocatalytic NH_4^+ production rate of MIL-101-Fe before and after heat-treatment.

6.5 Investigations of the Structure Activity Relationship

Another Fe-based MOF MIL-53 has been applied for photocatalytic NRR. MIL-53-Fe has a different mononuclear SBU. It is composed of infinite chains of inorganic octahedrally coordinated Fe^{3+} metal centers, bridged with BDC ligand. Each carboxylate bidentate function is connected to 4 different metal centers bridging a pair of metal centers, so that each Fe^{3+} is coordinated with four different BDC ligands¹⁵⁶. The difference between different SBUs is depicted in Fig. 6-29.

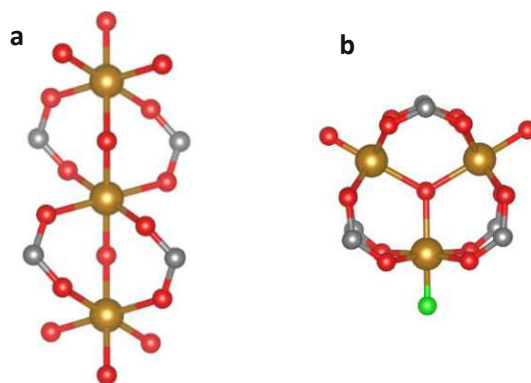


Figure 6-34 Secondary building units of Fe-terephthalate MOFs: a) MIL-53-Fe ($\text{FeO}_4(\text{OH})_2$) from; b) MIL-101-Fe ($\text{Fe}_3\text{O}(\text{RCO}_2)_6(\text{H}_2\text{O})_2\text{X}$).

6.5.1 structural Characterization of MIL-53-Fe

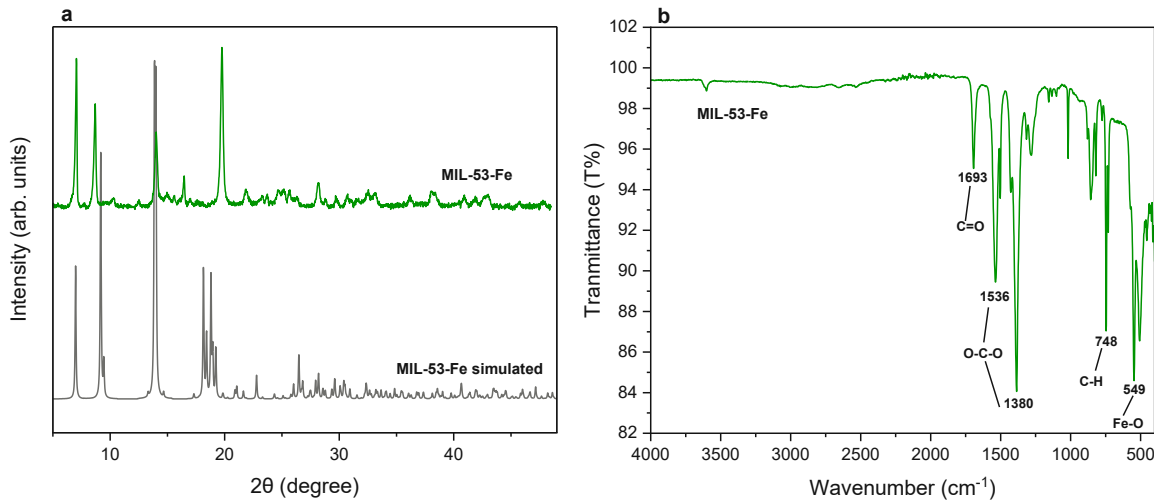


Figure 6-35 Characterization of as-prepared MIL-53-Fe: a) XRD pattern of synthesized MIL-53-Fe in comparison with simulated spectrum of MIL-53-Fe; b) FTIR spectra of MIL-53-Fe.

The XRD pattern of as-prepared MIL-53-Fe shows high crystallinity but all the peaks are not in complete accordance with simulated pattern. The synthesis reproducibility of iron-MOFs from MIL-series has been already discussed and it is highly possible that here the secondary phase or unreacted ligands had impaired the formation of expected crystal structure.

In the FTIR spectra, the prominent band corresponding to OH group coordinated to the SBU can be observed at 3600 cm^{-1} . The band at 549 cm^{-1} corresponds to the stretching of Fe-O bond between carboxylic group of the ligand and Fe^{3+} . The sharp peak at 748 cm^{-1} can be attributed to the C-H bending vibration of the linker. Two broad bands centered at 1536 and 1380 cm^{-1} are asymmetric and symmetric stretching vibrations of C-O bond in carboxylic groups, respectively. A peak of significant intensity can be observed at 1693 cm^{-1} belonging to the stretching vibration of free carboxylic group¹⁵⁷. Thus, a lot of uncoordinated or singly coordinated ligands are present in the framework.

6.5.2 Influence of SBU Tuning of Photocatalytic Nitrogen Reduction

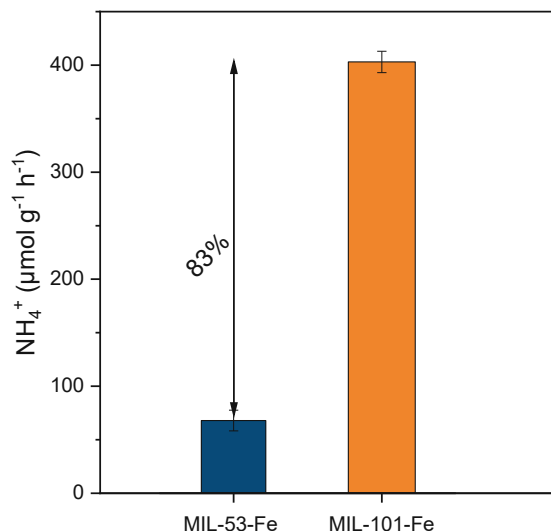


Figure 6-36 Photocatalytic NH_4^+ production rate of Fe-based MOFs with different SBU.

The MIL-53-Fe with mononuclear SBU has 83% lower ammonia production yield. Regarding the structural difference, MIL-53 does not have oxo-bridged trimeric SBU. Based on the SBU observation it can be concluded that the diminished electron delocalization between the metal centers has a determining effect on the NH_4^+ production rate.

6.6 Investigations on the Rate-Determining Step

The conversion of nitrogen to ammonia exhibited variable production rates dependent on the selection of SBU and the functionalization of ligands. Comparing the ammonia yield across differently functionalized single-ligand MOFs, it was concluded: the presence of proton accepting NH_2 group impedes the N_2 conversion process, while the proton donating Br-BDC promotes it. However, the determination of the rate-determining step within this catalytic mechanism remains an open question.

The initial idea of electrochemical measurement was to screen the photocatalyst with potentially good performance in electrochemical system. For that purpose, the anodic current has been determined, as the assessment of reduction potential would be difficult due to the concurrent HER.

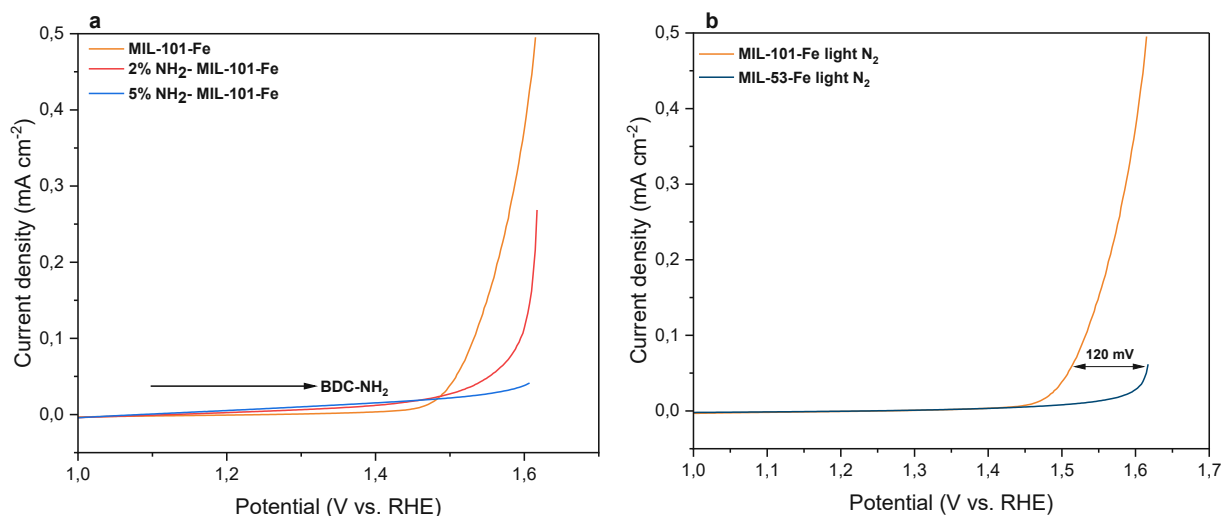


Figure 6-37 J-V curves recorded in 0.1 M Na₂SO₄ with Ag/AgCl electrode and Pt cathode, with potential reported vs. RHE: a) BDC-NH₂ ligand influence; b) SBU influence.

The LSVs of the amino-functionalized ligand MOFs show an anodic shift of the onset potential and decreased current density with increasing NH₂-BDC percentage (Fig. 6-32a). Considering that the redox potential of water oxidation reaction (WOR) is 1.23 V vs. RHE, the anodic current corresponds to the WOR. Therefore, the higher overpotential of this half reaction implies kinetically limited conversion, whereas the slow kinetic explains low current density in NH₂-ligand MOFs.

In Fig. 6-32b J-V curve from the LSV measurements of MIL-53-Fe and MIL-101-Fe are displayed. The overpotential of water oxidation using MIL-101-Fe as a working electrode is 120 mV lower than with MIL-53-Fe. Additionally, the current density reaches a maximum of 0.05 mV cm⁻², which is 10th of the peak current density achieved with MIL-101-Fe. Correspondingly, the oxidative part of conversion is kinetically limited.

Both LSV measurements validate previous observations on ammonia production yield with proton accepting NH₂-BDC and proton donating Br-BDC ligand MOFs about water oxidation half reaction being the rate-determining step.

6.7 Structure and Photocatalytic Activity of Ce-UiO-66 MOF

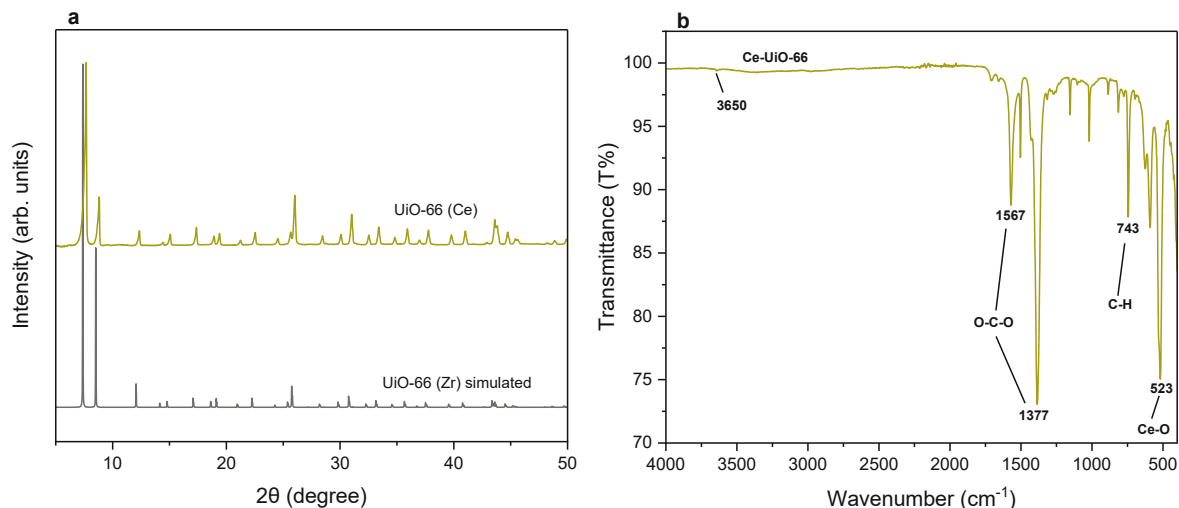


Figure 6-38 Characterization of Ce-UiO-66 as-prepared samples: a) XRD pattern; b) FTIR spectrum.

The synthesized sample shows a high crystallinity and corresponds to the simulated PXRD pattern of isostructural UiO-66 (Zr).

The characteristic bands in the FTIR can be assigned to the asymmetric and symmetric stretching of the carboxylic group at 1567 cm^{-1} and 1377 cm^{-1} , respectively. There is a prominent band at 743 cm^{-1} attributed to the C-H bending. Ce-O stretching of the bridging carboxylate coordination can be seen at 523 cm^{-1} . Not such prominent band at 3560^{-1} of OH group coordination can be observed⁸⁸. Under the same reaction conditions the activity of Ce-UiO-66 towards photocatalytic nitrogen reduction has been tested.

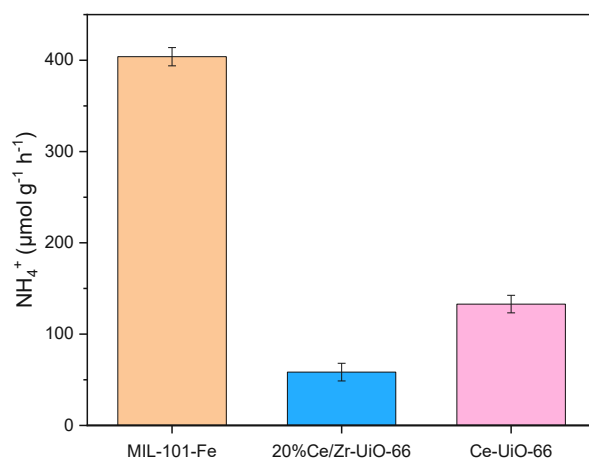


Figure 6-39 Photocatalytic NH_4^+ production rate Ce-UiO-66 and its analogue mixed metal Ce/Zr-UiO-66 under ambient conditions.

For the comparison of the activity in NRR the structural analogue containing 20mol.% Ce as mixed-metal MOF was used to establish the role of the cerium metal cation exchange. The Ce-UiO-66 has a higher ammonia production rate than mixed-metal MOF.

In the literature the reported band gap of pristine Ce-UiO-66 is 2.66 eV, thus the energy of 365 nm LED light source was sufficient for creation of excited states. The motivation for testing Ce-based MOFs raised from low lying unoccupied metal orbital (lower than a ligand LUMO), which could lead to more efficient LMCT, thereby promoting charge separation. Based on previous reports, low lying nature of the empty 4f orbital of Ce makes materials also highly reducible because of the facile formation of Ce^{3+} . Thus, incorporating the Ce^{4+} into the MOF node could be effective strategy to facilitate LMCT and promote metal redox cycling¹⁴⁸.

Although, efficient charge separation would be beneficial and it is desirable for HER only, OER and reduction photocatalysis¹⁴⁸, the appropriate band edge position and the number of electrons in the valence band of Ce^{4+} as well the symmetry and energy of valence band orbital could be the reason lower photocatalytic nitrogen conversion, in comparison to Fe-MOFs. In this thesis, no further studies have been conducted in order to clarify the origin of the Ce-MOF activity.

7 Discussion

7.1 Influence of Ligand- and SBU-tuning

Ligand tuning in mixed-ligand and single-ligand Fe-MOFs resulted in distinct structural and physiochemical properties. FTIR analysis revealed clearly distinguishable structural characteristics between single-ligand BDC and NH₂-BDC MOFs. In the BDC MOF, a single type of coordination was present, whereas in the NH₂-BDC MOF two different coordination bonds were observed.

With incremental increase of NH₂-BDC ligand content in mixed-ligand MOFs, the coordination the coordination bond strength changed, as evidenced by the FTIR spectra (*Fig. 6-8b*). The Fe-O stretching bands were superimposed from those of single ligand MOFs, with noticeable changes in relative intensities. Gradual red-shift in carboxylic asymmetric stretching with NH₂ ligand increase was observed, indicating that weakening of the bidentate carboxylate coordination is proportional to the amino content.

Moreover, the increase of amino ligand content resulted in different Fe-terephthalate crystalline phases as obtained from PXRD measurements. The phase occurring at low NH₂ ligand contents is considered the kinetic product, MIL-101, in contrast to the high NH₂ ligand content, which led to the thermodynamic product, MIL-88B. 17mol.% NH₂-BDC sample was estimated as turning point in which both polymorphs are present.

In addition to the MIL-101 phase, which is known for its large pores, another Fe-terephthalate MOF with different topology and pore structure, called MOF-235 was identified in samples with low NH₂ ligand content. MOF-235 shares the same SBU but has different terminal groups, resulting in an overall positive charge that is neutralized by [FeCl₄]⁻ ions, giving the formula [Fe₃O(BDC)₃(DMF)₃][FeCl₄].

In three separate papers authored by Geoesten *et al.*, researchers identified an isomorphic MOF-235 (Al) as an intermediate stage in the formation of MIL-101. These studies emphasized the critical role played by DMF in stabilizing the MIL-101 structure. DMF acts as a molecular promoter by forming H-Cl-DMF complexes (*Fig. 6.10*). These complexes are crucial as they provide the necessary hydroxide ligands essential for facilitating ligand exchange, which is necessary for the formation of [Fe₃O(BDC)₃(OH₂)₂X] clusters within the MIL-101 framework. During the analysis of

irregular synthesis, it was observed that the diffraction peaks assigned to the MOF-235 phase correspond to crystallographic planes in which the terminal groups and the ligands are in close proximity (Fig. 6.11). In these planes, DMF is engaged in strong van der Waals interactions and hydrogen bonding, making the reassembly into the MIL-101 phase energetically unfavorable.

The mentioned crystallographic planes intersect the benzene ring plane, where NH_2 groups are present in the case of amino-substituted ligands. This specific geometric arrangement results in strong interactions. Consequently, the diffraction peaks corresponding to these planes show an increase in relative intensity, transitioning from the single-ligand BDC MIL to the 17 mol.% NH_2 -BDC MIL.

Examining the PXRD patterns with NH_2 ligand content exceeding 17 mol.%, it was observed that the formation of the MOF-235 crystalline phase did not occur. Instead, a phase-pure MOF, the MIL-88B was formed. This phenomenon was approached from a different perspective.

The crucial difference between MOF-235 and MIL-88B lies in the arrangement of charge-balancing anions: in MOF-235, these anions are located within the pores, whereas in MIL-88B and MIL-101, the OH^- ions directly coordinate with the $\text{Fe}-\mu_3\text{-oxo}$ -cluster.

The NH_2 groups exhibit a weak base character, leading to an increase in the concentration of hydroxide ions. Hydroxide ions are stronger nucleophiles compared to Cl^- , aqua, and DMF ligands in polar aprotic solvents¹³⁴. Due to the presence of these highly nucleophilic hydroxide ions, MOF-235 cluster does not form as an intermediate in cases of high NH_2 content. Instead, the formation of MIL-88B is favored.

However, this remains a hypothesis that requires further validation. The combination of molecular dynamics, which models growth dynamics and specific interactions, with DFT calculations could predict energetically stable structures during self-assembly process¹⁵⁸.

DRS spectra of amino-containing MOFs reveal different optoelectronic properties, in comparison to unmodified BDC MOF. The light absorption gradually increases with increasing NH_2 -BDC content (Section 6.1.1.6), a phenomenon previously reported in the mixed-ligand MIL-88B MOFs¹⁵⁹, although the specific impact on the electronic structure has not been assessed.

This can be attributed to the conjugation of the NH_2 lone pair with the π system of the benzene ring in BDC ligand. This extended conjugation allows pronounced electron delocalization. Thus, instead of reaching a saturation plateau, the electronic states continue to evolve as more NH_2 -BDC units are incorporated, which leads to broadening of already existing absorption band.

In contrast to amino ligand containing Fe-MOFs, the nitro and bromide functionalization led to phase-pure MIL-101-Fe, of which Br-MIL-101(Fe) has not been previously reported. The reason for more promoted formation of MIL-101 in the presence of Br-BDC ligand can be attributed to the enhanced electrostatic interactions between the carboxylate ligand and metal precursor, during the self-assembly process, which enhance the exchange rate of Cl^- by carboxylate anion in the Fe^{3+} coordination sphere and allow kinetic control over the MOF growth. However, the aforementioned simulation studies will be needed for a comprehensive understanding.

An interesting and previously unexplored aspect is the non-negligible bandgap narrowing in Br-BDC MOF (*Fig. 16.6b*). While there is limited literature on d-orbital splitting in Fe-MOFs, a relevant study on ligand-substitution in Ce-UiO-66, which shares the same ligand as MIL-101, provides an interesting insight. In the Ce-MOF, bromide substitution was found to shift down the LUMO of the BDC ligand¹⁴⁸. Given the similarity in ligands between MIL-101 and Ce-UiO-66, this reported LUMO shift becomes relevant in understanding the non-negligible bandgap narrowing observed in Br-BDC MOF.

In NH_2 -BDC-containing MOFs, despite additional LMCT and enhanced light absorption, NH_4^+ production gradually decreases with increasing NH_2 -BDC content. Notably, there is a significant decrease in NH_4^+ production up to 50 mol.% NH_2 -BDC, followed by a more gradual 6% decrease between 50 and 100 mol.%. This suggests that the influence of NH_2 -BDC ligand content extends beyond just reducing active species, indicating the contribution of additional factors. The structural inhomogeneity identified by PXRD could contribute to this effect. Further comparative studies of phase-pure MOFs after adjusting self-assembly parameters will be needed to prove this.

The introduction of electron-withdrawing bromide and nitro groups was hypothesized to enhance the Lewis acidity of metal centers, thereby facilitating nitrogen activation and conversion.

The highest production rate among all tested Fe-MOFs was achieved with Br-MIL-101-Fe, a proton-donating catalyst. The opposing trend in photocatalytic performance compared to proton-accepting amino functionalized MOF suggests that the rate of NH_4^+ production is determined by proton generation. This observation was further supported by the findings from linear sweep voltammograms (*Fig. 6.32a*), which displayed an anodic shift in WOR potential and reduced current density as the NH_2 -BDC content increased. These results confirm the limitation of protons in the conversion of N_2 to NH_3 .

Let's revise the findings on the influence of ligand tuning systematically.

Amino functionalization changes the charge generation pathway from: a) direct excitation in the metal cluster of BDC MOFs to b) dual excitation pathway in NH_2 -BDC MOFs (*Fig. 6.13*).

No studies on amino-containing Fe-MOFs as photocatalysts for NRR have been reported yet. However, amino-containing single-ligand Fe-MOFs have shown remarkable superiority over their non-amino counterparts in diverse photocatalytic applications. This includes organic dye and pollutant degradation,^{160, 161, 142, 113} Cr(VI) reduction¹⁵⁹ and CO_2 reduction¹⁶².

In specific cases like NH_2 -MIL-88B(Fe) and NH_2 -MIL-101(Fe), the presence of dual excitation pathways has been crucial. NH_2 -MIL-101(Fe) exhibited nearly three times higher photocatalytic activity in CO_2 reduction compared to MIL-101(Fe), emphasizing the synergistic effect between charge generation pathways¹⁶².

Other reports highlight the significance of dual excitation pathway and more effective charge separation due to the LMCT in NH_2 -MIL-88B(Fe) for effective utilization in a Fenton-like reactions^{142, 160}.

In NH_2 -MIL-125(Ti), distinctive pathways for charge generation and transfer were observed in comparison to its non-amino functionalized counterpart, MIL-125(Ti). The introduction of NH_2 functionality created a dual excitation pathway, similar to what was observed in my samples. In the case of amino-functionalized MIL-125-Ti, photogenerated holes were localized at the N atoms of the NH_2 -BDC ligand, situated far away from metal-localized electrons. This spatial arrangement resulted in an extended lifetime of charge carriers. However, it is crucial to note that a prolonged lifetime of charge carriers does not automatically imply efficient charge extraction. Conversely, in

the non-amino functionalized MIL-125-Ti, electrons were more effectively extracted through hole scavenging, as emphasized by the author¹⁴⁵.

Based on the systematic studies of previously reported and experimental results, it can be concluded.

Despite the advantageous dual excitation charge generation mechanism facilitated by the NH₂ functionality, enabling additional electron transfer from the ligand to the Fe-O cluster and generating Fe²⁺ potentially useful for nitrogen reduction, the trapping of holes at the N atom of the NH₂ group kinetically restricts the water oxidation, which is necessary for providing the protons essential for N₂ conversion, as depicted in the figure below.

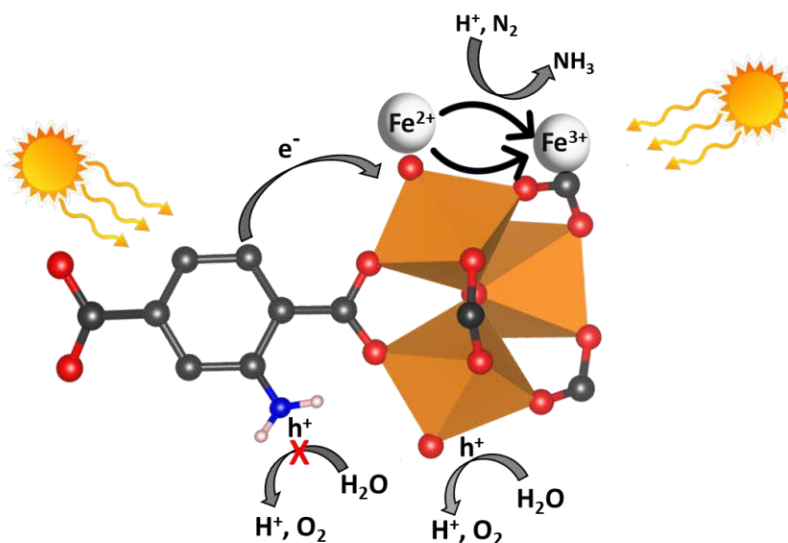


Figure 7-1 Proposed mechanism of electron transfer in the NH₂-BDC MOF on the example of NRR.

Based on these observations, a more detailed understanding of the influence of nitro functionalization can be elucidated.

Nitro functionalization enhances the acidity of Fe³⁺ to a greater extent than Br, as evident from the FTIR analysis (Figure 6.1b), thereby positively influencing NRR. However, due to its strong electron-withdrawing properties and its hybridization with the π system the BDC ligand, the nitro group leads to the accumulation of negative charge on its O atoms. This phenomenon is analogous to what is observed in amino-containing MOFs. The excess negative charge can act as a potent

sink, capturing photogenerated holes. Consequently, the positive effect is counteracted by the negative effect of hole trapping, resulting in an activity similar to that of non-modified BDC MIL.

Furthermore, the impact of the SBU on structure-activity relationship has been investigated by comparing performance of MIL-53-Fe with MIL-101-Fe. MIL-53 resulted in 83% lower activity towards NRR. This signified the crucial role of trimeric oxo-bridged SBU on photocatalytic activity. Additionally, LSV measurements (*Fig. 6-32b*) have shown that water oxidation is kinetically restricted in MIL-53. This is in accordance with the previously observed trends in ligand tuning experiments. The sluggish kinetics of water oxidation in MIL-53-Fe suggests that the number of protons which can react in proton-coupled electron transfer is limited. But why is MIL-101-Fe outperforming MIL-53?

Previous studies of the catalytic activities for aerobic oxidation of alcohols over a trinuclear ruthenium carboxylate catalyst $\text{Ru}_3\text{O}(\text{O}_2\text{CCH}_3)_6(\text{H}_2\text{O})_3$ revealed that a framework containing $\mu_3\text{-O}$ plays an important role in its catalytic performance. It was stated that the existence of $\mu_3\text{-O}$ can promote the formation of a pronounced electronic delocalized states in the Ru_3O cluster, which could help the electron transfer from metal ion to active species¹⁶³.

Another report revealed that multinuclear iron-based molecular complexes are active water oxidation catalysts due to the presence of the two active sites with an appropriate distance for intramolecular O-O formation¹⁶⁴. However, the authors did not publish the exact distance, so it cannot be compared to the one in MIL-101.

The iron cations in the MIL are bridged with bidentate carboxylate ligand, which could restrict the accessibility of water molecules from the side. However, based on the results the molecules can still be adsorbed and destabilized, leading to formation O-O bond, while the Fe redox cycling enables further oxidation reaction. The structural "pocket" created by three iron cations and the bridging tricentered oxygen is essential for the redox activity. This configuration significantly enhances electron delocalization between iron cations, facilitating more efficient electron transfer and extraction. Consequently, this enhanced electron mobility substantially increases the activity in redox reactions.

7.2 Influence of Heat-treatment

After heat-treatment the samples showed high crystallinity (*Fig.6-21*), but not expected properties.

In the as-prepared mixed-ligand MOFs, NH_2 -ligand is responsible for band gap narrowing, so removing this ligand should cause reverse effect. However, DRS spectra after thermolysis showed a newly bandgap decrease, uncorrelated to the initial NH_2 -BDC content. Surprisingly the same trend could be achieved by thermolyzing single-BDC MOF. SEM images of mixed-ligand MOFs (*Fig. 6.27*) disclosed that heat-treatment changed the microstructure by introducing surface cracks. TGA analysis of heat-treated MOFs indicated a high molar fraction of missing ligands: approximately 30, 32 and 10 % for 2, 5 and 17 mol.% NH_2 -BDC samples, respectively (*Table 6.10*). Additionally, a new band in the OH region was observed in the FTIR spectra of these samples (*Fig. 6.30*), indicating the presence of OH^- ions, which are necessary for charge compensation due to the missing ligands.

Previous studies on MIL-125 (Ti) and UiO-66 (Zr) have demonstrated that missing ligands create sub-band defects energies below the conduction band^{165,166}. In MIL-125, missing ligands were produced by etching, whereas UiO-66 exhibited photo-induced missing ligand defects after irradiation with UV light. Interestingly, in the case of UiO-66, the morphology of the defective MOF did not differ from the pristine one. In contrast, the study on MIL-125 reported a rough surface of plate-shaped particles after treatment. Both MOFs were utilized for photocatalytic nitrogen fixation and demonstrated superior performance compared to untreated MOFs. This enhanced performance was attributed to the presence of oxygen vacant active sites.

The morphological characterization, DRS spectra, and TGA analysis, along with insights from previous studies, collectively indicate that thermal treatment introduced structural defects in the form of oxygen vacancies.

After heat-treatment, the catalytic performance of all tested samples increased by 30%. To explain the correlation between ammonia production rate increase and oxygen vacancies a possible interpretation can be constructed.

The presence of oxygen vacancies supposedly increases the electron density of the Fe^{3+} , enhancing its adsorption ability and conversion performance. Since oxygen vacancies carry a positive charge, photogenerated electrons can migrate to the created OVs, creating a mid-gap state and promoting the charge separation. These electrons can be efficiently extracted for the redox reaction or could reduce the Fe^{3+} to Fe^{2+} , which can then reduce the nitrogen by proton coupled electron transfer.

There is a yield enhancement of nearly 30% regardless of the initial ratio of $\text{NH}_2\text{-BDC}$ ligand, even when the percentage of missing ligands varies. This raises questions about the relationship between missing ligands, active site accessibility, and the enhanced yield. Further computational studies could provide better understanding of the interactions between reactants and active sites in the presence of missing ligands.

8 Conclusion

A series of mixed-ligand $x\text{NH}_2\text{-MIL Fe-MOFs}$ with varying ratios of $\text{NH}_2\text{-BDC}$ to BDC ligand were synthesized *via* solvothermal method. With various ex-situ techniques, the influence of amino ligand on structural and physiochemical properties was studied. X-ray diffraction (XRD) revealed that as-prepared MOFs are highly crystalline but crystallize in different phases, depending on the $\text{NH}_2\text{-BDC}$ content. This implied significantly different electrostatic interactions between metal precursor and ligands under same synthesis conditions. Diffuse reflectance spectroscopy (DRS) showed that amino functionalization introduced new electronic states above HOMO level of the ligand, resulting in additional excitation of functionality and band gap narrowing.

Incremental increase in $\text{NH}_2\text{-BDC}$ ligand in MOFs resulted in a proportional decrease in photocatalytic activity. In contrast to proton accepting amino-ligand, functionalization with proton donating Br-BDC promoted ammonia production yield. The anodic branch of linear sweep voltammogram validated the assumption that proton generation is limiting the conversion of N_2 to ammonia.

Another Fe-terephthalate MOF with mononuclear SBU was tested for NRR, disclosing that trinuclear oxo-bridged metal cluster is crucial for superior photocatalytic performance. The presence of $\mu_3\text{-O}$ in the metal center could promote delocalization and more efficient charge extraction. Once again, LSV confirmed that sluggish kinetics of water oxidation and insufficient proton generation is rate-determining step.

In-situ DRIFTS studies of representative $2\%\text{NH}_2\text{-MIL}$ mixed-ligand MOF showed that thermolabile $\text{NH}_2\text{-BDC}$ ligand can be partially cleaved from the framework leaving the BDC-SBU coordination intact. It was established with XRD that $17\text{mol.}\%$ $\text{NH}_2\text{-BDC}$ ligand sample was the one with the highest amino content, that could be subjected to heat-treatment preserving the framework structure. This sample and samples with lower amino content were dwelled at $300\text{ }^\circ\text{C}$ for 3h showing high crystallinity after treatment.

The increase in ammonia production yield after heat-treatment was not correlated with the initial amino content, indicating the creation of defects due to missing or singly coordinated ligands.

SEM images revealed unintended defect engineering, resulting in the introduction of surface cracks. This observation was supported by the high fraction of missing ligands after treatment. The optoelectronic properties after heat-treatment were investigated with DRS. Since the samples, including the non-amino modified MIL-101-Fe, exhibited the same amount of bandgap narrowing, it can be concluded that missing ligands created vacant oxygen sites and new electronic states below the conduction band minimum.

9 Outlook

The present results demonstrate that Fe-MOFs have high photocatalytic activity towards NRR. MIL-101-Fe has been previously reported, as MOF with the highest ammonia production yield among metal-organic frameworks^{20,167}. There are no previous studies on the influence of ligand-tuning, SBU-tuning and thermal-treatment of MIL-101-Fe. This approach brought a deeper understanding structure-related photocatalytic performance of iron-based MOFs, but further potential of these strategies should be explored. Since the water oxidation reaction is a rate-determining step, the introduction of co-catalyst that could promote this half-reaction should be evaluated.

TGA analysis indicated significant levels of missing ligand defects in the heat-treated samples. Despite the varying fraction of missing ligands in these heat-treated samples, they exhibited a 30% increase in yield after thermal treatment. To gain a deeper understanding of the open metal sites and interactions between reactants and active sites in the presence of missing ligands, conducting additional DFT simulations could provide valuable insights.

Given the significant amount of defects created by the applied thermolysis parameters, it is essential to explore the effects of dwelling mixed-ligand MOFs at lower temperatures.

Furthermore, in-situ EPR or XPS studies could elucidate the possibility of reduction of coordinatively unsaturated metal centers during thermal treatment.

It would be interesting to investigate the specific SBU site responsible for water oxidation and nitrogen hydrogenation, especially given that water oxidation typically serves as the rate-determining step.

Additional in-situ DRIFTS studies of reaction in liquid phase could be applied to see the temporal change of functional groups under light irradiation and the formation of NH_x species.

Based on theory, hydrogenation of N_2 can proceed through different diazene and hydrazine intermediates. Simulation studies of reaction mechanisms should be conducted in order to obtain intermediate energies and exact conversion pathways.

10 References

- (1) Rouwenhorst, K. H. R.; Krzywda, P. M.; Benes, N. E.; Mul, G.; Lefferts, L. Chapter 4 - Ammonia Production Technologies. In *Techno-Economic Challenges of Green Ammonia as an Energy Vector*; Valera-Medina, A., Banares-Alcantara, R., Eds.; Academic Press, 2021; pp 41–83. <https://doi.org/10.1016/B978-0-12-820560-0.00004-7>.
- (2) Erisman, J. W.; Sutton, M. A.; Galloway, J.; Klimont, Z.; Winiwarter, W. How a Century of Ammonia Synthesis Changed the World. *Nat. Geosci.* **2008**, *1* (10), 636–639. <https://doi.org/10.1038/ngeo325>.
- (3) Choi, J.; Suryanto, B. H. R.; Wang, D.; Du, H.-L.; Hodgetts, R. Y.; Ferrero Vallana, F. M.; MacFarlane, D. R.; Simonov, A. N. Identification and Elimination of False Positives in Electrochemical Nitrogen Reduction Studies. *Nat. Commun.* **2020**, *11* (1), 5546. <https://doi.org/10.1038/s41467-020-19130-z>.
- (4) MacFarlane, D. R.; Cherepanov, P. V.; Choi, J.; Suryanto, B. H. R.; Hodgetts, R. Y.; Bakker, J. M.; Ferrero Vallana, F. M.; Simonov, A. N. A Roadmap to the Ammonia Economy. *Joule* **2020**, *4* (6), 1186–1205. <https://doi.org/10.1016/j.joule.2020.04.004>.
- (5) Medford, A. J.; Hatzell, M. C. Photon-Driven Nitrogen Fixation: Current Progress, Thermodynamic Considerations, and Future Outlook. *ACS Catal.* **2017**, *7* (4), 2624–2643. <https://doi.org/10.1021/acscatal.7b00439>.
- (6) Wang, L.; Xia, M.; Wang, H.; Huang, K.; Qian, C.; Maravelias, C. T.; Ozin, G. A. Greening Ammonia toward the Solar Ammonia Refinery. *Joule* **2018**, *2* (6), 1055–1074. <https://doi.org/10.1016/j.joule.2018.04.017>.
- (7) Martín, A. J.; Shinagawa, T.; Pérez-Ramírez, J. Electrocatalytic Reduction of Nitrogen: From Haber-Bosch to Ammonia Artificial Leaf. *Chem* **2019**, *5* (2), 263–283. <https://doi.org/10.1016/j.chempr.2018.10.010>.
- (8) Shin, B.-J.; Mun, J.-H.; Devkota, S.; Kim, S.-M.; Kang, T.-H.; Mazari, S. A.; Cho, K.; Kim, S. H.; Chun, D.-H.; Kim, K.-M.; Yoon, H. C.; Moon, J.-H. Comparative Assessment and Multi-Objective Optimization for the Gray and Blue Ammonia Synthesis Processes: Energy, Economic and Environmental (3E) Analysis. *Int. J. Hydrog. Energy* **2023**, S0360319923025454. <https://doi.org/10.1016/j.ijhydene.2023.05.205>.
- (9) Shen, H.; Yang, M.; Hao, L.; Wang, J.; Strunk, J.; Sun, Z. Photocatalytic Nitrogen Reduction to Ammonia: Insights into the Role of Defect Engineering in Photocatalysts. *Nano Res.* **2022**, *15* (4), 2773–2809. <https://doi.org/10.1007/s12274-021-3725-0>.
- (10) Rong, X.; Liu, S.; Xie, M.; Liu, Z.; Wu, Z.; Zhou, X.; Qiu, X.; Wei, J. N₂ Photofixation by Z-Scheme Single-Layer g-C₃N₄/ZnFe₂O₄ for Cleaner Ammonia Production. *Mater. Res. Bull.* **2020**, *127*, 110853. <https://doi.org/10.1016/j.materresbull.2020.110853>.
- (11) Nazemi, M.; El-Sayed, M. A. Plasmon-Enhanced Photo(Electro)Chemical Nitrogen Fixation under Ambient Conditions Using Visible Light Responsive Hybrid Hollow Au-Ag₂O Nanocages. *Nano Energy* **2019**, *63*, 103886. <https://doi.org/10.1016/j.nanoen.2019.103886>.

- (12) Zhang, S.; Zhao, Y.; Shi, R.; Zhou, C.; Waterhouse, G. I. N.; Wang, Z.; Weng, Y.; Zhang, T. Sub-3 Nm Ultrafine Cu₂O for Visible Light Driven Nitrogen Fixation. *Angew. Chem. Int. Ed.* **2021**, *60* (5), 2554–2560. <https://doi.org/10.1002/anie.202013594>.
- (13) Huang, Y.; Zhu, Y.; Chen, S.; Xie, X.; Wu, Z.; Zhang, N. Schottky Junctions with Bi Cocatalyst for Taming Aqueous Phase N₂ Reduction toward Enhanced Solar Ammonia Production. *Adv. Sci.* **2021**, *8* (6), 2003626. <https://doi.org/10.1002/adv.202003626>.
- (14) Sun, S.; Li, X.; Wang, W.; Zhang, L.; Sun, X. Photocatalytic Robust Solar Energy Reduction of Dinitrogen to Ammonia on Ultrathin MoS₂. *Appl. Catal. B Environ.* **2017**, *200*, 323–329. <https://doi.org/10.1016/j.apcatb.2016.07.025>.
- (15) Sultana, S.; Mansingh, S.; Parida, K. M. Phosphide Protected FeS₂ Anchored Oxygen Defect Oriented CeO₂ NS Based Ternary Hybrid for Electrocatalytic and Photocatalytic N₂ Reduction to NH₃. *J. Mater. Chem. A* **2019**, *7* (15), 9145–9153. <https://doi.org/10.1039/C8TA11437D>.
- (16) Wang, Z.; Hu, X.; Liu, Z.; Zou, G.; Wang, G.; Zhang, K. Recent Developments in Polymeric Carbon Nitride-Derived Photocatalysts and Electrocatalysts for Nitrogen Fixation. *ACS Catal.* **2019**, *9* (11), 10260–10278. <https://doi.org/10.1021/acscatal.9b03015>.
- (17) Liu, S.; Wang, S.; Jiang, Y.; Zhao, Z.; Jiang, G.; Sun, Z. Synthesis of Fe₂O₃ Loaded Porous G-C₃N₄ Photocatalyst for Photocatalytic Reduction of Dinitrogen to Ammonia. *Chem. Eng. J.* **2019**, *373*, 572–579. <https://doi.org/10.1016/j.cej.2019.05.021>.
- (18) Qin, J.; Hu, X.; Li, X.; Yin, Z.; Liu, B.; Lam, K. 0D/2D AgInS₂/MXene Z-Scheme Heterojunction Nanosheets for Improved Ammonia Photosynthesis of N₂. *Nano Energy* **2019**, *61*, 27–35. <https://doi.org/10.1016/j.nanoen.2019.04.028>.
- (19) Wang, S.; Li, B.; Li, L.; Tian, Z.; Zhang, Q.; Chen, L.; Zeng, X. C. Highly Efficient N₂ Fixation Catalysts: Transition-Metal Carbides M₂C (MXenes). *Nanoscale* **2020**, *12* (2), 538–547. <https://doi.org/10.1039/C9NR09157B>.
- (20) Hu, K.; Huang, Z.; Zeng, L.; Zhang, Z.; Mei, L.; Chai, Z.; Shi, W. Recent Advances in MOF-Based Materials for Photocatalytic Nitrogen Fixation. *Eur. J. Inorg. Chem.* **2022**, *2022* (3). <https://doi.org/10.1002/ejic.202100748>.
- (21) Zhou, H.-C.; Long, J. R.; Yaghi, O. M. Introduction to Metal–Organic Frameworks. *Chem. Rev.* **2012**, *112* (2), 673–674. <https://doi.org/10.1021/cr300014x>.
- (22) Jia, H.-P.; Quadrelli, E. A. Mechanistic Aspects of Dinitrogen Cleavage and Hydrogenation to Produce Ammonia in Catalysis and Organometallic Chemistry: Relevance of Metal Hydride Bonds and Dihydrogen. *Chem Soc Rev* **2014**, *43* (2), 547–564. <https://doi.org/10.1039/C3CS60206K>.
- (23) Einsle, O.; Rees, D. C. Structural Enzymology of Nitrogenase Enzymes. *Chem. Rev.* **2020**, *120* (12), 4969–5004. <https://doi.org/10.1021/acs.chemrev.0c00067>.
- (24) Jim Clark. *The Haber Process*. <https://chemguide.co.uk/physical/equilibria/haber.html> (accessed 2023-06-28).
- (25) Naghdi, S.; Cherevan, A.; Giesriegl, A.; Guillet-Nicolas, R.; Biswas, S.; Gupta, T.; Wang, J.; Haunold, T.; Bayer, B. C.; Rupprechter, G.; Toroker, M. C.; Kleitz, F.; Eder, D. Selective Ligand Removal to Improve

Accessibility of Active Sites in Hierarchical MOFs for Heterogeneous Photocatalysis. *Nat. Commun.* **2022**, *13* (1), 282. <https://doi.org/10.1038/s41467-021-27775-7>.

(26) Yang, X.; Wang, D. Photocatalysis: From Fundamental Principles to Materials and Applications. *ACS Appl. Energy Mater.* **2018**, *1* (12), 6657–6693. <https://doi.org/10.1021/acsaem.8b01345>.

(27) Braslavsky, S. E. Glossary of Terms Used in Photochemistry, 3rd Edition (IUPAC Recommendations 2006). *Pure Appl. Chem.* **2007**, *79* (3), 293–465. <https://doi.org/10.1351/pac200779030293>.

(28) Fujishima, A.; Honda, K. Electrochemical Photolysis of Water at a Semiconductor Electrode. *Nature* **1972**, *238* (5358), 37–38. <https://doi.org/10.1038/238037a0>.

(29) Yuan, G.; Tan, L.; Wang, P.; Wang, Y.; Wang, C.; Yan, H.; Wang, Y.-Y. MOF-COF Composite Photocatalysts: Design, Synthesis, and Mechanism. *Cryst. Growth Des.* **2022**, *22* (1), 893–908. <https://doi.org/10.1021/acs.cgd.1c01071>.

(30) Verma, P.; Kondo, Y.; Kuwahara, Y.; Kamegawa, T.; Mori, K.; Raja, R.; Yamashita, H. Design and Application of Photocatalysts Using Porous Materials. *Catal. Rev.* **2021**, *63* (2), 165–233. <https://doi.org/10.1080/01614940.2021.1948302>.

(31) Introduction to Solid State Chemistry. https://ocw.mit.edu/courses/3-091sc-introduction-to-solid-state-chemistry-fall-2010/resources/mit3_091scf09_aln03/ (accessed 2023-06-30).

(32) Kalhor, S.; Zarei, M.; Zolfigol, M. A.; Sepehrmansourie, H.; Nematollahi, D.; Alizadeh, S.; Shi, H.; Arjomandi, J. Anodic Electrosynthesis of MIL-53(Al)-N(CH₂PO₃H₂)₂ as a Mesoporous Catalyst for Synthesis of Novel (N-Methyl-Pyrrol)-Pyrazolo[3,4-b]Pyridines via a Cooperative Vinylogous Anomeric Based Oxidation. *Sci. Rep.* **2021**, *11* (1), 19370. <https://doi.org/10.1038/s41598-021-97801-7>.

(33) Xu, Y.; Schoonen, M. A. A. The Absolute Energy Positions of Conduction and Valence Bands of Selected Semiconducting Minerals. *Am. Mineral.* **2000**, *85* (3–4), 543–556. <https://doi.org/10.2138/am-2000-0416>.

(34) Schmickler, W. J. O'M. Bockris, Shaded U.M. Khan: Surface Electrochemistry, a Molecular Level Approach. Plenum Press, New York, London, 1993. ISBN 0-306-44298-1, 1014 Seiten, Preis: \$79.50. *Berichte Bunsenges. Für Phys. Chem.* **1994**, *98* (9), 1207–1207. <https://doi.org/10.1002/bbpc.19940980933>.

(35) Zhang, N.; Li, L.; Shao, Q.; Zhu, T.; Huang, X.; Xiao, X. Fe-Doped BiOCl Nanosheets with Light-Switchable Oxygen Vacancies for Photocatalytic Nitrogen Fixation. *ACS Appl. Energy Mater.* **2019**, *2* (12), 8394–8398. <https://doi.org/10.1021/acsaem.9b01961>.

(36) Atomic and Molecular Orbitals. In *Orbital Interactions in Chemistry*; John Wiley & Sons, Inc.: Hoboken, NJ, USA, 2013; pp 1–14. <https://doi.org/10.1002/9781118558409.ch1>.

(37) Valence Bond Theory, 2012. <https://www.slideserve.com/erasto/valence-bond-theory> (accessed 2023-06-28).

(38) Hao, Q.; Liu, C.; Jia, G.; Wang, Y.; Arandiyani, H.; Wei, W.; Ni, B.-J. Catalytic Reduction of Nitrogen to Produce Ammonia by Bismuth-Based Catalysts: State of the Art and Future Prospects. *Mater. Horiz.* **2020**, *7* (4), 1014–1029. <https://doi.org/10.1039/C9MH01668F>.

- (39) Chen, L.; Shou, J.; Chen, Y.; Han, W.; Tu, X.; Zhang, L.; Sun, Q.; Cao, J.; Chang, Y.; Zheng, H. Efficient Sunlight Promoted Nitrogen Fixation from Air under Room Temperature and Ambient Pressure via Ti/Mo Composites. *Chem. Eng. J.* **2023**, *451*, 138592. <https://doi.org/10.1016/j.cej.2022.138592>.
- (40) Lofthus, A.; Krupenie, P. H. The Spectrum of Molecular Nitrogen. *J. Phys. Chem. Ref. Data* **1977**, *6* (1), 113–307. <https://doi.org/10.1063/1.555546>.
- (41) Appl, M. The Haber-Bosch Process and the Development of Chemical Engineering. In *A Century of Chemical Engineering*; Furter, W. F., Ed.; Springer US: Boston, MA, 1982; pp 29–53. https://doi.org/10.1007/978-1-4899-5289-9_3.
- (42) Atkins, P. W.; De Paula, J. *Elements of Physical Chemistry*, 6th ed.; Oxford University Press: Oxford, 2013.
- (43) Appl, M. Ammonia. In *Ullmann's Encyclopedia of Industrial Chemistry*; Wiley-VCH Verlag GmbH & Co. KGaA, Ed.; Wiley-VCH Verlag GmbH & Co. KGaA: Weinheim, Germany, 2006; p a02_143.pub2. https://doi.org/10.1002/14356007.a02_143.pub2.
- (44) Roberts, M. W. Development of the Industrial Relevance of Catalysis and Its Physiochemical Basis (1860-1940). *Catal. Lett.* **2000**, *67* (1), 5–13. <https://doi.org/10.1023/A:1016674822904>.
- (45) Schlögl, R. Ammonia Synthesis. In *Handbook of Heterogeneous Catalysis*; 2008; pp 2501–2575. <https://doi.org/10.1002/9783527610044.hetcac0129>.
- (46) Li, J.; Li, H.; Zhan, G.; Zhang, L. Solar Water Splitting and Nitrogen Fixation with Layered Bismuth Oxyhalides. *Acc. Chem. Res.* **2017**, *50* (1), 112–121. <https://doi.org/10.1021/acs.accounts.6b00523>.
- (47) Chen, X.; Li, J.-Y.; Tang, Z.-R.; Xu, Y.-J. Surface-Defect-Engineered Photocatalyst for Nitrogen Fixation into Value-Added Chemical Feedstocks. *Catal. Sci. Technol.* **2020**, *10* (18), 6098–6110. <https://doi.org/10.1039/D0CY01227K>.
- (48) Huang, Y.; Zhang, N.; Wu, Z.; Xie, X. Artificial Nitrogen Fixation over Bismuth-Based Photocatalysts: Fundamentals and Future Perspectives. *J. Mater. Chem. A* **2020**, *8* (10), 4978–4995. <https://doi.org/10.1039/C9TA13589H>.
- (49) Chen, X.; Li, N.; Kong, Z.; Ong, W.-J.; Zhao, X. Photocatalytic Fixation of Nitrogen to Ammonia: State-of-the-Art Advancements and Future Prospects. *Mater. Horiz.* **2018**, *5* (1), 9–27. <https://doi.org/10.1039/C7MH00557A>.
- (50) Azofra, L. M.; Li, N.; MacFarlane, D. R.; Sun, C. Promising Prospects for 2D $d^2-d^4 M_3 C_2$ Transition Metal Carbides (MXenes) in N_2 Capture and Conversion into Ammonia. *Energy Environ. Sci.* **2016**, *9* (8), 2545–2549. <https://doi.org/10.1039/C6EE01800A>.
- (51) Li, H.; Shi, J.; Zhao, K.; Zhang, L. Sustainable Molecular Oxygen Activation with Oxygen Vacancies on the {001} Facets of BiOCl Nanosheets under Solar Light. *Nanoscale* **2014**, *6* (23), 14168–14173. <https://doi.org/10.1039/C4NR04810E>.
- (52) Zhang, X.; Yang, P.; Yang, B.; Bai, Y.; Liu, W.; Zhang, K. Synthesis of the Composite Catalyst Bi₄O₅Br₂/BiOBr for the Improved Photocatalytic Degradation of Oilfield Produced Wastewater. *J. Mater. Sci. Mater. Electron.* **2019**, *30* (18), 17276–17287. <https://doi.org/10.1007/s10854-019-02074-6>.

- (53) Li, H.; Li, J.; Ai, Z.; Jia, F.; Zhang, L. Durch Sauerstoff-Leerstellen Vermittelte Photokatalyse Mit BiOCl: Reaktivität, Selektivität Und Ausblick. *Angew. Chem.* **2018**, *130* (1), 128–145. <https://doi.org/10.1002/ange.201705628>.
- (54) Bazhenova, T. A.; Shilov, A. E. Nitrogen Fixation in Solution. *Coord. Chem. Rev.* **1995**, *144*, 69–145.
- (55) van der Ham, C. J. M.; Koper, M. T. M.; Hetterscheid, D. G. H. Challenges in Reduction of Dinitrogen by Proton and Electron Transfer. *Chem Soc Rev* **2014**, *43* (15), 5183–5191. <https://doi.org/10.1039/C4CS00085D>.
- (56) Li, X.; Guo, W.; Liu, Z.; Wang, R.; Liu, H. Fe-Based MOFs for Efficient Adsorption and Degradation of Acid Orange 7 in Aqueous Solution via Persulfate Activation. *Appl. Surf. Sci.* **2016**, *369*, 130–136. <https://doi.org/10.1016/j.apsusc.2016.02.037>.
- (57) Liu, D.; Chen, M.; Du, X.; Ai, H.; Lo, K. H.; Wang, S.; Chen, S.; Xing, G.; Wang, X.; Pan, H. Development of Electrocatalysts for Efficient Nitrogen Reduction Reaction under Ambient Condition. *Adv. Funct. Mater.* **2021**, *31* (11), 2008983. <https://doi.org/10.1002/adfm.202008983>.
- (58) Cambridge Structural Database. <https://www.ccdc.cam.ac.uk/discover/blog/mof-classification-search-screen/> (accessed 2023-01-07).
- (59) Yaghi, O. M.; Li, H. Hydrothermal Synthesis of a Metal–Organic Framework Containing Large Rectangular Channels. *J. Am. Chem. Soc.* **1995**, *117* (41), 10401–10402. <https://doi.org/10.1021/ja00146a033>.
- (60) Batten, S. R.; Champness, N. R.; Chen, X.-M.; Garcia-Martinez, J.; Kitagawa, S.; Öhrström, L.; O’Keeffe, M.; Paik Suh, M.; Reedijk, J. Terminology of Metal–Organic Frameworks and Coordination Polymers (IUPAC Recommendations 2013). *Pure Appl. Chem.* **2013**, *85* (8), 1715–1724. <https://doi.org/10.1351/PAC-REC-12-11-20>.
- (61) Treger, M.; König, C.; Behrens, P.; Schneider, A. M. Fragment-Based Approach for the Efficient Calculation of the Refractive Index of Metal–Organic Frameworks. *Phys. Chem. Chem. Phys.* **2023**, *10.1039.D3CP02356G*. <https://doi.org/10.1039/D3CP02356G>.
- (62) Hoskins, B. F.; Robson, R. Design and Construction of a New Class of Scaffolding-like Materials Comprising Infinite Polymeric Frameworks of 3D-Linked Molecular Rods. A Reappraisal of the Zinc Cyanide and Cadmium Cyanide Structures and the Synthesis and Structure of the Diamond-Related Frameworks [N(CH₃)₄][CuI₂ZnII(CN)₄] and CuI[4,4',4'',4'''-Tetracyanotetraphenylmethane]BF₄.x₆H₅NO₂. *J. Am. Chem. Soc.* **1990**, *112* (4), 1546–1554. <https://doi.org/10.1021/ja00160a038>.
- (63) Abrahams, B. F.; Hoskins, B. F.; Michail, D. M.; Robson, R. Assembly of Porphyrin Building Blocks into Network Structures with Large Channels. *Nature* **1994**, *369* (6483), 727–729. <https://doi.org/10.1038/369727a0>.
- (64) Subramanian, S.; Zaworotko, M. J. Porous Solids by Design:[Zn(4,4'-Bpy)₂(SiF₆)]_n-xDMF, a Single Framework Octahedral Coordination Polymer with Large Square Channels. *Angew. Chem. Int. Ed. Engl.* **1995**, *34* (19), 2127–2129. <https://doi.org/10.1002/anie.199521271>.

- (65) Li, H.; Eddaoudi, M.; O’Keeffe, M.; Yaghi, O. M. Design and Synthesis of an Exceptionally Stable and Highly Porous Metal-Organic Framework. *Nature* **1999**, *402* (6759), 276–279. <https://doi.org/10.1038/46248>.
- (66) Yu, Z.; Cao, X.; Wang, S.; Cui, H.; Li, C.; Zhu, G. Research Progress on the Water Stability of a Metal-Organic Framework in Advanced Oxidation Processes. *Water. Air. Soil Pollut.* **2021**, *232* (1), 18. <https://doi.org/10.1007/s11270-020-04953-9>.
- (67) Eddaoudi, M.; Moler, D. B.; Li, H.; Chen, B.; Reineke, T. M.; O’Keeffe, M.; Yaghi, O. M. Modular Chemistry: Secondary Building Units as a Basis for the Design of Highly Porous and Robust Metal–Organic Carboxylate Frameworks. *Acc. Chem. Res.* **2001**, *34* (4), 319–330. <https://doi.org/10.1021/ar000034b>.
- (68) Yusuf, V. F.; Malek, N. I.; Kailasa, S. K. Review on Metal–Organic Framework Classification, Synthetic Approaches, and Influencing Factors: Applications in Energy, Drug Delivery, and Wastewater Treatment. *ACS Omega* **2022**, *7* (49), 44507–44531. <https://doi.org/10.1021/acsomega.2c05310>.
- (69) Horcajada, P.; Serre, C.; Vallet-Regí, M.; Sebban, M.; Taulelle, F.; Férey, G. Metal–Organic Frameworks as Efficient Materials for Drug Delivery. *Angew. Chem. Int. Ed.* **2006**, *45* (36), 5974–5978. <https://doi.org/10.1002/anie.200601878>.
- (70) Jia, T.; Gu, Y.; Li, F. Progress and Potential of Metal-Organic Frameworks (MOFs) for Gas Storage and Separation: A Review. *J. Environ. Chem. Eng.* **2022**, *10* (5), 108300. <https://doi.org/10.1016/j.jece.2022.108300>.
- (71) Ihsanullah, I. Applications of MOFs as Adsorbents in Water Purification: Progress, Challenges and Outlook. *Curr. Opin. Environ. Sci. Health* **2022**, *26*, 100335. <https://doi.org/10.1016/j.coesh.2022.100335>.
- (72) Kumar, P.; Deep, A.; Kim, K.-H. Metal Organic Frameworks for Sensing Applications. *TrAC Trends Anal. Chem.* **2015**, *73*, 39–53. <https://doi.org/10.1016/j.trac.2015.04.009>.
- (73) Maksimchuk, N. V.; Zalomaeva, O. V.; Skobelev, I. Y.; Kovalenko, K. A.; Fedin, V. P.; Kholdeeva, O. A. Metal–Organic Frameworks of the MIL-101 Family as Heterogeneous Single-Site Catalysts. *Proc. R. Soc. Math. Phys. Eng. Sci.* **2012**, *468* (2143), 2017–2034. <https://doi.org/10.1098/rspa.2012.0072>.
- (74) Kozuch, S.; Martin, J. M. L. “Turning Over” Definitions in Catalytic Cycles. *ACS Catal.* **2012**, *2* (12), 2787–2794. <https://doi.org/10.1021/cs3005264>.
- (75) Cole-Hamilton, D. J. Homogeneous Catalysis--New Approaches to Catalyst Separation, Recovery, and Recycling. *Science* **2003**, *299* (5613), 1702–1706. <https://doi.org/10.1126/science.1081881>.
- (76) Mizuno, N.; Misono, M. Heterogeneous Catalysis. *Chem. Rev.* **1998**, *98* (1), 199–218. <https://doi.org/10.1021/cr960401q>.
- (77) Jiang, J.; Jiang, P.; Wang, D.; Li, Y. The Synthetic Strategies for Single Atomic Site Catalysts Based on Metal–Organic Frameworks. *Nanoscale* **2020**, *12* (40), 20580–20589. <https://doi.org/10.1039/D0NR05907B>.
- (78) Cui, X.; Li, W.; Ryabchuk, P.; Junge, K.; Beller, M. Bridging Homogeneous and Heterogeneous Catalysis by Heterogeneous Single-Metal-Site Catalysts. *Nat. Catal.* **2018**, *1* (6), 385–397. <https://doi.org/10.1038/s41929-018-0090-9>.

- (79) Lashgari, M.; Zeinalkhani, P. Photocatalytic N₂ Conversion to Ammonia Using Efficient Nanostructured Solar-Energy-Materials in Aqueous Media: A Novel Hydrogenation Strategy and Basic Understanding of the Phenomenon. *Appl. Catal. Gen.* **2017**, *529*, 91–97. <https://doi.org/10.1016/j.apcata.2016.10.017>.
- (80) Zhang, N.; Jalil, A.; Wu, D.; Chen, S.; Liu, Y.; Gao, C.; Ye, W.; Qi, Z.; Ju, H.; Wang, C.; Wu, X.; Song, L.; Zhu, J.; Xiong, Y. Refining Defect States in W₁₈O₄₉ by Mo Doping: A Strategy for Tuning N₂ Activation towards Solar-Driven Nitrogen Fixation. *J. Am. Chem. Soc.* **2018**, *140* (30), 9434–9443. <https://doi.org/10.1021/jacs.8b02076>.
- (81) Sun, B.; Liang, Z.; Qian, Y.; Xu, X.; Han, Y.; Tian, J. Sulfur Vacancy-Rich O-Doped 1T-MoS₂ Nanosheets for Exceptional Photocatalytic Nitrogen Fixation over CdS. *ACS Appl. Mater. Interfaces* **2020**, *12* (6), 7257–7269. <https://doi.org/10.1021/acsami.9b20767>.
- (82) Shiraishi, Y.; Shiota, S.; Kofuji, Y.; Hashimoto, M.; Chishiro, K.; Hirakawa, H.; Tanaka, S.; Ichikawa, S.; Hirai, T. Nitrogen Fixation with Water on Carbon-Nitride-Based Metal-Free Photocatalysts with 0.1% Solar-to-Ammonia Energy Conversion Efficiency. *ACS Appl. Energy Mater.* **2018**, *1* (8), 4169–4177. <https://doi.org/10.1021/acsaem.8b00829>.
- (83) Li, X.-H.; Chen, W.-L.; Tan, H.-Q.; Li, F.-R.; Li, J.-P.; Li, Y.-G.; Wang, E.-B. Reduced State of the Graphene Oxide@Polyoxometalate Nanocatalyst Achieving High-Efficiency Nitrogen Fixation under Light Driving Conditions. *ACS Appl. Mater. Interfaces* **2019**, *11* (41), 37927–37938. <https://doi.org/10.1021/acsami.9b12328>.
- (84) Xu, C.; Qiu, P.; Chen, H.; Jiang, F. Semi-Crystalline Graphitic Carbon Nitride with Midgap States for Efficient Photocatalytic Nitrogen Fixation. *Appl. Surf. Sci.* **2020**, *529*, 147088. <https://doi.org/10.1016/j.apsusc.2020.147088>.
- (85) Ziegenbalg, D.; Zander, J.; Marschall, R. Photocatalytic Nitrogen Reduction: Challenging Materials with Reaction Engineering. *ChemPhotoChem* **2021**, *5* (9), 792–807. <https://doi.org/10.1002/cptc.202100084>.
- (86) Kökçam-Demir, Ü.; Goldman, A.; Esrafilı, L.; Gharib, M.; Morsali, A.; Weingart, O.; Janiak, C. Coordinatively Unsaturated Metal Sites (Open Metal Sites) in Metal–Organic Frameworks: Design and Applications. *Chem. Soc. Rev.* **2020**, *49* (9), 2751–2798. <https://doi.org/10.1039/C9CS00609E>.
- (87) Fan, L.; Yu, Q.; Chen, J.; Khan, U.; Wang, X.; Gao, J. Achievements and Perspectives in Metal–Organic Framework-Based Materials for Photocatalytic Nitrogen Reduction. *Catalysts* **2022**, *12* (9), 1005. <https://doi.org/10.3390/catal12091005>.
- (88) Aghajanzadeh, M.; Zamani, M.; Molavi, H.; Khieri Manjili, H.; Danafar, H.; Shojaei, A. Preparation of Metal–Organic Frameworks UiO-66 for Adsorptive Removal of Methotrexate from Aqueous Solution. *J. Inorg. Organomet. Polym. Mater.* **2018**, *28* (1), 177–186. <https://doi.org/10.1007/s10904-017-0709-3>.
- (89) Lebedev, O. I.; Millange, F.; Serre, C.; Van Tendeloo, G.; Férey, G. First Direct Imaging of Giant Pores of the Metal–Organic Framework MIL-101. *Chem. Mater.* **2005**, *17* (26), 6525–6527. <https://doi.org/10.1021/cm051870o>.

- (90) Férey, G.; Mellot-Draznieks, C.; Serre, C.; Millange, F.; Dutour, J.; Surblé, S.; Margiolaki, I. A Chromium Terephthalate-Based Solid with Unusually Large Pore Volumes and Surface Area. *Science* **2005**, *309* (5743), 2040–2042. <https://doi.org/10.1126/science.1116275>.
- (91) Bauer, S.; Serre, C.; Devic, T.; Horcajada, P.; Marrot, J.; Férey, G.; Stock, N. High-Throughput Assisted Rationalization of the Formation of Metal Organic Frameworks in the Iron(III) Aminoterephthalate Solvothermal System. *Inorg. Chem.* **2008**, *47* (17), 7568–7576. <https://doi.org/10.1021/ic800538r>.
- (92) Zorainy, M. Y.; Gar Alalm, M.; Kaliaguine, S.; Boffito, D. C. Revisiting the MIL-101 Metal–Organic Framework: Design, Synthesis, Modifications, Advances, and Recent Applications. *J. Mater. Chem. A* **2021**, *9* (39), 22159–22217. <https://doi.org/10.1039/D1TA06238G>.
- (93) Hwang, Y. K.; Hong, D.-Y.; Chang, J.-S.; Seo, H.; Yoon, M.; Kim, J.; Jhung, S. H.; Serre, C.; Férey, G. Selective Sulfoxidation of Aryl Sulfides by Coordinatively Unsaturated Metal Centers in Chromium Carboxylate MIL-101. *Appl. Catal. Gen.* **2009**, *358* (2), 249–253. <https://doi.org/10.1016/j.apcata.2009.02.018>.
- (94) David Koppenaal, J. L. Small Molecule X-Ray Crystallography, Theory and Workflow. *Encyclopedia of Spectroscopy and Spectrometry*; 2010.
- (95) Małgorzata Kot. In-Operando Hard X-Ray Photoelectron Spectroscopy Study on the Resistive Switching Physics of HfO₂-Based RRAM. Doctoral, 2014. [https://www.researchgate.net/publication/283068066_In-operando_hard_X-ray_photoelectron_spectroscopy_study_on_the_resistive_switching_physics_of_HfO₂-based_RRAM#fullTextFileContent](https://www.researchgate.net/publication/283068066_In-operando_hard_X-ray_photoelectron_spectroscopy_study_on_the_resistive_switching_physics_of_HfO2-based_RRAM#fullTextFileContent) (accessed 2023-02-07).
- (96) *Thermal and Rheological Measurement Techniques for Nanomaterials Characterization*; Thomas, S., Thomas, R., Zachariah, A. K., Mishra, R. K., Eds.; Micro and Nano Technologies; Elsevier: Amsterdam, Netherlands ; Cambridge, MA, 2017.
- (97) Thommes, M.; Kaneko, K.; Neimark, A. V.; Olivier, J. P.; Rodriguez-Reinoso, F.; Rouquerol, J.; Sing, K. S. W. Physisorption of Gases, with Special Reference to the Evaluation of Surface Area and Pore Size Distribution (IUPAC Technical Report). *Pure Appl. Chem.* **2015**, *87* (9–10), 1051–1069. <https://doi.org/10.1515/pac-2014-1117>.
- (98) *Emerging Nanotechnologies for Renewable Energy*; Ahmed, W., Booth, M., Nourafkan, E., Eds.; Micro and nano technologies; Elsevier: Amerstdam ; Cambridge, MA, 2021.
- (99) Sing, K. S. W.; Williams, R. T. Physisorption Hysteresis Loops and the Characterization of Nanoporous Materials. *Adsorpt. Sci. Technol.* **2004**, *22* (10), 773–782. <https://doi.org/10.1260/0263617053499032>.
- (100) Sing, K.; Everett, D.; Haul, R.; Moscou, L.; Pierotti, R. Rouquerol j., Siemieniewska T., Reporting Physisorption Data for Gas/Solid Systems with Special Reference to the Determination of Surface Area and Porosity(Recommendations 1984). *Pure Appl Chem* **1985**, *57* (4), 603–619.
- (101) Burgess, C. G. V.; Everett, D. H.; Nuttall, S. Adsorption Hysteresis in Porous Materials. *Pure Appl. Chem.* **1989**, *61* (11), 1845–1852. <https://doi.org/10.1351/pac198961111845>.

- (102) Dahm, D. J.; Dahm, K. D. Representative Layer Theory for Diffuse Reflectance. *Appl. Spectrosc.* **1999**, *53* (6), 647–654. <https://doi.org/10.1366/0003702991947298>.
- (103) *Infrared and Raman Spectroscopy: Methods and Applications*; Schrader, B., Bougeard, D., Eds.; VCH: Weinheim ; New York, 1995.
- (104) Mirabella, F. M. *Internal Reflection Spectroscopy: Theory and Applications*, 1st ed.; Mirabella, F. M., Ed.; CRC Press, 2020. <https://doi.org/10.1201/9781003066941>.
- (105) Wenning, M.; Seiler, H.; Scherer, S. Fourier-Transform Infrared Microspectroscopy, a Novel and Rapid Tool for Identification of Yeasts. *Appl. Environ. Microbiol.* **2002**, *68* (10), 4717–4721. <https://doi.org/10.1128/AEM.68.10.4717-4721.2002>.
- (106) Mäntele, W.; Deniz, E. UV–VIS Absorption Spectroscopy: Lambert-Beer Reloaded. *Spectrochim. Acta. A. Mol. Biomol. Spectrosc.* **2017**, *173*, 965–968. <https://doi.org/10.1016/j.saa.2016.09.037>.
- (107) Jim Clark. *The Beer-Lambert Law*. <https://chemguide.co.uk/analysis/uvvisible/beerlambert.html> (accessed 2023-07-14).
- (108) Macdonald H. *Scanning Electron Microscopy (SEM)*. Geologic Puzzles. <https://serc.carleton.edu/18401> (accessed 2023-07-14).
- (109) Ezzahmouly, M.; Elmoutaouakkil, A.; Ed-Dahraouy, M.; Khallok, H.; Elouahli, A.; Mazurier, A.; ElAlbani, A.; Hatim, Z. Micro-Computed Tomographic and SEM Study of Porous Bioceramics Using an Adaptive Method Based on the Mathematical Morphological Operations. *Heliyon* **2019**, *5* (12), e02557. <https://doi.org/10.1016/j.heliyon.2019.e02557>.
- (110) Parker, V. D. Chapter 3 Linear Sweep and Cyclic Voltammetry. In *Comprehensive Chemical Kinetics*; Elsevier, 1986; Vol. 26, pp 145–202. [https://doi.org/10.1016/S0069-8040\(08\)70027-X](https://doi.org/10.1016/S0069-8040(08)70027-X).
- (111) Li, J.; Wu, Q.; Wu, J. Synthesis of Nanoparticles via Solvothermal and Hydrothermal Methods. In *Handbook of Nanoparticles*; Aliofkhaezai, M., Ed.; Springer International Publishing: Cham, 2016; pp 295–328. https://doi.org/10.1007/978-3-319-15338-4_17.
- (112) Holder, C. F.; Schaak, R. E. Tutorial on Powder X-Ray Diffraction for Characterizing Nanoscale Materials. *ACS Nano* **2019**, *13* (7), 7359–7365. <https://doi.org/10.1021/acsnano.9b05157>.
- (113) Gecgel, C.; Simsek, U. B.; Gozmen, B.; Turabik, M. Comparison of MIL-101(Fe) and Amine-Functionalized MIL-101(Fe) as Photocatalysts for the Removal of Imidacloprid in Aqueous Solution. *J. Iran. Chem. Soc.* **2019**, *16* (8), 1735–1748. <https://doi.org/10.1007/s13738-019-01647-w>.
- (114) Karimian, R.; Davarpanah, S. J. MIL-101(Fe) Hexagonal Microspindle as a Highly Efficient, Reusable and Versatile Catalyst for Benzo-fused Heterocyclic Nucleus Synthesis. *Appl. Organomet. Chem.* **2018**, *32* (11), e4529. <https://doi.org/10.1002/aoc.4529>.
- (115) Guo, L.; Li, F.; Liu, J.; Li, R.; Yu, Z.; Xi, Q.; Zhang, L.; Li, Y.; Fan, C. Cracked Spindle Morphology of MIL-101(Fe) for Improved Photocatalytic Nitrogen Reduction. *J. Solid State Chem.* **2022**, *316*, 123610. <https://doi.org/10.1016/j.jssc.2022.123610>.

- (116) Zhang, L. J.; Li, F. Q.; Ren, J. X.; Ma, L. B.; Li, M. Q. Preparation of Metal Organic Frameworks MIL-101 (Cr) with Acetic Acid as Mineralizer. *IOP Conf. Ser. Earth Environ. Sci.* **2018**, *199*, 042038. <https://doi.org/10.1088/1755-1315/199/4/042038>.
- (117) Moore, S. C.; Sarazen, M. L. Stability and Kinetics of IRON-TEREPHTHALATE MOFs with Diverse Structures in Aqueous Pollutant Degradation. *AIChE J.* **2023**, e18205. <https://doi.org/10.1002/aic.18205>.
- (118) Bara, D.; Meekel, E.; Pakamoré, I.; Wilson, C.; Ling, S.; Forgan, R. *Exploring and Expanding the Fe-Terephthalate Metal-Organic Framework Phase Space by Coordination and Oxidation Modulation*; preprint; Chemistry, 2021. <https://doi.org/10.26434/chemrxiv-2021-ikt60>.
- (119) Simonsson, I.; Gärdhagen, P.; Andrén, M.; Tam, P. L.; Abbas, Z. Experimental Investigations into the Irregular Synthesis of Iron(III) Terephthalate Metal–Organic Frameworks MOF-235 and MIL-101. *Dalton Trans.* **2021**, *50* (14), 4976–4985. <https://doi.org/10.1039/D0DT04341A>.
- (120) Goesten, M. G.; Stavitski, E.; Juan-Alcañiz, J.; Martínez-Joaristi, A.; Petukhov, A. V.; Kapteijn, F.; Gascon, J. Small-Angle X-Ray Scattering Documents the Growth of Metal–Organic Frameworks. *Catal. Today* **2013**, *205*, 120–127. <https://doi.org/10.1016/j.cattod.2012.08.044>.
- (121) Ma, M.; Bétard, A.; Weber, I.; Al-Hokbany, N. S.; Fischer, R. A.; Metzler-Nolte, N. Iron-Based Metal–Organic Frameworks MIL-88B and NH₂-MIL-88B: High Quality Microwave Synthesis and Solvent-Induced Lattice “Breathing.” *Cryst. Growth Des.* **2013**, *13* (6), 2286–2291. <https://doi.org/10.1021/cg301738p>.
- (122) Cai, X.; Lin, J.; Pang, M. Facile Synthesis of Highly Uniform Fe-MIL-88B Particles. *Cryst. Growth Des.* **2016**, *16* (7), 3565–3568. <https://doi.org/10.1021/acs.cgd.6b00313>.
- (123) Hadjiivanov, K. I.; Panayotov, D. A.; Mihaylov, M. Y.; Ivanova, E. Z.; Chakarova, K. K.; Andonova, S. M.; Drenchev, N. L. Power of Infrared and Raman Spectroscopies to Characterize Metal–Organic Frameworks and Investigate Their Interaction with Guest Molecules. *Chem. Rev.* **2021**, *121* (3), 1286–1424. <https://doi.org/10.1021/acs.chemrev.0c00487>.
- (124) van der Lubbe, S. C. C.; Fonseca Guerra, C. The Nature of Hydrogen Bonds: A Delineation of the Role of Different Energy Components on Hydrogen Bond Strengths and Lengths. *Chem. – Asian J.* **2019**, *14* (16), 2760–2769. <https://doi.org/10.1002/asia.201900717>.
- (125) Taylor-Pashow, K. M. L.; Della Rocca, J.; Xie, Z.; Tran, S.; Lin, W. Postsynthetic Modifications of Iron-Carboxylate Nanoscale Metal–Organic Frameworks for Imaging and Drug Delivery. *J. Am. Chem. Soc.* **2009**, *131* (40), 14261–14263. <https://doi.org/10.1021/ja906198y>.
- (126) Carson, F.; Su, J.; Platero-Prats, A. E.; Wan, W.; Yun, Y.; Samain, L.; Zou, X. Framework Isomerism in Vanadium Metal–Organic Frameworks: MIL-88B(V) and MIL-101(V). *Cryst. Growth Des.* **2013**, *13* (11), 5036–5044. <https://doi.org/10.1021/cg4012058>.
- (127) Feng, D.; Wang, K.; Wei, Z.; Chen, Y.-P.; Simon, C. M.; Arvapally, R. K.; Martin, R. L.; Bosch, M.; Liu, T.-F.; Fordham, S.; Yuan, D.; Omary, M. A.; Haranczyk, M.; Smit, B.; Zhou, H.-C. Kinetically Tuned Dimensional Augmentation as a Versatile Synthetic Route towards Robust Metal–Organic Frameworks. *Nat. Commun.* **2014**, *5* (1), 5723. <https://doi.org/10.1038/ncomms6723>.

- (128) Jiang, D.; Huang, C.; Zhu, J.; Wang, P.; Liu, Z.; Fang, D. Classification and Role of Modulators on Crystal Engineering of Metal Organic Frameworks (MOFs). *Coord. Chem. Rev.* **2021**, *444*, 214064. <https://doi.org/10.1016/j.ccr.2021.214064>.
- (129) Cheetham, A. K.; Kieslich, G.; Yeung, H. H.-M. Thermodynamic and Kinetic Effects in the Crystallization of Metal–Organic Frameworks. *Acc. Chem. Res.* **2018**, *51* (3), 659–667. <https://doi.org/10.1021/acs.accounts.7b00497>.
- (130) Arenas-Vivo, A.; Avila, D.; Horcajada, P. Phase-Selective Microwave Assisted Synthesis of Iron(III) Aminoterephthalate MOFs. *Materials* **2020**, *13* (6), 1469. <https://doi.org/10.3390/ma13061469>.
- (131) Stavitski, E.; Goesten, M.; Juan-Alcañiz, J.; Martinez-Joaristi, A.; Serra-Crespo, P.; Petukhov, A. V.; Gascon, J.; Kapteijn, F. Kinetic Control of Metal–Organic Framework Crystallization Investigated by Time-Resolved In Situ X-Ray Scattering. *Angew. Chem.* **2011**, *123* (41), 9798–9802. <https://doi.org/10.1002/ange.201101757>.
- (132) Goesten, M. G.; Kapteijn, F.; Gascon, J. Fascinating Chemistry or Frustrating Unpredictability: Observations in Crystal Engineering of Metal–Organic Frameworks. *CrystEngComm* **2013**, *15* (45), 9249. <https://doi.org/10.1039/c3ce41241e>.
- (133) Goesten, M. G.; Magusin, P. C. M. M.; Pidko, E. A.; Mezari, B.; Hensen, E. J. M.; Kapteijn, F.; Gascon, J. Molecular Promoting of Aluminum Metal–Organic Framework Topology MIL-101 by *N*, *N*-Dimethylformamide. *Inorg. Chem.* **2014**, *53* (2), 882–887. <https://doi.org/10.1021/ic402198a>.
- (134) *Nucleophiles and Electrophiles*. <https://www.masterorganicchemistry.com/2012/06/05/nucleophiles-and-electrop>.
- (135) Makuła, P.; Pacia, M.; Macyk, W. How To Correctly Determine the Band Gap Energy of Modified Semiconductor Photocatalysts Based on UV–Vis Spectra. *J. Phys. Chem. Lett.* **2018**, *9* (23), 6814–6817. <https://doi.org/10.1021/acs.jpcllett.8b02892>.
- (136) Pazhand, H.; Alvani, A. A. S.; Sameie, H.; Salimi, R.; Poelman, D. *Exploring the Effect of Morphologies of Metal Organic Framework MIL-53(Fe) on the Photocatalytic Performance*; preprint; In Review, 2022. <https://doi.org/10.21203/rs.3.rs-2025694/v1>.
- (137) Cao, W.; Jiang, Z.; Gai, C.; Barrón, V.; Torrent, J.; Zhong, Y.; Liu, Q. Re-Visiting the Quantification of Hematite by Diffuse Reflectance Spectroscopy. *Minerals* **2022**, *12* (7), 872. <https://doi.org/10.3390/min12070872>.
- (138) Lin, J.; Hu, Y.; Wang, L.; Liang, D.; Ruan, X.; Shao, S. M88/PS/Vis System for Degradation of Bisphenol A: Environmental Factors, Degradation Pathways, and Toxicity Evaluation. *Chem. Eng. J.* **2020**, *382*, 122931. <https://doi.org/10.1016/j.cej.2019.122931>.
- (139) Liu, Y.; Xie, Y.; Dai, M.; Gong, Q.; Dang, Z. Ag/AgCl/MIL-101(Fe) Catalyzed Degradation of Methylene Blue under Visible Light Irradiation. *Materials* **2019**, *12* (9), 1453. <https://doi.org/10.3390/ma12091453>.
- (140) Li, Y.; Hou, G.; Yang, J.; Xie, J.; Yuan, X.; Yang, H.; Wang, M. Facile Synthesis of MOF 235 and Its Superior Photocatalytic Capability under Visible Light Irradiation. *RSC Adv.* **2016**, *6* (20), 16395–16403. <https://doi.org/10.1039/C5RA24915E>.

- (141) Glass, C. E. *Interpreting Aerial Photographs to Identify Natural Hazards*; Elsevier: Waltham, MA, 2013.
- (142) Liu, H.; Yin, H.; Yu, X.; Zhu, M.; Dang, Z. Amino-Functionalized MIL-88B as Heterogeneous Photo-Fenton Catalysts for Enhancing Tris-(2-Chloroisopropyl) Phosphate (TCPP) Degradation: Dual Excitation Pathways Accelerate the Conversion of FeIII to FeII under Visible Light Irradiation. *J. Hazard. Mater.* **2022**, 425, 127782. <https://doi.org/10.1016/j.jhazmat.2021.127782>.
- (143) Zhang, Z.; Li, X.; Liu, B.; Zhao, Q.; Chen, G. Hexagonal Microspindle of NH₂-MIL-101(Fe) Metal–Organic Frameworks with Visible-Light-Induced Photocatalytic Activity for the Degradation of Toluene. *RSC Adv.* **2016**, 6 (6), 4289–4295. <https://doi.org/10.1039/C5RA23154J>.
- (144) Bag, P. P.; Sahoo, P. Designing Metal-Organic Frameworks Based Photocatalyst for Specific Photocatalytic Reactions: A Crystal Engineering Approach. In *Green Photocatalysts for Energy and Environmental Process*; Rajendran, S., Naushad, Mu., Ponce, L. C., Lichtfouse, E., Eds.; Environmental Chemistry for a Sustainable World; Springer International Publishing: Cham, 2020; Vol. 36, pp 141–186. https://doi.org/10.1007/978-3-030-17638-9_6.
- (145) Wang, J.; Cherevan, A. S.; Hannecart, C.; Naghdi, S.; Nandan, S. P.; Gupta, T.; Eder, D. Ti-Based MOFs: New Insights on the Impact of Ligand Composition and Hole Scavengers on Stability, Charge Separation and Photocatalytic Hydrogen Evolution. *Appl. Catal. B Environ.* **2021**, 283, 119626. <https://doi.org/10.1016/j.apcatb.2020.119626>.
- (146) Xu, W.; Kang, Y.; Jiao, L.; Wu, Y.; Yan, H.; Li, J.; Gu, W.; Song, W.; Zhu, C. Tuning Atomically Dispersed Fe Sites in Metal–Organic Frameworks Boosts Peroxidase-Like Activity for Sensitive Biosensing. *Nano-Micro Lett.* **2020**, 12 (1), 184. <https://doi.org/10.1007/s40820-020-00520-3>.
- (147) Exner, O. Inductive and Mesomeric Effects in Benzene Derivatives. *Tetrahedron Lett.* **1963**, 4 (13), 815–820. [https://doi.org/10.1016/S0040-4039\(01\)90721-X](https://doi.org/10.1016/S0040-4039(01)90721-X).
- (148) Wu, X.-P.; Gagliardi, L.; Truhlar, D. G. Cerium Metal–Organic Framework for Photocatalysis. *J. Am. Chem. Soc.* **2018**, 140 (25), 7904–7912. <https://doi.org/10.1021/jacs.8b03613>.
- (149) Lin, K.; Zhu, Y.; Zhang, Y.; Lin, H. Determination of Ammonia Nitrogen in Natural Waters: Recent Advances and Applications. *Trends Environ. Anal. Chem.* **2019**, 24, e00073. <https://doi.org/10.1016/j.teac.2019.e00073>.
- (150) Zhao, Y.; Shi, R.; Bian, X.; Zhou, C.; Zhao, Y.; Zhang, S.; Wu, F.; Waterhouse, G. I. N.; Wu, L.; Tung, C.; Zhang, T. Ammonia Detection Methods in Photocatalytic and Electrocatalytic Experiments: How to Improve the Reliability of NH₃ Production Rates? *Adv. Sci.* **2019**, 6 (8), 1802109. <https://doi.org/10.1002/adv.201802109>.
- (151) Yoon, J. W.; Seo, Y.-K.; Hwang, Y. K.; Chang, J.-S.; Leclerc, H.; Wuttke, S.; Bazin, P.; Vimont, A.; Daturi, M.; Bloch, E.; Llewellyn, P. L.; Serre, C.; Horcajada, P.; Grenèche, J.-M.; Rodrigues, A. E.; Férey, G. Controlled Reducibility of a Metal-Organic Framework with Coordinatively Unsaturated Sites for Preferential Gas Sorption. *Angew. Chem. Int. Ed.* **2010**, 49 (34), 5949–5952. <https://doi.org/10.1002/anie.201001230>.

- (152) Zhang, F.; Shang, H.; Wang, L.; Ma, L.; Li, K.; Zhang, Y.; Yang, J.; Li, L.; Li, J. Substituent-Induced Electron-Transfer Strategy for Selective Adsorption of N₂ in MIL-101(Cr)-X Metal–Organic Frameworks. *ACS Appl. Mater. Interfaces* **2022**, *14* (1), 2146–2154. <https://doi.org/10.1021/acsami.1c22866>.
- (153) Zainuri, M. Hematite from Natural Iron Stones as Microwave Absorbing Material on X-Band Frequency Ranges. *IOP Conf. Ser. Mater. Sci. Eng.* **2017**, *196*, 012008. <https://doi.org/10.1088/1757-899X/196/1/012008>.
- (154) Thommes, M.; Cychosz, K. A. Physical Adsorption Characterization of Nanoporous Materials: Progress and Challenges. *Adsorption* **2014**, *20* (2–3), 233–250.
- (155) Zanatta, A. R. Revisiting the Optical Bandgap of Semiconductors and the Proposal of a Unified Methodology to Its Determination. *Sci. Rep.* **2019**, *9* (1), 11225. <https://doi.org/10.1038/s41598-019-47670-y>.
- (156) Nguyen, D. T. C.; Le, H. T. N.; Do, T. S.; Pham, V. T.; Lam Tran, D.; Ho, V. T. T.; Tran, T. V.; Nguyen, D. C.; Nguyen, T. D.; Bach, L. G.; Ha, H. K. P.; Doan, V. T. Metal–Organic Framework MIL-53(Fe) as an Adsorbent for Ibuprofen Drug Removal from Aqueous Solutions: Response Surface Modeling and Optimization. *J. Chem.* **2019**, *2019*, 1–11. <https://doi.org/10.1155/2019/5602957>.
- (157) López, J.; Chávez, A. M.; Rey, A.; Álvarez, P. M. Insights into the Stability and Activity of MIL-53(Fe) in Solar Photocatalytic Oxidation Processes in Water. *Catalysts* **2021**, *11* (4), 448. <https://doi.org/10.3390/catal11040448>.
- (158) Sikdar, A.; Majumdar, A.; Gogoi, A.; Dutta, P.; Borah, M.; Maiti, S.; Gogoi, C.; Anki Reddy, K.; Oh, Y.; Narayan Maiti, U. Diffusion Driven Nanostructuring of Metal–Organic Frameworks (MOFs) for Graphene Hydrogel Based Tunable Heterostructures: Highly Active Electrocatalysts for Efficient Water Oxidation. *J. Mater. Chem. A* **2021**, *9* (12), 7640–7649. <https://doi.org/10.1039/D0TA09077H>.
- (159) Shi, L.; Wang, T.; Zhang, H.; Chang, K.; Meng, X.; Liu, H.; Ye, J. An Amine-Functionalized Iron(III) Metal–Organic Framework as Efficient Visible-Light Photocatalyst for Cr(VI) Reduction. *Adv. Sci.* **2015**, *2* (3), 1500006. <https://doi.org/10.1002/advs.201500006>.
- (160) Taha, A. A.; Huang, L.; Ramakrishna, S.; Liu, Y. MOF [NH₂-MIL-101(Fe)] as a Powerful and Reusable Fenton-like Catalyst. *J. Water Process Eng.* **2020**, *33*, 101004. <https://doi.org/10.1016/j.jwpe.2019.101004>.
- (161) He, J.; Zhang, Y.; Zhang, X.; Huang, Y. Highly Efficient Fenton and Enzyme-Mimetic Activities of NH₂-MIL-88B(Fe) Metal Organic Framework for Methylene Blue Degradation. *Sci. Rep.* **2018**, *8* (1), 5159. <https://doi.org/10.1038/s41598-018-23557-2>.
- (162) Wang, D.; Huang, R.; Liu, W.; Sun, D.; Li, Z. Fe-Based MOFs for Photocatalytic CO₂ Reduction: Role of Coordination Unsaturated Sites and Dual Excitation Pathways. *ACS Catal.* **2014**, *4* (12), 4254–4260. <https://doi.org/10.1021/cs501169t>.
- (163) Qian, L.; Zheng, G. Recent Advances of Metal Nanoclusters for Aerobic Oxidation. *Mater. Today Nano* **2020**, *11*, 100080. <https://doi.org/10.1016/j.mtnano.2020.100080>.

- (164) Okamura, M.; Kondo, M.; Kuga, R.; Kurashige, Y.; Yanai, T.; Hayami, S.; Praneeth, V. K. K.; Yoshida, M.; Yoneda, K.; Kawata, S.; Masaoka, S. A Pentanuclear Iron Catalyst Designed for Water Oxidation. *Nature* **2016**, *530* (7591), 465–468. <https://doi.org/10.1038/nature16529>.
- (165) Wang, L.; Wang, S.; Li, M.; Yang, X.; Li, F.; Xu, L.; Zou, Y. Constructing Oxygen Vacancies and Linker Defects in MIL-125 @TiO₂ for Efficient Photocatalytic Nitrogen Fixation. *J. Alloys Compd.* **2022**, *909*, 164751. <https://doi.org/10.1016/j.jallcom.2022.164751>.
- (166) Gao, W.; Li, X.; Zhang, X.; Su, S.; Luo, S.; Huang, R.; Jing, Y.; Luo, M. Photocatalytic Nitrogen Fixation of Metal–Organic Frameworks (MOFs) Excited by Ultraviolet Light: Insights into the Nitrogen Fixation Mechanism of Missing Metal Cluster or Linker Defects. *Nanoscale* **2021**, *13* (16), 7801–7809. <https://doi.org/10.1039/D1NR00697E>.
- (167) Li, G.; Li, F.; Liu, J.; Fan, C. Fe-Based MOFs for Photocatalytic N₂ Reduction: Key Role of Transition Metal Iron in Nitrogen Activation. *J. Solid State Chem.* **2020**, *285*, 121245. <https://doi.org/10.1016/j.jssc.2020.121245>.

Acknowledgements

I am truly grateful to Prof. Dominik Eder for giving me the opportunity to conduct my thesis in his research group. His guidance, expertise, and truly inspiring ideas have been invaluable throughout this time. I admire his patience and the atmosphere he created in the group. I deeply appreciate his approachable nature and the patience in addressing all the students' questions.

I also want to thank my co-supervisor Dr. Shaghayegh Naghdi, for introducing me to the world of MOFs. I really appreciate the project idea and all the input throughout the work. I am thankful for showing me all the methods and helping me with the data interpretation.

In addition, I am thankful for having been able to work with all the members of the group. I appreciate the collegiality within the group, which greatly contributed to my research experience.

11 Appendix

11.1 In-situ DRIFTS

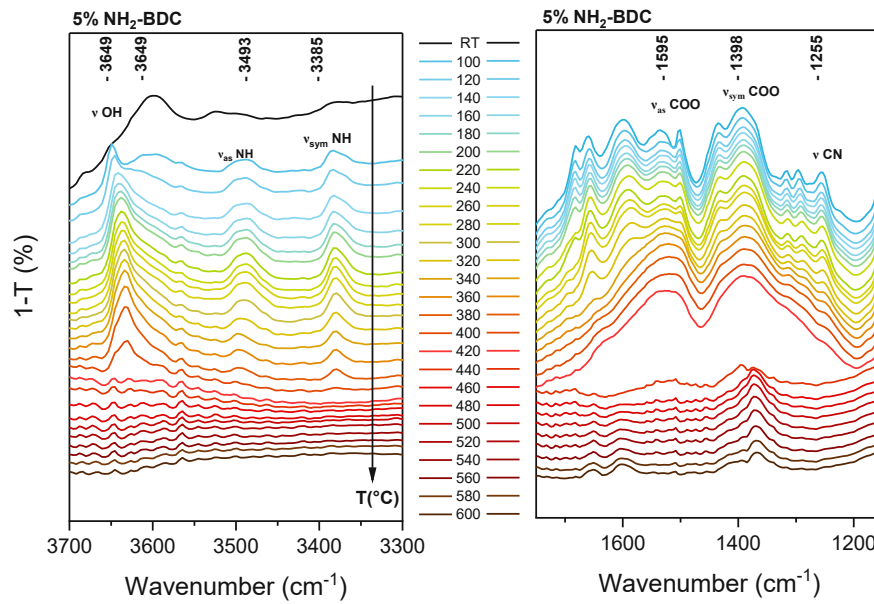


Figure 11-1 In-situ DRIFTS measurements of 5%NH₂-MIL-101-Fe during heating up to 600 °C with ramp rate of 5 °C min⁻¹.

DRIFTS measurement of 5%NH₂-MIL does not show any noticeable difference, in comparison to 2%NH₂-MIL MOF.

11.2 XRD

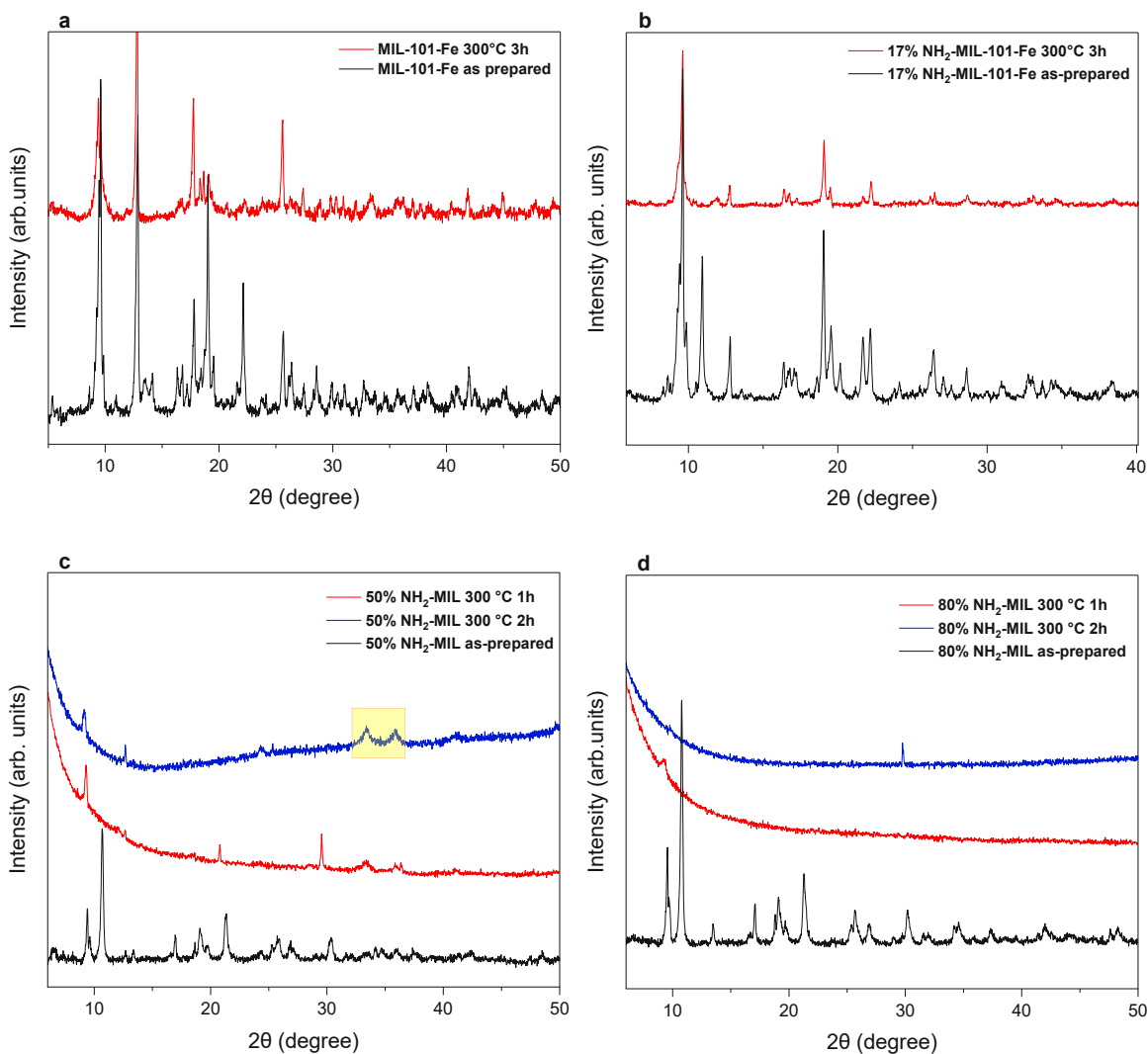


Figure 11-2 Ex-situ XRD patterns of heat-treated MOFs at different parameters: a) single-ligand MIL-101-Fe; b) 17%NH₂-MIL; c) 50% NH₂-MIL; d) 80% NH₂-MIL.

Sample with 17 mol.% NH₂-BDC shows loss of one peak which was quite prominent in as-prepared samples. XRD measurements of 50 and 80 % NH₂-MIL MOFs display structure amorphization after thermal treatment.

11.3 SEM

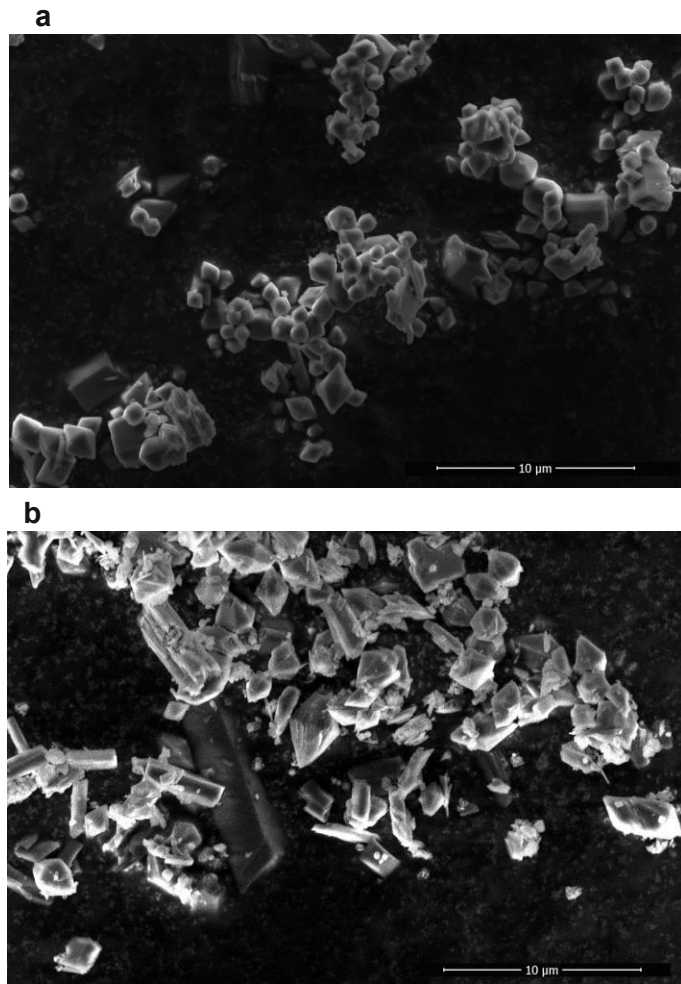


Figure 11-3 SEM images of 2%NH₂-MIL-101-Fe with 12 000x magnification: a) before; b) after heat treatment.

Figure 10.4 displays obvious particle size inhomogeneity and remarkable structural defects of heat-treated MOF in comparison to the as-prepared.